Emergent phenomena in two-dimensional magnetic crystals

Bevin Huang

A dissertation

submitted in partial fulfillment of the

requirements for the degree of

Doctor of Philosophy

University of Washington

2020

Reading Committee:

Xiaodong Xu, Chair

Jiun-Haw Chu

Boris Spivak

Program Authorized to Offer Degree:

Department of Physics

University of Washington

Abstract

Emergent phenomena in two-dimensional magnetic crystals

Bevin Huang

Chair of the Supervisory Committee:
Professor Xiaodong Xu
Department of Physics

Two-dimensional (2D) van der Waals (vdW) crystals and their heterostructures offer a simple, yet powerful platform for discovering emergent phenomena and implementing device structures in the atomically thin limit. Fervent work over the past several years has pushed this frontier to include magnetism. These advances have brought forth a new wave of layered materials that intrinsically possess a wide variety of magnetic properties and are significant for integrating exchange and spin-orbit interactions into vdW heterostructures. In this thesis, we will focus on exploring the tantalizing physics that has been enabled by the discovery of one of these 2D magnetic vdW crystals, namely the magnetic insulator chromium triiodide (CrI_3). While its bulk form is ferromagnetic, emergent layer-dependent magnetism is observed when CrI_3 is cleaved down to just a countable number of layers – it is a ferromagnet in the monolayer, but a layered antiferromagnet when it possesses two to four layers. We leverage this unprecedented magnetic behavior to demonstrate the electrical control of 2D magnetism in bilayer CrI_3, an important step

towards realizing efficient, low-power spintronics devices for computing and memory storage applications. We also uncover a host of magneto-optical phenomena that arise from symmetry-breaking in a 2D magnetic insulator: electrical generation of Kerr signal in a layered antiferromagnet; giant polarization rotation and magnetoelectrical manipulation of Raman phonon selection rules; and discrete angular momentum conservation and its imprint on 2D magnon optical selection rules.

TABLE OF CONTENTS

LIST OF FIGURES

LIST OF TABLES

ACKNOWLEDGEMENTS

I would like to thank Prof. Xiaodong Xu for his enduring patience in advising me these past five years. I am sure there were times where he thought I was too slow to understand something, but he allowed me the space and time to think through certain ideas and grow as a physicist. I would also like to express gratitude to my reading committee, Profs. Jiun-Haw Chu and Boris Spivak, as well as my supervisory committee, Profs. Xiaosong Li, David Cobden, Kai-Mei Fu, and Alejandro Garcia for taking their time to attend and hold my general and final exams to an exceptional standard.

I also owe many thanks to my collaborators: Michael A. McGuire, Efrén Navarro-Moratalla, Dahlia Klein, Zhong Lin, and Tafti Lab at Boston College for growing pristine CrI_3 crystals, Takashi Tanaguchi and Kenji Watanabe in Japan for the world's best hBN crystals, and the theoretical support from Di Xiao's and Wang Yao's team. This dissertation would not be possible without the high-quality materials and the theoretical understanding from these outstanding groups around the world!

I am especially grateful to Emma Schmidgall from Prof. Kai-Mei Fu's lab and Nathan Wilson, who gave me all the encouragement and support to build and debug the magneto-optical Kerr microscope that is now a frequently-used characterization tool in the lab. I joined Xiaodong's lab with absolutely no background in optics, so the expertise that you two provided when I was stumbling through building the MOKE microscope was invaluable. The discussions we had also pushed me to understand more deeply the mechanisms of MOKE and RMCD in magnetic materials.

I am also grateful to each and every one of the Xu lab members both past and present for fostering such a fun and collaborative environment to do science and grow as a person. Everyone in the lab is brilliant and I have learned a lot from their unique perspectives on physics as well as global events, especially about Chinese culture, and U.S.-China relations. Hopefully, my antics in

lab weren't too overbearing and that everyone was able to focus despite the big ball of energy that I am!

Gen was one of the first people who I worked with the most in lab and whom I learned the most from in terms of efficient methods to run experiments and work ethic. She is truly a remarkable mentor and I am indebted to her for helping shape the foundations of my career as a scientist. She also taught me how to bike (better late than never!) after I had been sidelined with numerous running injuries, so without her encouragement, I wouldn't have been able to ride around Lake Washington or complete a century ride in my hometown. Thank you so much, Gen!

I am not sure if my weirdness rubbed off on John, or if he was naturally already weird, but we certainly clicked well together in lab and accomplished a lot with the lattice and magnetic excitations in CrI_3. Hopefully, I wasn't too harsh mentoring you and that you learned a lot from the ramblings that I gave. Keep churning like a black hole and never let that insatiable appetite die!

Thank you to every Chinese member in the lab for helping me learn more about my cultural heritage and improve my spoken Mandarin. While I was born in the U.S., I was still raised in a Chinese household speaking predominantly Cantonese and so I hold myself in high regard to learning as much as possible about my heritage. Besides, you guys have developed my Mandarin enough to allow me to converse with my girlfriend on a daily basis! Not to mention all the "useful phrases" and slang that someone definitely won't pick up in a class!

Nathan, I can't believe it's been five years, but we did it. We suffered through homework sets together and slaved through measuring the alloys, but after all these tribulations, I would say that the end result was worth it. I enjoyed spending my whole PhD with you both in and out of lab and I can only wish you all the best with your postdoctorate position in Germany and career afterwards.

I am also incredibly thankful to my girlfriend, Weisi Xie, who has supported me through tough times in the ongoing coronavirus pandemic as well as through my writing of this thesis. Words cannot describe just how wonderful the moments were that we have spent together and the selfless care and attention that you have showed me. I am the luckiest person in this universe to have met you.

And lastly, I owe my deepest gratitude to my parents for letting me experience this world and pursue the things that give me the most joy in life. I know it must have been difficult raising me financially, but I want to let you know that I love you, always. You are the best parents that anyone wished they could have had.

DEDICATION

To my loving parents who have never ceased supporting me in the toughest of times.

Chapter 1. INTRODUCTION

One of the most important components in a condensed matter system is the interface. The screen you are using to look at this dissertation, for instance, takes advantage of the interfaces in its dielectric layers to reduce glare. Transistors, the building blocks of your phone, computer, or smart device's hardware, utilize the specific combination of interfaces between a metal, electrical insulator, and semiconductor to control the flow of electrons which allow you to browse the internet, or me to write this dissertation. It cannot be understated how prevalent interfaces are in our everyday lives and how important they are for realizing the technologies which society is, for better or for worse, reliant on.

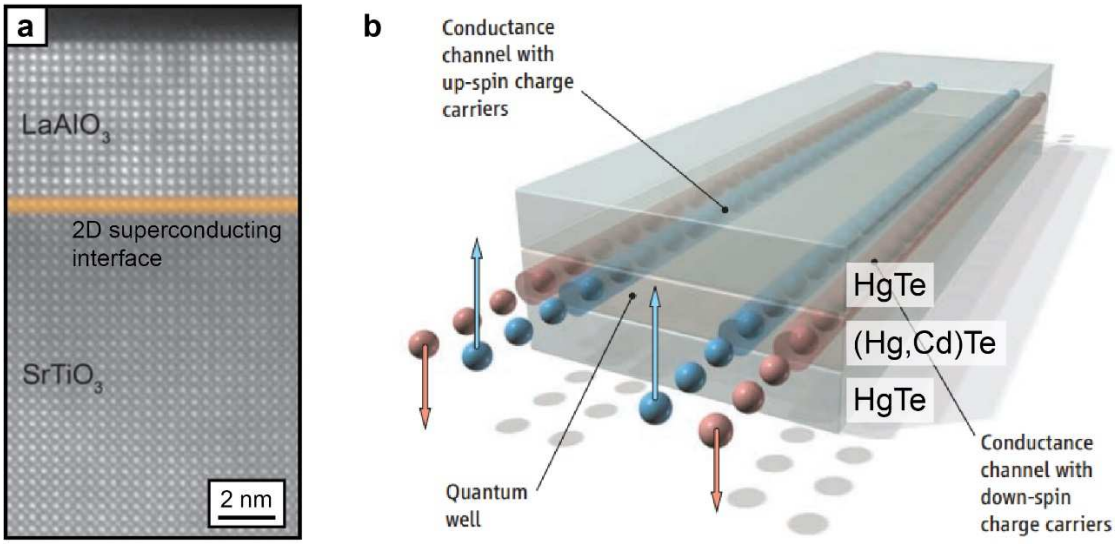

Figure 1.1. Emergent phenomena at the interface of 3D materials. (a) Scanning tunneling electron microscopy image of an $LaAlO_3/SrTiO_3$ heterostructure and its interface. In between these two band insulators is a 2D superconducting interface, highlighted in orange. Scale bar is 2 nm. (b) Quantum spin Hall effect in a HgTe/(Hg,Cd)Te quantum well. Epitaxial growth of (Hg,Cd)Te sandwiched between HgTe in a vertical heterostructure leads to momentum-spin-locked transport along the edges of the (Hg,Cd)Te layer. Panels (a) and (b) are adapted from refs. [1] and [2] with permission from AAAS.

At a more fundamental level, interfaces are a key testbed for controlling quantum phenomena and discovering emergent states of matter in the two-dimensional (2D) limit. A classic example of this is seen in $LaAlO_3/SrTiO_3$ heterostructures. While $LaAlO_3$ and $SrTiO_3$ both are 3D bulk non-magnetic electrical insulators, unconventional superconductivity[1] and ferromagnetic order emerge[3] at the 2D interface when $LaAlO_3$ thin films are grown on top of $SrTiO_3$ (Fig. 1.1a). Electrostatic gating using the $SrTiO_3$ substrate as a dielectric layer allows for the direct observation of a quantum phase transition between this unconventional 2D superconducting state to the normal insulating state[4]. The discovery of the quantum spin Hall effect, a significant milestone in experimental condensed matter physics, also hinged upon optimizing the quasi-2D interfacial HgTe layer (Fig. 1.1b) and Cd-doping in HgTe/(Hg,Cd)Te quantum wells[2,5].

A glaring shortcoming, however, is the very fact that these are 2D states embedded within 3D crystals making it difficult to couple these highly desired states with other quantum materials via proximity effects. On the other hand, van der Waals (vdW) materials provide a natural platform to interface exotic phenomena in the 2D limit. Formed by layers of covalently bonded atoms that are weakly held together by vdW forces, vdW materials can be exfoliated down to the monolayer limit[6]. They exhibit emergent phenomena uniquely seen in two-dimensions such as ballistic transport of Dirac electrons[7,8] and the fractional quantum Hall effect in monolayer graphene[9], spin-valley coupled excitonic physics in semiconducting monolayer transition metal dichalcogenides (MX_2, M = Mo, W; X = S, Se)[10], and the quantum spin Hall effect in monolayer WTe_2[11,12]. Furthermore, these vdW materials can be re-stacked in different combinations to form heterostructures with atomically sharp interfaces, combining or extending the properties of their constituent parts (Fig. 1.2a)[13,14]. This capability has led to work that includes the creation of the first atomically thin light-emitting diode[15–17], the discovery of unconventional superconductivity

in twisted bilayers of graphene (Fig. 1.2b)[18], and moiré-trapped valley excitons in heterobilayers of semiconducting MX_2[19–22].

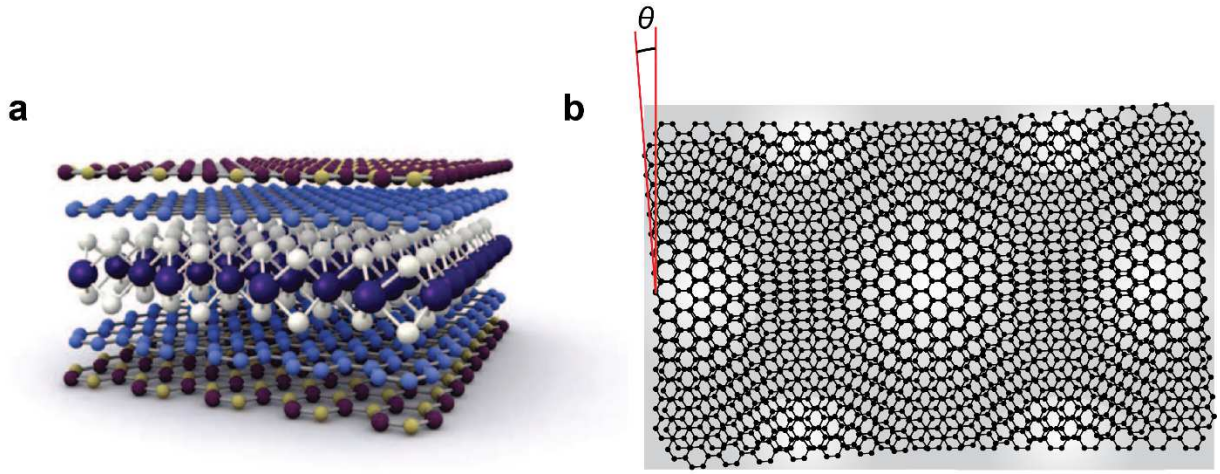

Figure 1.2. Van der Waals heterostructures. (a) An illustration of an example heterostructure formed of van der Waals materials. Monolayers of hexagonal boron nitride (top and bottoms layers) sandwich two layers of graphene and a monolayer transition metal dichalcogenide (middle). The constituent layers are held through weak van der Waals forces. The resulting atomically sharp interfaces are crucial for high-quality electrostatic gating, proximity effects, etc. Reproduced from ref. [14] with permission from AAAS. (b) Moiré superlattice of twisted bilayer graphene. A twist angle, θ, between two layers of graphene results in a moiré superlattice with a unit cell that can be much larger than that of graphene. In this cartoon, $\theta = 4.5^{o}$, and the resulting moiré unit cell is ~15 graphene unit cells large.

Despite a decade of research in ultrathin/exfoliated vdW materials and their heterostructures, monolayer vdW materials with long-range magnetic order did not exist when I joined Prof. Xu's lab in 2015. One of the leading reasons is due to the Mermin-Wagner theorem, which states that long-range magnetic order in 2D cannot be formed in systems without discrete symmetries due to strong thermal fluctuations[23]. By breaking continuous symmetries, e.g. by introducing magnetic anisotropy[24], long-range magnetic order could be stabilized in the 2D limit.

Therefore, if one starts with a bulk crystal that exhibits sufficiently strong magnetic anisotropy, long-range magnetic order could be sustained when cleaved down to the monolayer limit.

A variety of layered magnetic compounds drew interest due to the possibility of retaining their magnetic properties down to monolayer thickness[25–29]. For instance, Raman studies suggested ferromagnetic ordering in few-layer $Cr_2Ge_2Te_6$ and antiferromagnetic ordering in monolayer $FePS_3$[30,31]. One promising candidate is bulk crystalline CrI_3. It shows layered Ising ferromagnetism below a Curie temperature (T_C) of 61 K with an out-of-plane easy-axis[32,33]. Given its van der Waals nature, we expect magnetocrystalline anisotropy, which can lift the Mermin-Wagner restriction, to stabilize long-range ferromagnetic ordering even in a monolayer.

1.1 Dissertation Outline

Therefore, the focus of thesis will be on the exploration of 2D magnetism and emergent phenomena in the atomically thin magnetic insulator, CrI_3. References to other magnetic vdW crystals and their key discoveries will be interspersed in the remarks/conclusions of each section.

In Chapter 2, we will explore the magnetic properties of atomically thin CrI_3, namely its layered antiferromagnetism, and give a thorough explanation for differences in its magnetic order as compared to bulk CrI_3. Important points that will be highlighted are the exchange mechanisms in CrI_3, namely superexchange and super-superexchange, and how the stacking order affects these different exchange pathways. This chapter serves as a foundation to understanding the emergent phenomena investigated in the later chapters.

In Chapter 3, we will investigate the effects of applying an electric field to control the 2D magnetism of bilayer CrI_3, in which there are two unique features. The first is that electrostatic doping changes the interlayer magnetic order of bilayer CrI_3. We will find that this could in principle lead to a magnetic phase transition through ionic liquid gating techniques. The second is

that an interlayer bias through displacement fields leads to a linear magnetoelectric effect that is tied the breaking of the combined time-reversal and inversion symmetries. We will see that this allows the differentiation and readout of antiferromagnetic states that is coveted for spin- and opto-spintronics devices.

In Chapter 4, we will shift our focus to investigating symmetry-related magneto-optical phenomena in the phonons of CrI_3. In particular, we will show that one of the Raman-active phonons in monolayer CrI_3 gives rise to a giant rotation of ~40^o to light that is Raman scattered by this mode. This is over two orders of magnitude larger than the rotation induced from MOKE. We will also show that in bilayer CrI_3, the phonon mode displaying large spin-phonon coupling is Davydov split into an even-parity and odd-parity phonon. We will show that we can readily switch their Raman activity through magnetoelectrical switching of the underlying magnetic state, demonstrating the susceptibility of magneto-optical phenomena by symmetry control in the 2D limit.

Lastly, in Chapter 5, we investigate the 2D magnons of atomically thin CrI_3. We will first show that the magneto-optical selection rules of one-magnon scattering in the 2D limit differ significantly from the bulk, obeying angular momentum conservation up to modulo $3\hbar$ due to the threefold rotational symmetry of a single layer. Due to weak interlayer coupling, these selection rules remain valid for the bilayer, despite possessing a twofold rotationally symmetric lattice. We will also extract the magnetic parameters from these scattering measurements, offering for the first time a method to determine the intra- and interlayer exchange constants, and magnetic anisotropy in the 2D limit.

Chapter 2. LAYER-DEPENDENT MAGNETISM IN A VDW CRYSTAL DOWN TO THE MONOLAYER LIMIT

In this chapter, we will first briefly go over the physical and magnetic properties of bulk CrI_3. This will naturally lead into a discussion of the magnetic properties of CrI_3 in the atomically thin limit as well as an analysis of its differences with unexfoliated bulk crystals. This chapter presents results from my work in *B. Huang et al.* "Layer-dependent ferromagnetism down to the monolayer limit in a vdW crystal" which was published into *Nature* in 2017[34].

2.1 CrI_3 – A CANDIDATE LAYERED MAGNET FOR REALIZING 2D MAGNETISM

As mentioned in the previous chapter, chromium triiodide is a magnetic vdW material. Within each layer, Cr^{3+} ions are covalently bonded and octahedrally coordinated to six I^- ions. These octahedra are edge-shared, forming a Cr^{3+} honeycomb lattice similar to the crystal lattice of graphene (see Fig. 2.1a). CrI_3 layers are held together by weak interlayer vdW forces, with their stacking configuration dependent on the temperature[35]. Illustrated in Fig. 2.1b, above ~200 K, the stacking order of bulk CrI_3 is monoclinic ($C2/m$ or C_{2h}) whereas below 200 K, the stacking order is rhombohedral ($R\bar{3}$ or C_3).

When cooled below 61 K, bulk CrI_3 develops ferromagnetic order as probed by superconducting quantum interference device (SQUID) magnetometry[35]. However, unlike metallic ferromagnets, the primary mode of exchange in CrI_3 is not direct exchange. The overlap of *d*-orbitals between two nearest-neighbor Cr^{3+} ions is small and results in negligible *anti*ferromagnetic exchange interactions (Fig. 2.2a, bottom). Rather, intralayer exchange is dominated by superexchange pathways, exchange interactions between two adjacent Cr^{3+} sites that are mediated by a connecting I^- ion through virtual electron[36,37] (Fig 2.2a, top).

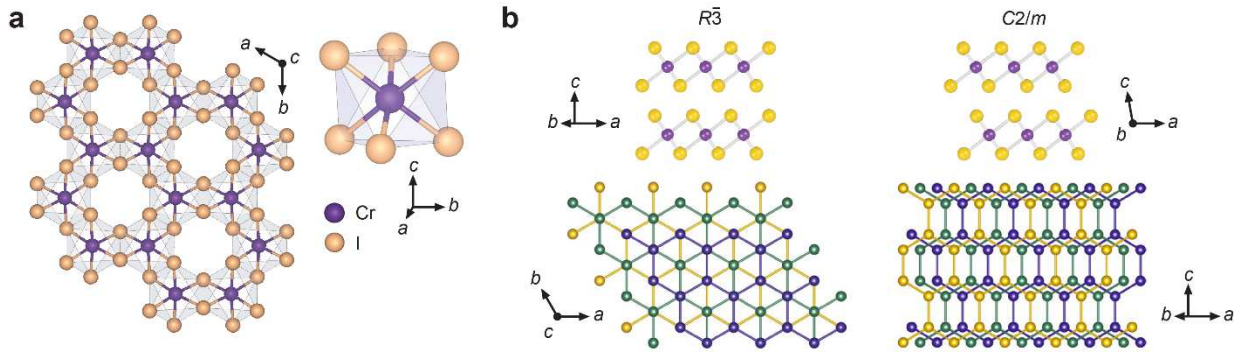

Figure 2.1. Structural properties of layered CrI_3. (a) Top view of a CrI_3 monolayer along with an illustration of the coordination between Cr^{3+} (purple) and I^- (gold) in an octahedral cage. (b) Side (upper-half) and top views (lower-half) of the CrI_3 layers in the rhombohedral (left) and monoclinic (right) phases. Three CrI_3 layers are shown without the I^- ions to show the relative stacking order of the bottom (yellow), middle (green) and top (blue) Cr^{3+} layers in both phases. Reproduced from ref. [38].

Whether a superexchange interaction is ferromagnetic or antiferromagnetic can be intuited through the Goodenough-Kanamori-Anderson (GKA) rules[39,40], which depend on 1) the geometry of the metal-ligand-metal bonds and the *d* orbitals involved in covalent bonding, and 2) whether the orbitals are empty or half-filled. In general, however, the GKA rules state that superexchange between half-filled orbitals results in antiferromagnetic exchange while superexchange between a half-filled orbital and an empty one is ferromagnetic. Superexchange pathways which are formed by a 90° bond angle also tend to be ferromagnetic[39], though there are certainly exceptions such as when the bond angle deviates significantly from 90° or when there is an additional ion bonded to the ligand[41].

With the GKA rules in mind, we now intuit the ferromagnetic order in CrI_3. Due to crystal field splitting from the octahedral environment, the Cr^{3+} *d* orbitals are split into a set of three degenerate t_{2g} orbitals (d_{xy}, d_{xz}, d_{yz}) and two degenerate e_g orbitals ($d_{x^2-y^2}$ and d_{z^2}). There are three electrons per Cr^{3+} site, each singly occupying one of the t_{2g} orbitals. The bond angle formed by

two adjacent Cr^{3+} ions and an I^- ion is ~90°, with the orbitals participating in bonding and superexchange depicted in Fig. 2.2b. Clearly, the superexchange pathways involve either two empty Cr^{3+} e_g orbitals with virtual hopping of like-spins from two different p orbitals, or a half-filled t_{2g} orbital to an empty e_g orbital. From the GKA rules, we can intuit that the intralayer exchange interactions between two adjacent Cr^{3+} sites must be ferromagnetic. Interlayer exchange interactions between Cr^{3+} sites of adjacent layers are determined through super-superexchange, which for bulk CrI_3 results in ferromagnetic interlayer exchange. This will be elaborated on further in Section 2.6.

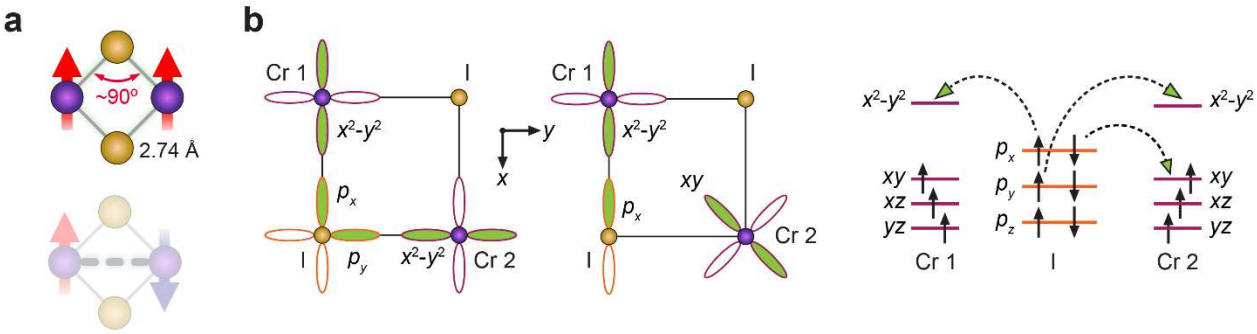

Figure 2.2. Exchange pathways in monolayer CrI_3. (a) Illustrations of direct exchange (bottom, grayed out) and superexchange pathways (top) in CrI_3. (b) Virtual hopping of electrons between the I^- anion and Cr^{3+} occurs through two paths. The first path bridges an I^- p_x and p_y orbital with the x^2-y^2 orbitals of both Cr^{3+} ions. The second path links the I^- p_x orbital to the x^2-y^2 orbital of one Cr^{3+} ion and the xy orbital of the second Cr^{3+} ion. Both paths lead to ferromagnetism between adjacent Cr^{3+} sites. Adapted from ref. [38].

Ferromagnetic spins in bulk CrI_3 also exhibit strong out-of-plane anisotropy, seen from SQUID magnetometry measurements by the significantly small out-of-plane saturation magnetic field (~0.2 T) and large in-plane saturation field (3 T)[34]. The calculated magnetic anisotropy of CrI_3 is around 600 μeV/Cr^{3+} and was revealed through density functional theory (DFT) calculations to result from large spin-orbit coupling (SOC) of the I^- ions[42]. This is confirmed by

observing the anisotropies of $CrCl_3$ and $CrBr_3$, two isostructural magnetic insulators which have the I^- ions substituted by Cl^- and Br^- ions, respectively. From electron paramagnetic resonance measurements, $CrCl_3$ possesses the lowest anisotropy, more than an order of magnitude lower than CrI_3, while $CrBr_3$ exhibits an anisotropy that is almost five times lower than that of CrI_3[43]. Since, the lattice is isostructural between the CrX_3 compounds, single-ion anisotropy should not change[44]. SOC of the anion, on the other hand, depends on Z^4, where Z is the atomic number of the anion. Clearly, I^- has a much larger spin-orbit coupling strength than Br^-, which in turn has a larger SOC than Cl^- (see Table 2.1). Therefore, the anion in a superexchange interaction is not only important for establishing the magnetic ground state of a material, but also instrumental in determining its anisotropy. The combination of its magnetic order and strong anisotropy thus makes CrI_3 a promising candidate to study magnetism down to the 2D limit.

Table 2.1. Normalized spin-orbit coupling of halide series relative to iodine and experimental anisotropy of corresponding chromium trihalide[43]

Atom	Z	Norm. SOC	Anisotropy (μeV/Cr^{3+})
Cl	17	1.1×10^{-2}	24
Br	35	1.9×10^{-1}	83
I	53	1	340

2.2 Exfoliation and thickness identification of CrI_3 flakes

Since individual layers of a CrI_3 crystal are held weakly by vdW forces, a small mechanical force applied perpendicular to the layers will separate them. The method we use to cleave these crystals is through a mechanical exfoliation technique using scotch tape, as pioneered by Andre Geim and Konstantin Novoselov in their seminal work on isolating monolayer graphene[6]. Cleaved CrI_3

crystals are then deposited onto SiO_2/Si wafer, leaving behind CrI_3 flakes of varying thickness and size (10-10000 μm^2) on the wafer substrate.

To identify the thicknesses of exfoliated CrI_3 flakes, we employed two methods: optical contrast and topography mapping through an atomic force microscope. Figure 2.3a shows an example exfoliation of atomically thin CrI_3. Light that is incident on flakes of CrI_3 undergo multiple reflections at the different interfaces between air, CrI_3, SiO_2, and Si, and interfere (Fig. 2.3b). The conditions for thin film interference, for CrI_3 flakes on the same SiO_2/Si substrate, are set entirely by the thickness of the CrI_3 flake. Consequently, the different flake colors seen in Fig. 2.3a correspond to different thicknesses of flakes that can be mapped to a specific thickness by directly extracting its thickness through atomic force microscopy.

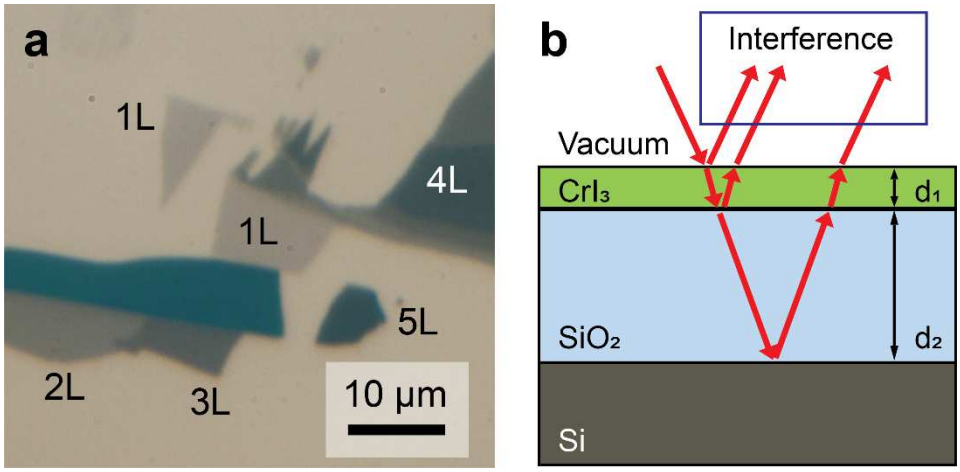

Figure 2.3. Optical image and thin-film interference of CrI_3 on SiO_2/Si. (a) White light image of atomically thin CrI_3 flakes with their thicknesses labeled. Scale bar is 10 μm. (b) Thin-film interference diagram of CrI_3 (green) on SiO_2/Si (light blue/gray) substrate due to reflections at each interface. The thicknesses of the CrI_3 layer and SiO_2 layer are d_1 and d_2, respectively. The Si is treated as semi-infinite and hence opaque to optical light. Panel (b) adopted from ref. [34].

In more detail, we optically determined the thickness of CrI_3 flakes by looking at their contrast with the SiO_2 substrate at a specific wavelength of light. Exfoliated CrI_3 flakes were

imaged using a Nikon Eclipse LV-CH 150NA microscope and illuminated through a 100x objective at normal incidence by a monochromatically filtered halogen lamp. The peak intensity of light emitted through the filter was centered around 631 nm and a bandwidth of ~5 nm. Optical images of these flakes were then captured using a DS-Ri2 full frame camera. The normalized contrast at 631 nm, *C*, was then experimentally obtained through the following equation:

$$C = \frac{I_{flake} - I_{substrate}}{I_{flake} + I_{substrate}},$$

where I_{flake} and $I_{substrate}$ are the reflected intensities of light from the CrI_3 flake and SiO_2/Si substrate, respectively. These experimental contrast values were then compared to a theoretical contrast model derived from the Fresnel equations outlined in ref. [45] and take the form:

$$I_{substrate}(\lambda) = \left| \frac{r_{02} + r_{23}e^{-2i\Phi_2}}{1 + r_{02}r_{23}e^{-2i\Phi_2}} \right|^2$$

$$I_{flake}(\lambda) = \left| \frac{r_{02}e^{i(\Phi_1+\Phi_2)} + r_{12}e^{-i(\Phi_1-\Phi_2)} + r_{23}e^{-i(\Phi_1+\Phi_2)} + r_{01}r_{12}r_{23}e^{i(\Phi_1-\Phi_2)}}{e^{i(\Phi_1+\Phi_2)} + r_{01}r_{12}e^{-i(\Phi_1-\Phi_2)} + r_{01}r_{23}e^{-i(\Phi_1+\Phi_2)} + r_{12}r_{23}e^{i(\Phi_1-\Phi_2)}} \right|^2$$

The subscripts 0, 1, 2, and 3 in the above equation refer to vacuum, CrI_3, SiO_2, and Si, respectively. The coefficients r_{jk} refer to the complex reflection coefficients between media *j* and *k* which take the form:

$$r_{jk} = \frac{\tilde{n}_j - \tilde{n}_k}{\tilde{n}_j + \tilde{n}_k}$$

where $\tilde{n}_j$ and $\tilde{n}_k$ are the complex indices of refraction for medias *j* and *k*, respectively. Likewise, Φ_j refers to the phase shift due to light of wavelength, λ, propagating in media *j* of thickness d_j:

$$\Phi_j = \frac{2\pi\tilde{n}_j d_j}{\lambda}$$

As can be seen, these calculations require the complex indices refraction of each media. Although the index of refraction is well-known for SiO_2, it must be calculated for CrI_3. To do this, we perform a numerical integration using the following Kramers-Kronig relations:

$$\theta(E) = -\frac{E}{\pi}\int_0^{\infty} \frac{\ln[R(E')]}{(E')^2 - E^2} dE'$$

$$r(E) = \sqrt{R(E)}e^{i\theta(E)} = \frac{n(E) - 1 + i\kappa(E)}{n(E) + 1 + i\kappa(E)}$$

where $r(E)$ is the derived complex reflection coefficient of CrI_3. The derivation of $\theta(E)$, the phase of the complex reflection coefficient, requires an integration of the reflectance of CrI_3 across the entire energy spectrum. For this, we rely on previous measurements of the reflectivity in bulk CrI_3[46], $R(E)$ taken at 300 K.

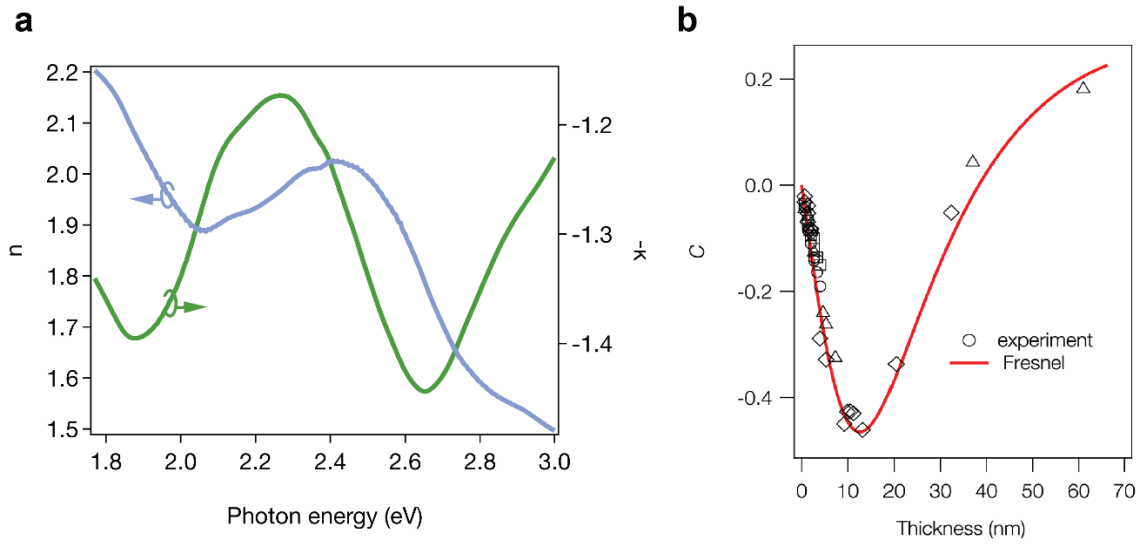

Figure 2.4. Computed index of refraction of bulk CrI_3 and Fresnel fit to experimental contrast values of exfoliated CrI_3 at 631 nm. (a) Real (n, blue) and imaginary (k, red) components are plotted as a function of photon energy in the visible range. (b) Comparison of the experimental contrast data with the computed thickness dependence of C for a red-light-illuminated sample. The different shape markers indicate data coming from different sets of exfoliated samples. The complex index of refraction used for CrI_3 is 1.95-1.35i. Reproduced from ref. [34].

The calculated index of refraction for bulk CrI_3 is shown in Fig. 2.4a as a function of photon energy. At 631 nm or ~1.97 eV, the index of refraction is ~1.95-1.35*i*. The contrast of CrI_3 on 285 nm SiO_2/Si substrate at 1.97 eV is plotted as a function of flake thickness in Fig. 2.4b. Experimental values of the contrast for a wide range of flake thicknesses match the Fresnel fit well, establishing a concrete optical method by which to identify the layer number of exfoliated CrI_3 flakes.

2.3 AIR SENSITIVITY OF CrI_3 FLAKES

Although single macroscopic crystals of CrI_3 appear to be stable in air, microscopic flakes of ultrathin CrI_3 cleaved from their parent crystal immediately degrade, posing a significant challenge towards measuring the magnetic properties of atomically thin flakes. This can be partially avoided by exfoliating CrI_3 flakes inside a glove-box filled with inert gas such as N_2 or Ar_2, though the issue remains of how to transport the air-sensitive flakes to an atomic force microscope for measuring their thickness, or to a cryostat for probing their magnetic properties. One initial attempt was to place a flake of hexagonal boron nitride (h-BN), an insulating vdW material, on top of a target CrI_3 flake. The atomically sharp interface formed between the h-BN and the CrI_3 layers, in principle, ensures that air cannot penetrate the hBN barrier and react with CrI_3, and is a prevalent method in protecting air-sensitive exfoliated vdW flakes from degradation[6,47].

However, CrI_3 flakes continued to degrade despite being protected from an h-BN capping layer. That is because the main mechanism by which CrI_3 flakes degrade is through a photocatalytic reaction with water vapor[48]. Since h-BN is hydrophilic and the interface between the h-BN and surrounding SiO_2 is not atomically smooth due to the roughness of the SiO_2, we speculate that water vapor can still penetrate through the hBN-SiO_2 interface and react with the underlying CrI_3 flake (Figure 2.5a).

Instead, we came up with two solutions. The first method was to sandwich CrI_3 flakes between two flakes of h-BN (Figure 2.5b). The atomically flat interface between the two hBN flakes surrounding the sandwiched CrI_3 flake successfully prevents water vapor from seeping between the hBN flakes, evidenced by CrI_3 flakes remaining intact despite sitting in ambient conditions for >15 days[48]. Unfortunately, this sealing technique does not work for CrI_3 monolayers as the elevated temperatures, up to 170° C, required to sandwich the CrI_3 flake between the h-BN flakes leads to degradation of the CrI_3 monolayer.

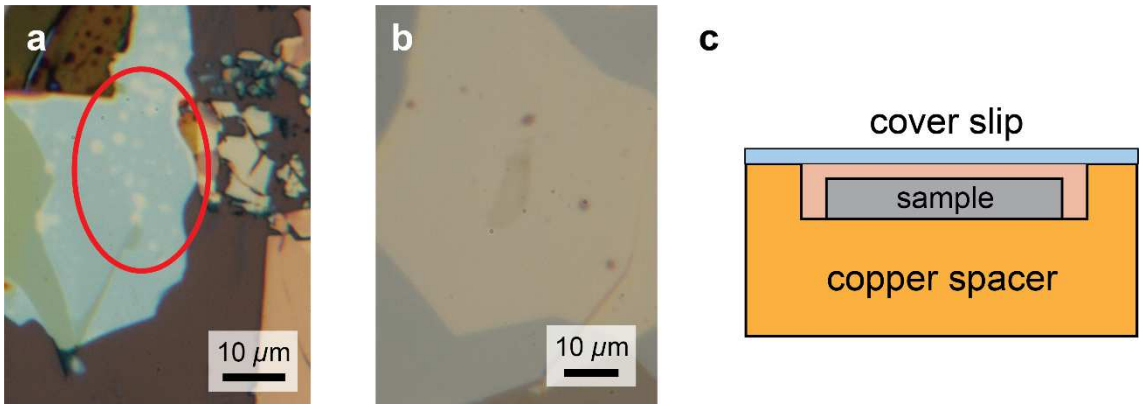

Figure 2.5. Overcoming fabrication challenges. (a) Optical image of CrI_3 monolayer covered on top by h-BN. Clear spots of degradation can be seen at the edge of the monolayer in the red circle. The monolayer is not visible when covered by h-BN. Scale bar is 10 μm. (b) Optical image of trilayer CrI_3 that is sandwiched between two flakes of h-BN. There is no evidence of water residue or degradation on the CrI_3 flake. (c) Side view of the copper spacer. The wafer which the sample is exfoliated on sits just below the lip of the spacer. This allows for optical accessibility with a low working distance aspheric lens. A thin cover slip held down to the spacer by grease forms a seal that traps inert atmosphere in the sample space.

Therefore, to safely transport CrI_3 flakes of all thicknesses in ambient conditions, we created sealable sample carriers which could hold an inert atmosphere while CrI_3 flakes were brought from the glove box to the cryostat. The main body of the sealable sample carrier was a copper "spacer", a piece of flat, oxygen-free high thermal conductivity copper with a small dip

milled out in the middle (Figure 2.5c). This small dip was milled to a depth slightly larger than the thickness of a SiO_2/Si wafer such that the SiO_2/Si wafer sat below the lip when mounted in the small dip. Surrounding the dip was a polished lip upon which we fix a ~100-μm thick glass slip with high-vacuum grease. The barrier formed by the glass slip and the hydrophobic high vacuum grease successfully keeps air out while trapping inert atmosphere within the sample space when the sample carrier is taken out of the glove box.

2.4 MOKE: AN OPTICAL PROBE FOR 2D MAGNETISM

Another substantial challenge to studying 2D magnetism in these atomically thin materials is finding a suitable probe that can detect their magnetic order. While conventional SQUID magnetometry is an effective probe of large magnetic moments in bulk crystals, down to ~500 *n*emu resolution, these probes cannot detect the miniscule magnetic moments (~a few *n*emu for a monolayer of CrI_3) of exfoliated ultrathin vdW materials. Direct methods of detecting the magnetic lattice such as neutron diffraction or X-ray circular dichroism are also unfeasible due to the small scattering cross-section of exfoliated flakes (lateral areas around (10 x 10) μm^2). Lastly, electrical transport is not possible since CrI_3 is insulating below 100 K.

To overcome this difficulty, we look to previous work which dealt with similar challenges and constraints in detecting the magnetic order of ultrathin transition metal films[49]. Two of the most prevalent techniques used to characterize the magnetic properties of thin films were anomalous Hall effect (AHE) measurements[49] and polar magneto-optical Kerr effect (MOKE) microscopy[50]. In the anomalous Hall effect, charge carriers in an electrically conductive material with net out-of-plane magnetization experience an anomalous velocity perpendicular to their direction of motion due to a combination of spin-orbit coupling and scattering mechanisms[51]. However, since CrI_3 is electrically insulating below 100 K[52], AHE measurements are not possible.

Polar MOKE microscopy, on the other hand, is an optical technique that detects rotations of reflected linearly polarized light due to the magnetic circular birefringence of an out-of-plane magnetized sample[53]. This Kerr rotation of linearly polarized light, θ_K, due to MOKE depends on the excitation energy of the incident light and can be enhanced by resonantly exciting on an optical transition that exhibits strong spin-splitting from exchange interaction[53]. Furthermore, incident light can be focused down to a diffraction-limited beam spot (~1 μm), allowing for precise spatial mapping of magnetic order and domains in exfoliated CrI_3 flakes.

These advantages led us to design and build our own MOKE microscope to probe the magnetic order of atomically thin CrI_3, detailed in ref. [34] and illustrated below in Figure 2.6. Since θ_K is expected to be extremely small for monolayer systems[54] we use an AC polarization modulation lock-in amplification technique that can measure rotations down to 100 μrad (further discussion in ref. [55]). CrI_3 samples are cooled down to 15 K in the sample chamber of a Montana Instruments cold-finger cryostat and magnetic fields up to 7 T can be applied in the Faraday geometry (out-of-plane) using a Cryomagnetics superconducting magnet. Samples are excited by a red HeNe laser (1.96 eV) which is nearly resonant with a CrI_3 metal-to-ligand charge transfer transition at 2 eV.

One notable difference in the design of our MOKE microscope is the beam splitter used to divert reflected light to the photodiode. This could be problematic for sensitive polarization measurements such as MOKE since *s*- and *p*- component reflections from a typical beam splitter are anisotropic. To address these concerns we came up with two solutions: (1) use a laser line non-polarization beam splitter cube that provide equal *s*- and *p*- reflections in both amplitude and phase; (2) set a non-polarizing beam splitter to reflect the collection path at as close to normal incidence as possible. Using a 90 nm Ni thin film grown on SiO_2/Si substrate as a standard, we performed a

magnetic field sweep at room temperature of its MOKE signal (Fig. 2.7a) to determine if there any deviations to the MOKE signal incorporating these solutions. Given that the MOKE intensities, shape of the hysteresis curve, and the magnetic fields required to saturate the magnetization of Ni are all consistent with previous MOKE studies seen in Fig. 2.7b[56], it is clear that there is no impact on our MOKE measurements by using a beam splitter.

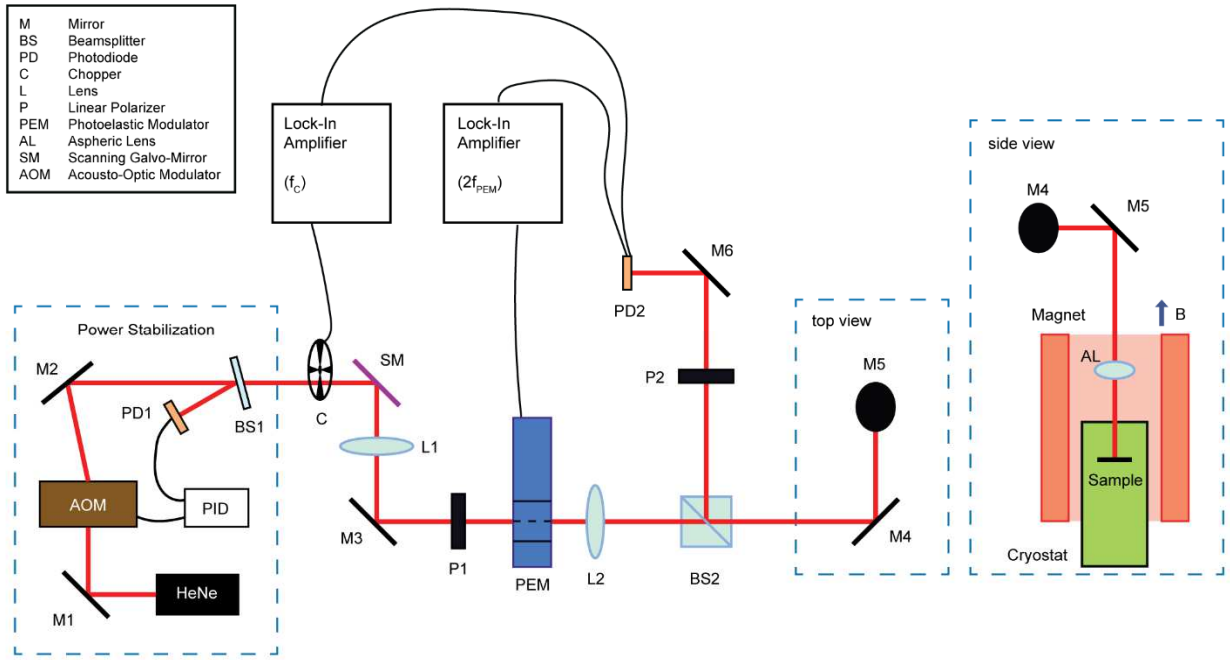

Figure 2.6. Magneto-optical Kerr effect experimental setup. Schematic of the optical setup used to measure Magneto-optical Kerr effect in CrI_3 samples. 633 nm optical excitation is provided by a power-stabilized HeNe laser. A mechanical chopper and photoelastic modulator provide intensity and polarization modulation, respectively. The modulated beam is directed through a non-polarizing beam splitter to the sample, housed in a closed-cycle cryostat at 15 K. A magnetic field is applied at the sample using a solenoidal superconducting magnet in the Faraday geometry. The reflected beam passes through an analyzer onto a photodiode, where lock-in detection measures the reflected intensity (at f_C) as well as the Kerr rotation (at $2f_{PEM}$). For reflective magnetic circular dichroism measurements, polarizer P2 is removed and lock-in detection of the magnetic circular dichroism signal is instead at f_{PEM}. Reproduced from ref. [34].

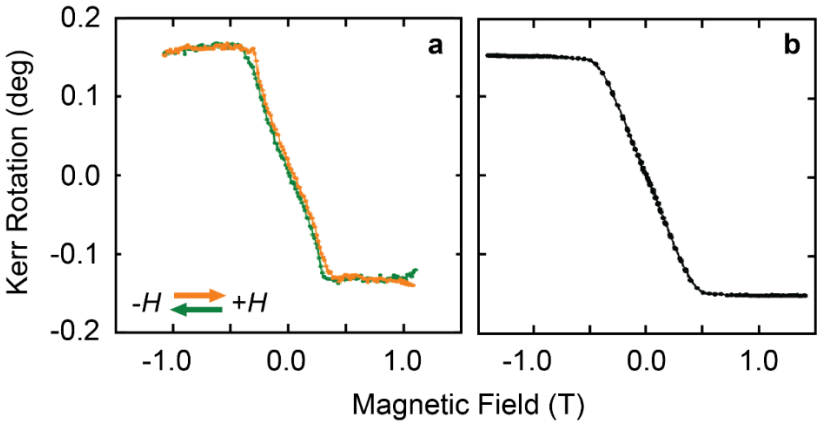

Figure 2.7. Magneto-optical Kerr microscopy on 90-nm Ni thin films. (a) Kerr rotation signal as a function of magnetic field measured in our lab on a 90-nm Ni thin film evaporated on 90-nm SiO_2/Si wafer. The green (orange) curve represents signal taken as the field is swept down (up) toward negative (positive) fields. (b) The same measurement as (a) taken in Višňovský *et al.* Both panels show virtually identical behavior of the Kerr signal, confirming that our MOKE setup is calibrated well. Panel (b) adapted from ref. [56] with permission from *ScienceDirect.*

2.5 2D FERROMAGNETISM OF CrI_3 MONOLAYERS

Through the sample preparation and measurement techniques that we developed, we successfully exfoliate and measure the magnetic properties of monolayer CrI_3[34]. In Fig. 2.8a, magnetic field-dependent MOKE measurements of a CrI_3 monolayer at a temperature of 15 K (optical image in Fig. 2.8a inset) clearly shows magnetic hysteresis, a hallmark of ferromagnetism that confirms the discovery of the first monolayer ferromagnetic insulator. The observed θ_K from the monolayer is ~5 mrad. Moreover, the ratio of the remanent MOKE signal at $\mu_o H = 0$ T and the signal at magnetic saturation is virtually unity *i.e.* the hysteresis curve is square, implying that the ferromagnetism in monolayer CrI_3 is highly anisotropic. The coercivity is around 50 mT for the monolayer as shown in Fig. 2.8a, though this varies across monolayers due to domain formation as we will discuss below. The MOKE signal and hysteresis are not affected by the laser power used, as seen in Fig. 2.8b, so a fixed power of 10 μW is used for all subsequent MOKE measurements.

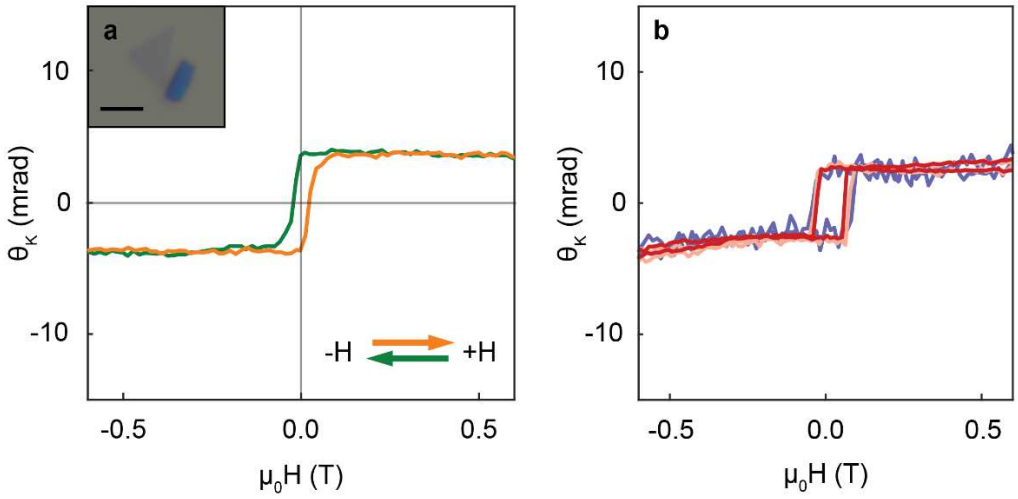

Figure 2.8. Ferromagnetism in CrI_3 detected through magneto-optical Kerr effect. (a) Kerr signal, θ_K, as a function of magnetic field of a representative monolayer CrI_3. The green (orange) curve represents signal taken as the field is swept down (up) toward negative (positive) fields. Optical image of a monolayer flake (faded purple) is in the upper-left inset. The scale bar is 2 μm. (b) Power dependence of MOKE signal taken at incident powers of 3 μW (blue), 10 μW (pink), and 30 μW (red). Reproduced from ref. [34].

Spatial mapping of the MOKE signal across the monolayer flake also reveals the presence of magnetic domains. In the left panel of Fig. 2.9a, the entire flake exhibits negative θ_K (blue in the spatial map) and hence is magnetized in the spin-down configuration when cooled to 15 K without an applied magnetic field. When the magnetic field is swept up to $\mu_o H$ = 0.15 T, part of the flake in the middle panel of Fig. 2.9b undergoes a magnetization reversal to the spin-up configuration, evidenced by the positive θ_K signal displayed as red in the upper-half of the flake. After sweeping the magnetic field to $\mu_o H$ = 0.3 T, the magnetization of the lower domain reverses, leading to a single magnetic domain across the flake that is in the spin-up configuration (Fig. 2.9c, right panel). These MOKE spatial maps indicate that the flake is split into two magnetic domains that are ~1 μm x 1 μm in lateral area and have different coercivities.

Parking the laser on different parts of the flake and measuring the MOKE response as a function of magnetic field further confirms this notion. When the laser is parked entirely on the upper domain (green circle, Fig. 2.9d), the resulting magnetic hysteresis has a coercivity of ~50 mT. This is lower than the coercivity observed from the lower domain (purple circle, Fig. 2.9d) which has a value of 200 mT. Of course, when the beam spot is parked between the two domains (green and orange circles, Fig. 2.9d), the MOKE signal reflects the magnetization reversal of both domains. All of these observations are consistent with the magnetization reversal seen in the field-dependent MOKE spatial maps.

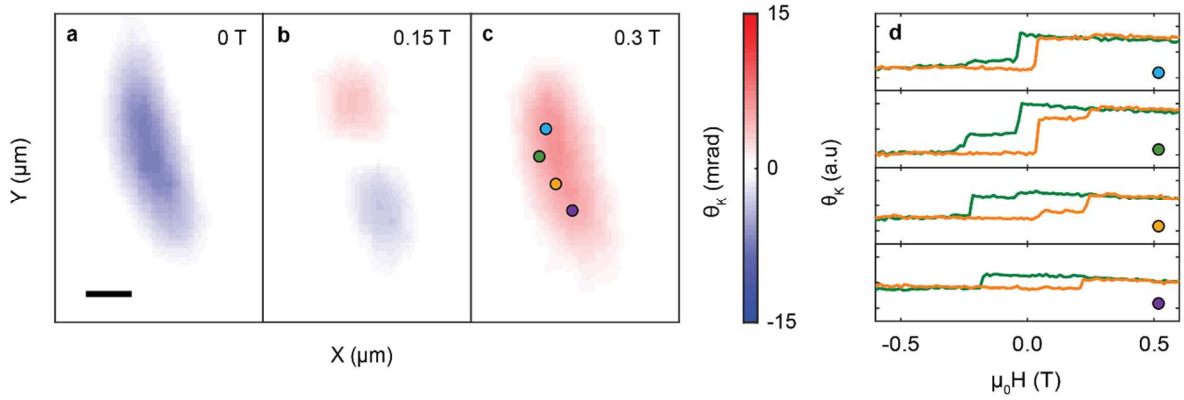

Figure 2.9. Magnetic domains in monolayer CrI_3. (a-c) MOKE maps at (a) $\mu_o H = 0$ T, (b) 0.15 T, (c) and 0.3 T on a different monolayer. The scale bar is 1 μm. (d) θ_K vs. $\mu_o H$ sweeps taken at four points marked by dots on the $\mu_o H = 0.3$ T map in (c). Reproduced from ref. [34].

To probe for any differences in T_C between monolayer and bulk CrI_3, we performed temperature-dependent MOKE field sweeps as shown in Fig. 2.10. Starting at 15 K, the remanent MOKE signal and coercivity both noticeably decrease as the temperature increases. Upon reaching ~45 K, the remanent MOKE signal *i.e.* spontaneous magnetization goes to zero as any magnetic hysteresis disappears, indicating a magnetic transition from ferromagnetic order to paramagnetism. These measurements suggest that the T_C of monolayer CrI_3 is ~45 K, only slightly lower than the bulk CrI_3 T_C of 61 K. This suggests that, unlike previous 2D ferromagnetic films where T_C drops

rapidly approaching a single layer, the strong out-of-plane anisotropy in monolayer CrI_3 stabilizes magnetic order in the 2D limit.

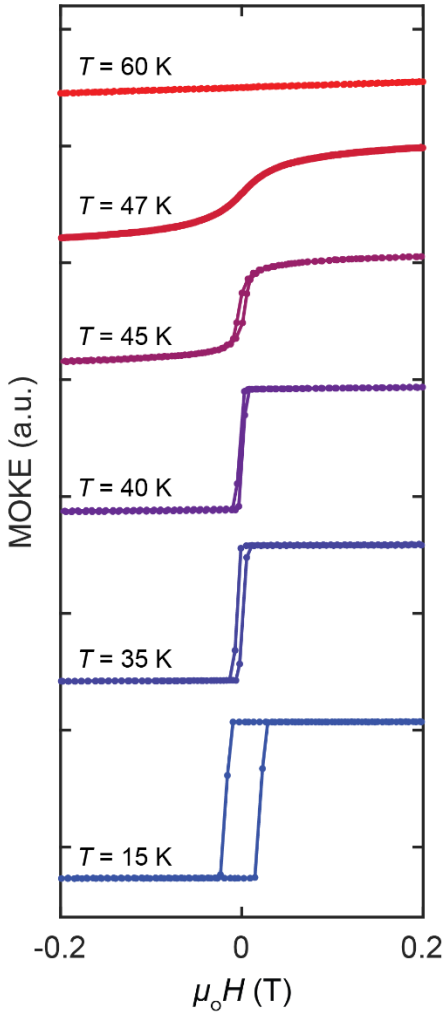

Figure 2.10. Temperature-dependent ferromagnetism in monolayer CrI_3. MOKE hysteresis curves of monolayer CrI_3 taken at select temperatures. An obvious decrease in the coercivity is seen warming up from 15 K until at ~45 K, the loop disappears and the monolayer enters the paramagnetic phase. Adapted from ref. [57].

2.6 Layered antiferromagnetism in few-layer CrI_3

Since both monolayer and bulk CrI_3 are ferromagnetic, it is expected then that flakes of all thicknesses in between these two extremes also display ferromagnetism. It is even more surprising

then that unlike monolayer CrI_3 flakes which exhibit magnetic hysteresis (Fig. 2.8a), bilayer CrI_3 flakes give zero MOKE signal, indicating the lack of a net out-of-plane magnetization for its magnetic ground state. If the magnetic field is swept past 0.7 T, an abrupt increase of the MOKE signal is observed (Fig. 2.11), with a θ_K of ~40 mrad. When ramping the magnetic field back down to 0 T from above 0.7 T, the MOKE signal drops back to zero at around 0.7 T. The sudden onset of magnetization also occurs when the magnetic field is swept toward negative fields: sweeping past -0.7 T, the MOKE signal becomes large and negative, roughly the same in magnitude as the positive MOKE signal observed above 0.7 T. Also peculiar is that θ_K in bilayer CrI_3 flakes is almost an order-of-magnitude larger than the θ_K observed in the monolayer, despite only doubling in the total magnetic moment. This is due to thin-film interference from the underlying SiO_2 substrate and is modeled in Appendix I.

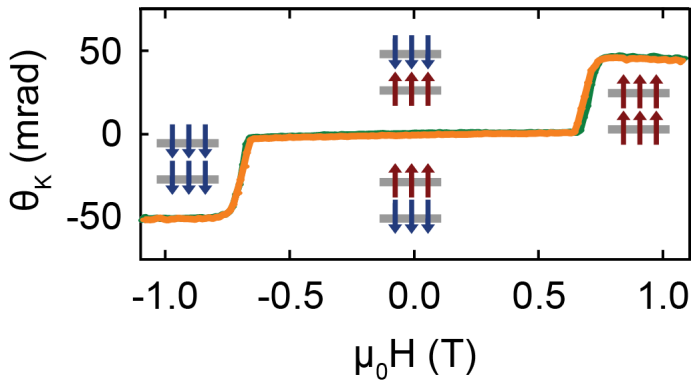

Figure 2.11. Layered antiferromagnetism in bilayer CrI_3. MOKE signal, θ_K, from a bilayer CrI_3 showing vanishing Kerr rotation for applied fields between ±0.65 T, suggesting antiferromagnetic behavior. Insets depict bilayer magnetic ground states for different applied fields. Reproduced from ref. [34].

It is clear then that the magnetic response of the bilayer is not ferromagnetic: it lacks magnetic hysteresis and exhibits sudden onsets of magnetization with applied magnetic fields. So, what is the ground state of the bilayer? One possibility is that the bilayer has in-plane spins since

the polar MOKE signal would be zero. However, this is ruled out since an out-of-plane field would lead to the canting of spins and hence a gradual increase in the MOKE signal. Rather, given the large out-of-plane magnetic anisotropy in both the monolayer and bulk CrI_3, the magnetic anisotropy of bilayer CrI_3 should also be strongly out-of-plane, implying that the anisotropy should be independent of thickness. This idea is consistent with the fact that the anisotropy of CrI_3 is primarily determined by intralayer superexchange interactions[42]. Lastly, DFT calculations show that intralayer magnetic order is strongly ferromagnetic in both monolayer and bulk CrI_3, on the order of a few meV[37].

Armed with this information, we conclude that bilayer CrI_3 is an A-type (or layered) antiferromagnet: the magnetic ground state consists of two ferromagnetic layers which are coupled antiferromagnetically (see cartoons in Fig. 2.11). A modest applied magnetic field of ±0.7 T then is enough to cause a spin-flip transition to a state where the magnetizations of both layers are fully magnetized along the applied field direction. This explains the abrupt increase in MOKE signal, and large, but opposite sign, signals between the two magnetic states at 0.7 T and -0.7 T.

We also find that the interlayer antiferromagnetic coupling is weak, with an energy scale roughly equivalent to the Zeeman energy of the applied magnetic field. This can be estimated through a mean-field approach by using an averaged layer magnetization, $\langle M_i \rangle$, to formulate a Hamiltonian, $\widehat{H}$, that takes into account the interlayer exchange interaction between $\langle M_1 \rangle$ and $\langle M_2 \rangle$ as well as the Zeeman term with the external magnetic field, $\mu_o H$. This is valid since, as we will find, interlayer exchange coupling is much weaker in CrI_3 than its intralayer exchange. We also only consider nearest-neighbor exchange interactions as next-nearest and next-next-nearest interactions are much weaker[58–61]. Thus, the resulting Hamiltonian takes the form:

$$\widehat{H} = J\frac{\langle M_1 \rangle \cdot \langle M_2 \rangle}{{\mu_B}^2} - (\langle M_1 \rangle + \langle M_2 \rangle) \cdot \mu_o H,$$

where J is the interlayer exchange constant and is positive for antiferromagnetic interactions, and μ_B is the Bohr magneton. Since the individual layers are either fully polarized spin-up or spin-down, $\langle M_1 \rangle$ and $\langle M_2 \rangle$ are just the expected magnetic moment per Cr^{3+}, $g\mu_B S$, where g is the gyromagnetic ratio and S is the spin quantum number. In the antiferromagnetic states, $\langle M_1 \rangle = -\langle M_2 \rangle = g\mu_B S$, eliminating the Zeeman term and simplifying the Hamiltonian:

$$\widehat{H}_{AFM} = -J(gS)^2.$$

In the spin-polarized states, $\langle M_1 \rangle = \langle M_2 \rangle$, so the Hamiltonian takes the form:

$$\widehat{H}_{FM} = J(gS)^2 - 2g\mu_B S \cdot \mu_o H.$$

Determining the magnetic state at a specific magnetic field, $\mu_o H$, simply involves determining whether $\widehat{H}_{AFM} - \widehat{H}_{FM}$ is positive (favoring ferromagnetism) or negative (favoring antiferromagnetism). $\widehat{H}_{AFM}$ is negative definite and does not depend on the magnetic field. However, the Zeeman term in $\widehat{H}_{FM}$ becomes increasingly negative as $\mu_o H$ increases. This implies that magnetic switching will occur between the two magnetic states when $\widehat{H}_{AFM} - \widehat{H}_{FM} = 0$ at some spin-flip field, $\mu_o H_{sf}$. Therefore, the expression when $\widehat{H}_{AFM} - \widehat{H}_{FM} = 0$ is:

$$-2J(gS)^2 + 2g\mu_B S \cdot \mu_o H_{sf} = 0.$$

Since we have a numerical value for $\mu_o H_{sf}$ of bilayer CrI_3 from our MOKE measurements, we can derive an expression to solve for the interlayer exchange. This expression for J is:

$$J = \frac{\mu_B \mu_o H_{sf}}{gS},$$

The gyromagnetic ratio in this calculation is assumed to be 2, the same as a free electron, S is the sum of the three electron spins presiding in the triply degenerate t_{2g} orbitals which is 3/2, and $\mu_o H_{sf}$, is 0.7 T. Thus, the resulting interlayer exchange strength, J, is on the order of tens of μeV, two orders of magnitude smaller than the intralayer exchange strength. One can also compare

the interlayer exchange strength to the dipolar interactions by calculating for a square lattice, the magnetostatic interactions from all spins in one layer on a single spin in the second layer. The magnetostatic energy is derived in Appendix II and is estimated to be fractions of μeV, several order-of-magnitudes lower than J.

MOKE measurements of tri- and four-layer CrI_3 flakes further confirm the notion of layered antiferromagnetic order in few-layer CrI_3, summarized in Fig. 2.12a-d[62]. As shown in Fig. 2.12c&d, staircase-like switching behavior is also observed in the magnetic field-dependent MOKE signal of tri- and four-layer, similar to the spin-flip behavior seen in the bilayer. Unlike the bilayer, however, there are more intermediate magnetic states in the tri- and four-layer flakes, with N+1 magnetization plateaus for an N-layer flake for N up to 4. Therefore, magnetic switching is not an all-at-once phenomena where all layers reverse simultaneously, and instead switch layer-by-layer that results in discrete $2M_s/N$ jumps in the magnetization, where M_s is the saturation magnetization.

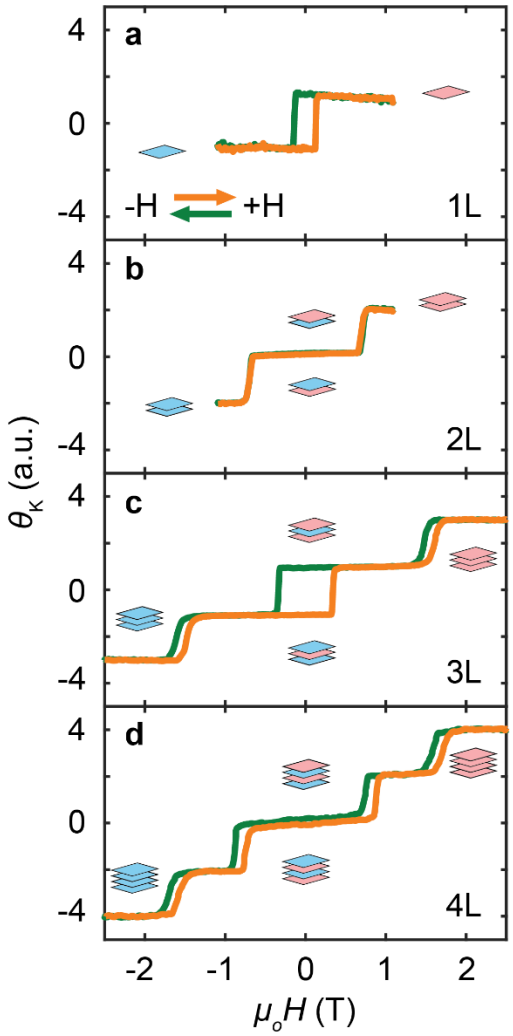

Figure 2.12. Layer-dependent 2D magnetism in atomically thin CrI_3. Kerr signal, θ_K, of (a) mono-, (b) bi-, (c) tri-, (d) and four-layer CrI_3 as a function of magnetic field. The green (orange) curve shows MOKE data taken as the magnetic field is swept down (up). The MOKE measurements for the monolayer and bilayer samples in (a) and (b) were taken at 15 K. The trilayer and four-layer Kerr signals in (c) and (d) were measured at 2 K. Cartoons illustrate the magnetic ground states and ferromagnetic-like states, with red (blue) squares representing a layer that is magnetized in the spin-up (spin-down) direction. Reproduced from ref. [38].

2.7 Differences in magnetic order between few-layer and bulk CrI_3

Interlayer magnetic order is clearly different in exfoliated few-layer CrI_3 compared to the bulk. Whereas few-layer CrI_3 hosts antiferromagnetic interlayer exchange, bulk CrI_3, on the other hand

contains ferromagnetic interlayer interactions. Since exchange interactions in general depend on the separation distances and geometry of ions in a crystal lattice, we take a closer look at how stacking order and magnetism are correlated in CrI_3.

As explained in Section 2.1, bulk CrI_3 has two structural phases: the monoclinic phase at high temperature (>200 K) and the rhombohedral phase at low temperature. Clearly, since T_C is below the structural transition temperature of bulk CrI_3, the crystal is in the rhombohedral phase when it becomes ferromagnetic below 61 K. In few-layer CrI_3, recent work using second harmonic generation (SHG)[63] and Raman spectroscopy[64–66] have found that these 2D flakes are stacked in the monoclinic phase at both room temperature and low temperature when the flakes display layered antiferromagnetism. These experimental findings are consistent with DFT calculations[58–61], which show that rhombohedral-stacked and monoclinic-stacked CrI_3 display ferromagnetic and layered antiferromagnetic order, respectively. This difference in stacking order in few-layer CrI_3 flakes is a surprising departure from bulk CrI_3 and implies that exfoliated flakes are essentially pinned in the bulk high-temperature structural phase. Given that the rhombohedral and monoclinic phases are nearly degenerate[58], perturbations from strain induced from the substrate or during the exfoliation process could further break this degeneracy and favor the monoclinic phase in 2D flakes.

We now look at the microscopic mechanisms of interlayer exchange in CrI_3. While chromium ions within a layer are only separated by around 4 Å[35], this separation distance already leads to a significant reduction in direct antiferromagnetic exchange interactions. This explains why the ferromagnetic superexchange interaction dominates and the monolayer displays ferromagnetic order and not antiferromagnetic order. On the other hand, the interlayer separation distance is around 7 Å[35,58], almost double the intralayer Cr^{3+}-Cr^{3+} separation distance. At these

large separation distances, the main mechanism for interlayer exchange is super-superexchange (SSE), virtual electron hopping between the Cr^{3+} *d* orbitals through the *p* orbitals of *two* I^- anions (Fig. 2.13)[58–61]. The mechanism of virtual hopping relies on orbital overlap between ions, so the relative positions of each ion and hence the layer configuration play a crucial role in determining the resultant interlayer exchange.

Furthermore, virtual electron hopping is a spin-conserved process. As such, any virtual hopping between the Cr t_{2g} orbitals is forbidden in the ferromagnetic state due to the Pauli exclusion principle (Fig. 2.13a). SSE pathways that involve the hybridization of two Cr^{3+} t_{2g} orbitals must therefore give rise to antiferromagnetic exchange. Analyzing the bilayer CrI_3 SSE pathways of the nearest and next-nearest neighbor interlayer Cr^{3+} pairs in the rhombohedral phase, we find that the nearest-neighbor SSE pathway, $J_{1\perp}$, links two t_{2g} orbitals (Fig. 2.13b&c), while the next-nearest-neighbor SSE pathway, $J_{2\perp}$, connects a t_{2g} orbital to an empty e_g orbital (Fig. 2.13d)[58]. Thus, $J_{1\perp}$ gives rise to antiferromagnetic exchange while $J_{2\perp}$ results in ferromagnetic exchange. Given that the exchange energy of $J_{1\perp}$ and $J_{2\perp}$ are of the same order-of-magnitude and that there are 16 $J_{2\perp}$ SSE interactions in a unit cell versus one $J_{1\perp}$ SSE interaction per unit cell, ferromagnetic exchange clearly dominates in rhombohedral-stacked CrI_3 (roughly 0.6 meV/μ_B)[58].

In the monoclinic phase, the relative translational shift between the CrI_3 layers differs from the rhombohedral phase, leading to changes in the geometry of the SSE interactions. Despite this, the orbital overlap of the interlayer Cr^{3+} and I^- sites in both the nearest-neighbor (Fig. 2.13e&f) and next-nearest neighbor interactions are in essence the same, *i.e.* $J_{1\perp}$ and $J_{2\perp}$ remain antiferromagnetic and ferromagnetic, respectively. What does change, however, are the number of SSE interactions in the unit cell. In the monoclinic phase, both $J_{1\perp}$ and $J_{2\perp}$ have two interactions per unit cell, dramatically lowering the ferromagnetic contribution to the super-superexchange.

Since the exchange strength of $J_{1\perp}$ is marginally larger than that of $J_{2\perp}$[58–61], the resulting ground state in the monoclinic phase is layered antiferromagnetism.

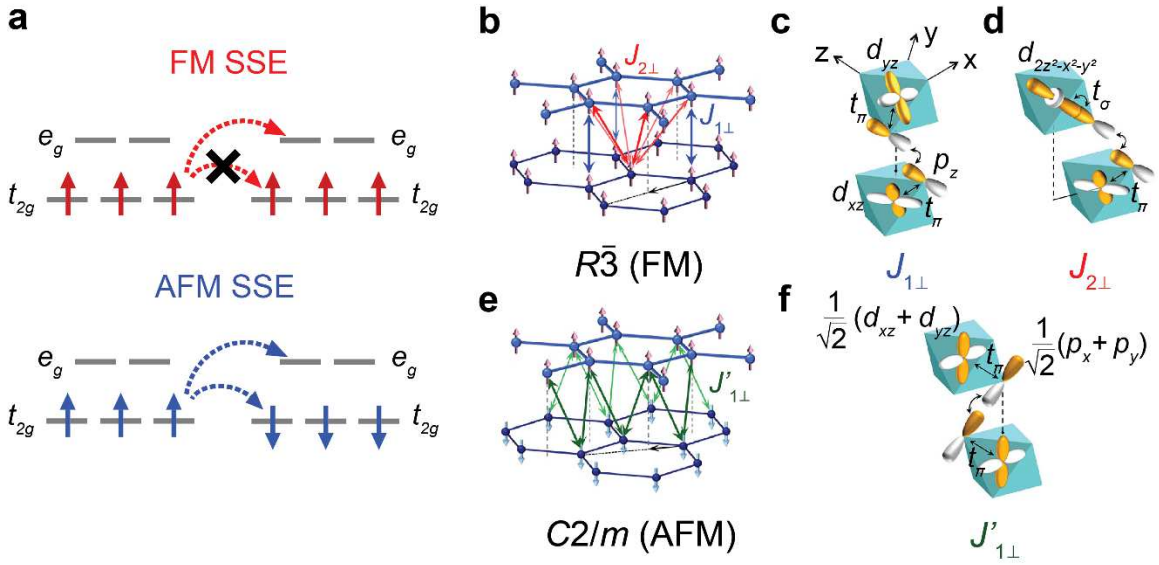

Figure 2.13. Interlayer super-superexchange pathways in bilayer CrI_3. (a) Overview of possible electron hopping scenarios for an interlayer ferromagnetic (FM) super-superexchange (SSE) pathway (red) and an interlayer antiferromagnetic (AFM) SSE pathway (blue). Hopping is only allowed between the t_{2g} and e_g orbitals in the FM SSE pathway, which further reinforces the FM order through Hund's coupling. (b-f) Interlayer SSE pathways between Cr^{3+} of adjacent layers in the (b-d) rhombohedral phase and (e-f) monoclinic phase. Summing all interlayer SSE pathways results in ferromagnetic order in rhombohedral-stacked bilayers and layered antiferromagnetic order in monoclinic-stacked bilayers. Panels (b)-(f) reproduced from ref. [38].

Similar behavior is observed in the other chromium trihalides. Like bulk CrI_3, bulk $CrCl_3$ exhibits a structural phase transition between the high-temperature monoclinic phase and the low-temperature rhombohedral phase at ~220 K[67,68]. While the magnetic order is identical between exfoliated flakes and unexfoliated bulk crystals, both displaying easy-plane layered antiferromagnetism, differences in their stacking order result in an order-of-magnitude larger interlayer exchange strength in ultrathin flakes[67,68]. Although a structural transition is absent below

room temperature in bulk $CrBr_3$, the epitaxial growth of bilayer $CrBr_3$ through molecular beam epitaxy (MBE) can result in films with differing stacking configurations[69] and which display contrasting magnetic behavior.

2.8 SIGNIFICANCE, PARALLEL WORK AND FUTURE DIRECTIONS

In this chapter, we have discovered 2D ferromagnetism in a vdW material. This is a breakthrough for the field of condensed matter physics, bringing opportunities to further explore 2D magnetism using the experimental machinery of vdW materials[13]. Because magnetic 2D flakes are essentially an exposed surface, their magnetic properties are highly susceptible to external tuning parameters such as electrostatic gating and fields[70–72], pressure[64,65], and strain[73]. Their universal compatibility with other vdW materials also enable flexible heterostructure design without lattice-matching constraints[13,71,74]. This could be leveraged to realize new spin-[71,75–77] and valleytronics[78,79] devices, and investigate the interplay between magnetism, topology, and other many-body phases[80,81].

Ferromagnetic order in monolayer CrI_3 is also the first realization of a 2D ferromagnetic insulator. This could provide new opportunities to explore how magneto-optical effects in the 2D limit differ from the bulk case. For instance, how are excitons affected by 2D magnetic order and is there an expected spontaneous helicity? What consequences does symmetry breaking have that affects the ways 2D magnets couple to light? Could we potentially form magnetic interlayer excitons in heterostructures with other materials? Answering these questions could lead to exciting physics discoveries and unprecedented opto-spintronic applications.

Besides CrI_3, 2D magnetism has also been investigated in other monolayer vdW crystals, with select magnets highlighted in Table 2.2[70–72]. $CrGeTe_3$[82], a soft ferromagnetic semiconductor, was shown to exhibit unusually high responsivity to magnetic fields in the few-layer limit. This demonstrates that even though 2D magnetism is suppressed by thermal fluctuations, these spins

still exhibit strong magnetic susceptibilities and so readily align to external applied magnetic fields. $FePS_3$[30,83], an Ising-like antiferromagnetic insulator, was shown to exhibit magnons[84] and splitting of its phonons below its Neél temperature (T_N) due to phonon zone folding. These signatures were used to identify a layer-independent T_N down to the monolayer limit, leading to the first discovery of 2D antiferromagnetic order in vdW materials. The list of discoveries goes on: intrinsic topological magnetic insulators exhibiting the quantum anomalous Hall effect ($MnBi_2Te_4$)[81,85,86]; isotropic monolayers for investigating magnetic vortices and the Berezinskii-Kosterlitz-Thouless transition ($CrCl_3$)[67,68,87]; epitaxially grown room-temperature 2D ferromagnets ($MnSe_x$)[88]. The possibilities, therefore, are endless in the different combinations of magnetic heterostructures that could be formed using these newly discovered magnetic vdW crystals.

Table 2.2 – Select magnetic vdW crystals, their properties, and crystal structures[38]

Material	Magnetic Order	T_C / T_N (K)	Band Gap[b] (eV)	Additional Notes	Crystal Structure
$FePS_3$	$AFM^{\perp}$	118	1.6	Zigzag	MAX_3 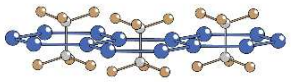
$NiPS_3$	$AFM^{\parallel}$	148[a]-166[b]	1.7	Zigzag, slight tilt out-of-plane	
$MnPS_3$	AFM	78	3.0	Neél, isotropic	
$CrGeTe_3$	$FM^{\perp}$	<5[a]-61[b]	0.38		
Fe_3GeTe_2	$FM^{\perp}$	70[a]-221[b]	metallic		Fe_3GeTe_2 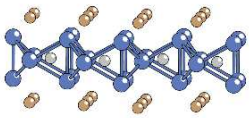
Fe_5GeTe_2	$FM^{\perp}$	270[a]-310[b]	metallic		
$MnBi_2Te_4$	$L\text{-}AFM^{\perp}$	21	0.1	Intrinsic magnetic topological insulator L-AFM: Intralayer FM, interlayer AFM	$MnBi_2Te_4$ 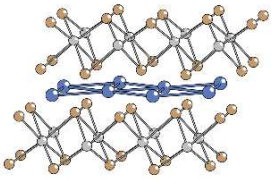
VSe_2	$FM^{a,\parallel}$	>300[a]	metallic	T_{CDW} ~ 130 K MBE-grown	MSe_2 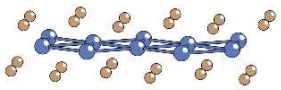
$MnSe_x$	$FM^{a,\perp}$	>300[a]	3.4	MBE-grown	
CrI_3	$L\text{-}AFM^{a,\perp}$ $FM^{b,\perp}$	45[a]-61[b]	1.2		CrX_3 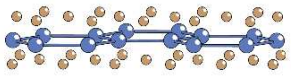
$CrBr_3$	$FM^{\perp}$	20[a]-37[b]	2.2		
$CrCl_3$	$L\text{-}AFM^{\parallel}$	17	3.0		

[a]Atomically thin [b]Unexfoliated bulk $^{\parallel}$In-plane anisotropy $^{\perp}$Out-of-plane anisotropy
FM = ferromagnet AFM = antiferromagnet L-AFM = layered antiferromagnet

Chapter 3. ELECTRICAL CONTROL OF 2D MAGNETISM IN BILAYER CrI_3

In the previous chapter, we went over the discovery of 2D magnetism in vdW materials, particularly in the magnetic insulator, CrI_3. This discovery unlocks new possibilities to control magnetism in the 2D limit through experimental techniques that are unique to the platform of vdW materials. For example, one way to tune the magnetic order in vdW materials is through strain. Exchange mechanisms are directly affected by interatomic distances between ions in a material. By directly applying a force to change these distances, one could potentially induce magnetic phase transitions in a vdW material by altering its exchange interactions and possibly its magnetic anisotropy[73,89,90]. Straining of magnetic vdW materials could be realized in experiment through methods such as their stretching on flexible substrates[91,92], on a piezo stack[93], or substrate textures[94] (pillars, holes, etc.). There has been a recent demonstration of strain tuning of the layered antiferromagnetic order in CrI_3 bilayers[95], though the change in the strain applied is relatively small, roughly 0.2%.

Another degree of freedom by which to control 2D magnetism is the application of pressure, particularly along the out-of-plane direction. One direct consequence of applying pressure, as with strain, is the change in interatomic distances that could lead to tuning of the exchange and anisotropy parameters. However, modest pressures in the few to tens of GPa can also result in structural phase transitions, as was observed in the metal-insulator transition of MoS_2 due to changes in its layer stacking configuration[96]. More recently, pressure-induced magnetic phase transitions have been realized in few-layer CrI_3[64,65], where the application of pressure results in a structural transition from monoclinic stacking to rhombohedral stacking. As we reasoned

through in Chapter 2, this structural transition then leads to an associated magnetic phase transition from layered antiferromagnetism to ferromagnetism.

One of the more coveted methods of controlling magnetism is through the use of electric fields. Simultaneous control over the spin and charge degrees of freedom is particularly useful from a technological standpoint as the successful electrical switching of magnetism could lead to low-power, high-speed solutions for computational and data storage applications[97]. In this chapter, we explore this concept further with magnetic vdW materials, namely by applying electric fields to bilayer CrI_3. This chapter closely follows my work in *B. Huang et al.* "Electrical control of 2D magnetism in bilayer CrI_3" which was published into *Nature Nanotechnology* in 2018[98].

3.1 Electric fields and their effects on spin

It is obvious that the electron charge couples to the electric field and its spin component to magnetic fields. The question though is whether the electron spin can be directly controlled by an electric field. To intuit this, we recall that charges moving relativistically, *e.g.* in a material with large spin-orbit coupling, and in an applied electric field, *E*, also experience an effective magnetic field of the form:

$$B_{eff} = \frac{\boldsymbol{v} \times \boldsymbol{E}}{c^2}$$

where *v* is the velocity of the charged particle, and *c* is the speed of light in the material. This B_{eff} can couple to the spin component of the charged particle[99]. If the particle is a free electron and the electric field is applied in the out-of-plane direction (which we define as the positive z-axis), a momentum-dependent Zeeman energy is imparted on the electron spin which takes the form:

$$H_R = \frac{\mu_B}{mc^2}\boldsymbol{\sigma} \cdot (\boldsymbol{p} \times \boldsymbol{E})$$

where μ_B is the Bohr magneton, p is the momentum of the electron and $\boldsymbol{\sigma}$ is the Pauli spin operator. Note that for this derivation, we use a generalized spin direction which does not necessarily point in the out-of-plane direction. This term, which couples the electron spin to the electric field, is known as the Rashba effect.

Upon closer inspection, however, magnetic 2D materials *e.g.* CrI_3, Fe_3GeTe_2, with strong out-of-plane anisotropy do not exhibit the Rashba effect when an electric field is applied. This is because $\boldsymbol{p} \times \boldsymbol{E}$ is necessarily a vector that lies in the plane, $\boldsymbol{\sigma} \sim \sigma_z \hat{\boldsymbol{z}}$, and so H_R is zero. Furthermore, the Rashba term is odd in $\boldsymbol{p}$, implying that materials with inversion symmetry exhibit no Rashba effect when an electric field is applied[99].

Instead, the first experimental implementation of electrically controlled magnetism leveraged electrostatic gating to modulate the magnetic properties of dilute magnetic semiconductors[100,101]. When chemically doped with magnetic ions such as Mn^+, the III-V semiconductors, GaAs and InAs, display ferromagnetic order that is mediated through Ruderman-Kittel-Kasuya-Yosida (RKKY) exchange interactions between itinerant holes. Changing the itinerant hole density through an applied gate voltage then can lead to tuning of the exchange strength and hence T_C of these dilute magnetic semiconductors. This can lead to significant changes in T_C of around 30% in, for example, $Ga_{1-x}Mn_xAs$ (x = 0.125) which has an unmodified T_C of 33 K.

While conventional electrostatic gating is effective for modifying the magnetic properties of semiconducting and potentially even insulating materials, it is not effective for metals which have short screening lengths and high carrier concentrations of ~10^{23} cm^{-3} or ~10^{15} cm^{-2} in the 2D regime. These issues can be addressed by using an ionic liquid polymer gate to apply giant electric fields on ultrathin metals (~1-2 nm in thickness)[102]. In practice, ionic liquid is cast upon the

ultrathin ferromagnetic metal (FePt, FePd, etc.) and a contact electrode, as illustrated in Figure 3.1. The application of a voltage between the ferromagnetic metal and contact electrode deposits either cations or anions onto the ferromagnetic metal surface depending on the polarity of the applied voltage. This attracts and forms a dense charge layer in the ferromagnetic metal, doping the material by up to 0.015*e* per unit cell in FePt, or ~10^{21} cm^{-2}.

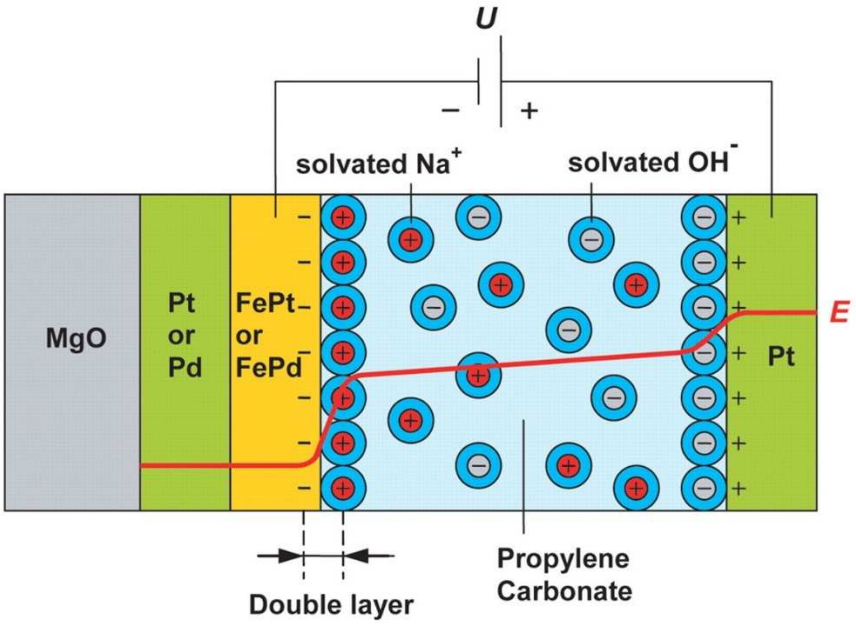

Figure 3.1. Ionic liquid gating of FePt/FePd. NaOH suspended in propylene carbonate is cast onto films of FePt/FePd and an electrically isolated Pt contact. A voltage is applied between the FePt/FePd film and the Pt contact (in this illustration, positive voltage is on the contact side), leading to the dissociation of NaOH and the formation of an Na^+ layer on the surface of the FePt/FePd film and OH^- layer on the Pt contact surface. The Na^+ layer leads to giant electrostatic doping of the FePt/FePd film surface *i.e.* a double layer interface between the ionic liquid and the FePt/FePd film. An illustration of the internal electric field is overlaid. Adapted from ref. [102] with permission from AAAS.

3.2 Electric field control of magnetism in bilayer CrI_3

Electric fields can be readily applied to any target magnetic vdW material by constructing transistors using hBN-graphite gates[103]. Since vdW monolayers are essentially a 2D surface,

electric fields are much more effective in electrostatically doping the monolayer material, with electric fields ~0.8 V/nm possible with high-quality transistor devices[104]. This can be pushed up to several V/nm through ionic liquid gating techniques, which has led to exciting discoveries such as electrically induced superconductivity in a direct-gap semiconductor, monolayer MoS_2[105].

Using well-established sample preparation protocols[106], we fabricate gated bilayer CrI_3 transistors in the geometry shown in Figure 3.2a (optical image of a sample device shown in Fig. 3.2b). In these devices, a flake of bilayer CrI_3 is encapsulated by two flakes of hBN, a graphite top gate, and for a few devices, a graphite bottom gate. A graphite strip also directly contacts the CrI_3 bilayer within the hBN sandwich, acting as the drain/source electrode that modifies the carrier density of the bilayer. The out-of-plane magnetic order in the CrI_3 bilayer devices was measured through polar MOKE and reflectance magnetic circular dichroism (RMCD, see Figure 2.6) microscopy, an optical technique that is similar to MOKE but which detects magnetic circular dichroism rather than birefringence. The experimental design is identical to the setup described in Section 2.3, with one small modification for RMCD measurements: the analyzing polarizer just before the photodiode is removed to measure the reflected intensities of right-circular (σ^+) and left-circularly polarized light (σ^-).

Magnetic field-dependent measurements of the RMCD signal of a representative bilayer device (D1) with zero applied gate voltage are shown in Figure 3.2c. The evolution of the RMCD signal is in general, consistent with the magnetic behavior observed in unencapsulated bilayer flakes. That is, there is a sudden onset of RMCD signal that occurs at around $\mu_o H_c = \pm 0.85$ T when the bilayer transitions from a layered antiferromagnetic (↑↓ or ↓↑) state to the ferromagnetic-like states (↑↑ or ↓↓), where the left and right arrows denote the layer magnetization direction in the top and bottom layers, respectively. Oddly, there is a small, but non-zero RMCD signal in the

antiferromagnetic states despite the net out-of-plane magnetization summing to zero. One explanation could be that the fabrication procedures in making the bilayer CrI_3 transistor induce interfacial strain that is unequal between the two layers. This breaks inversion symmetry and leads to an equal but opposite non-zero RMCD signal between the two antiferromagnetic states. We will discuss inversion symmetry breaking later in Section 3.4.

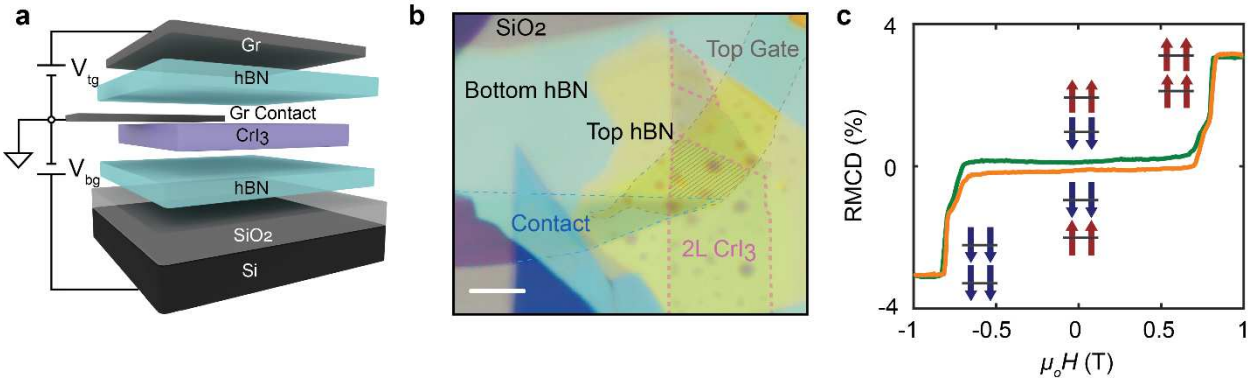

Figure 3.2. Device geometry for electrostatic gating of bilayer CrI_3 and preliminary magnetic characterization of bilayer CrI_3 device 1 (D1). (a) Schematic of a dual-gated bilayer CrI_3 device fabricated through van der Waals assembly. (b) False-color optical micrograph of D1. The scale bar is 5 μm. The two bilayer (2L) sections of the flake are outlined by a thick pink dashed line. (c) RMCD signal of D1 as a function of perpendicular magnetic field at zero gate voltage. Adapted from ref. [98].

On a second bilayer CrI_3 device, D2, which only has a single silicon back gate, we measure the MOKE signal of the bilayer as a function of magnetic field at V_g = -50 V, 0 V, and +50 V, plotted together in Fig. 3.3a. Upon applying a gate voltage of +50 V (red), a remarkable decrease in $\mu_o H_c$ from 0.6 T to ~0.5 T is observed. This is accompanied by a small decrease in the Kerr signal when the bilayer is spin-polarized in the ↑↑ state, explained by a decrease in the magnetic moment per unit cell that is also observed in monolayer CrI_3 flakes[107]. Likewise, opposite behavior is observed when the gate voltage is swept down to -50 V: $\mu_o H_c$ increases to ~0.7 T and the MOKE

signal in the ferromagnetic-like state increases by a few mrad. Since the interlayer exchange strength is directly proportional to $\mu_o H_c$, these measurements indeed show that electric fields can control the layered antiferromagnetic order of bilayer CrI_3.

Exploiting this strong dependence of $\mu_o H_c$ on the gate voltage, we demonstrate the direct electrical switching of magnetic states in bilayer CrI_3. This is done by applying a fixed bias magnetic field, $\mu_o H_{bias}$, near the zero-gate voltage $\mu_o H_c$ (~0.6 T) and sweeping the gate voltage continuously while measuring the Kerr signal as shown in Fig. 3.3b. At +50 V, the bilayer displays large Kerr signal, signifying that it is in the ↑↑ state and that $\mu_o H_c$ (~0.5 T) < $\mu_o H_{bias}$. As the gate voltage is ramped down toward -50 V, the bilayer switches from the ferromagnetic-like ↑↑ state to the antiferromagnetic ↑↓ state at around 0 V as $\mu_o H_c \geq \mu_o H_{bias}$. Repeating this same electrical switching protocol at slightly higher (lower) $\mu_o H_{bias}$, we find that the gate voltage required to switch between the antiferromagnetic and ferromagnetic-like states shifts towards more negative (positive) voltages. This is consistent with the fact that a higher $\mu_o H_{bias}$ requires larger negative gate voltages to tune $\mu_o H_c$ past $\mu_o H_{bias}$.

We map the rest of the V_g-H phase diagram on device D2 by taking a series of magnetic field-dependent MOKE measurements at fixed gate voltages from +50 V down to -50 V in steps of 5 V. The resulting color map of θ_K as a function of both magnetic field and gate voltage is shown in Fig. 3.3c. The MOKE signal traces as a function of magnetic field (gate voltage) in Fig. 3.3a (Fig. 3.3b), represent horizontal (vertical) line cuts in the V-H phase diagram denoted by matching colored arrows on the right-hand (top) side of the plot. The light colored region in the middle of the map illustrates low Kerr signal and signifies that the CrI_3 bilayer is in a layered antiferromagnetic state. The dark red (blue) region on the right (left) correspond to large, positive (negative) Kerr signal, reflecting the fact that the bilayer is in the ferromagnetic-like ↑↑ (↓↓) state.

The boundary between the colored regions demarcates magnetic phase transitions between the different magnetic states. Given the linearity of this boundary, we can deduce that the magnetoelectric effect is linear, at least within the range of gate voltages we applied. Converting the gate voltage into an electric field, E, by dividing by the thickness of SiO_2, we find that the $\mu_o H_c$ could be pushed to 0 T if E ~1.2 V/nm is applied, assuming that the magnetoelectric effect remains linear when E is large. While this is difficult to achieve with graphite/hBN gates, ionic liquid gating techniques could easily provide electric fields as strong as several V/nm.

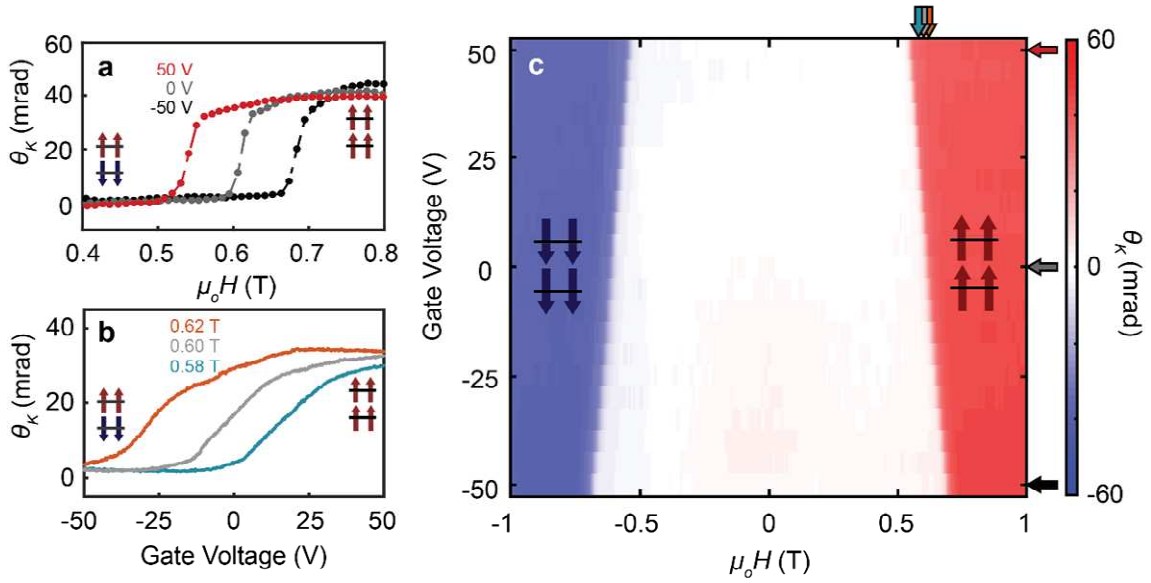

Figure 3.3. Electrical switching of magnetic states in bilayer CrI_3. (a) Kerr signal, θ_K, of bilayer CrI_3 device 2 (D2) as a function of magnetic field, $\mu_o H$, at V_g = -50 V (black), 0 V (grey), and 50 V (red) near the spin-flip transition at positive magnetic fields. (b) θ_K vs. gate voltage of D2 for select bias magnetic fields, $\mu_o H_{bias}$ = 0.58 T (blue), 0.60 T (grey), and 0.62 T (orange). Direct electrical switching from the layered antiferromagnetic state to the ferromagnetic-like state is observed. (c) Color plot of the MOKE intensity of D2 as a function of both gate voltage and applied magnetic field. The shift in the spin-flip transition, $\mu_o H_c$, for changes in magnetic field and gate voltage is clearly linear. Adapted from ref. [98].

3.3 DOPING-INDUCED CHANGES TO SPIN-FLIP TRANSITION

In the previous section, we found that an applied electric field can control the layered antiferromagnetism in bilayer CrI_3, specifically the spin-flip transition field between the antiferromagnetic and ferromagnetic-like states. However, since device D2 only has one SiO_2/Si gate, we cannot discern whether this electrical control originates from interlayer bias, D, or from electrostatic doping, Δn.

To explore these effects separately, we perform dual-gated RMCD measurements using device D1 to track the bilayer magnetic state while independently tuning D and Δn. The dual-gated bilayer CrI_3 device can essentially be modeled as a parallel-plate capacitor, where Δn is simply the charge accumulated from charging a capacitor and D is the net electric field applied from the two plates with the dielectric layer grounded:

$$\Delta n = C_{BG}(V_{BG} - V_{BG}^{D}) + C_{TG}(V_{TG} - V_{TG}^{D}),$$

$$D = C_{BG}(V_{BG} - V_{BG}^{D}) - C_{TG}(V_{TG} - V_{TG}^{D}).$$

In the above equations, C is the areal capacitance, V is the gate voltage, V^D is the charge neutral point voltage, and the indices TG and BG denote top gate and back gate respectively. Additionally, C is defined as ε/d, where ε and d are the relative permittivity constant and the thickness of the dielectric layer, respectively. Since we only care about the doping and D fields relative to the condition at zero applied gate voltage, we set all V^D terms to zero. Therefore, to vary the doping while keeping D fixed at zero, we set D to zero in the above equations and solve for V_{BG} in terms of V_{TG}. This results in a specific ratio of the gate voltages, V_{TG}/V_{BG}, that guarantees that Δn changes without affecting D. For device D1, this gate voltage ratio takes the form:

$$\frac{V_{TG}}{V_{BG}} = -\frac{d_{hBN}}{\frac{\varepsilon_{hBN}}{\varepsilon_{SiO_2}} d_{SiO_2} + d_{hBN}},$$

where ε_{hBN} and ε_{SiO2} is ~3 and ~3.9, respectively[108], and d_{hBN} and d_{SiO2} is 30 nm and 285 nm, respectively. Given these parameters, V_{TG}/V_{BG} ~ -1/8. Varying D while fixing the doping similarly gives a gate voltage ratio of equal magnitude to the ratio above, but of opposite sign (+1/8).

Figure 3.4 shows the RMCD intensity as a function of magnetic field near $\mu_o H_c$ ~ 0.85 T for constant D and set values of n (Fig. 3.4a), and constant n and set values of D (Fig. 3.4b). While a clear shift in $\mu_o H_c$ is observed when D is fixed and n changes, $\mu_o H_c$ does not change when n is fixed and D is allowed to vary. We also find that a doping level of ~3.5×10^{13} cm^{-2} or ~0.15 e^- per unit cell is required to tune $\mu_o H_c$ to zero. These observations confirm that doping, not interlayer bias, controls the layered antiferromagnetic order of bilayer CrI_3. This is not terribly surprising since doping plays a pivotal role in tuning the magnetism of other magnetic systems through changes in orbital occupation, exchange interactions, and magnetic anisotropy[102,109–112].

Yet, the microscopic picture of why doping leads to changes to the interlayer magnetic order in bilayer CrI_3 remains unclear. One possible explanation is that doping changes the orbital occupancies, affecting the interlayer super-superexchange by strengthening ferromagnetic pathways, weakening antiferromagnetic pathways, or both.

We now map the rest of the D-n phase space by performing top gate RMCD sweeps for a series of fixed bottom gate voltages ranging from -15 V up to 15 V. For these measurements, the bias magnetic field was parked close to ~ 0.78 T, the zero-gate value of $\mu_o H_c$. A color map of the RMCD intensity as a function of both the top and bottom gate voltages is illustrated in Figure 3.4c. The light (dark) pink region shows low (high) RMCD signal and represents the antiferromagnetic ↑↓ (ferromagnetic-like ↑↑) state. A linear boundary is observed that demarcates the transition between the antiferromagnetic and ferromagnetic-like states, which as expected, precisely spans the gate ratios required to maintain constant doping, plotted as a gray dotted line in the phase map.

In other words, magnetic switching cannot occur between the antiferromagnetic and ferromagnetic-like phases if traversing parallel to the gray dotted line, since doing so equates to continuously varying *D* while fixing *n*.

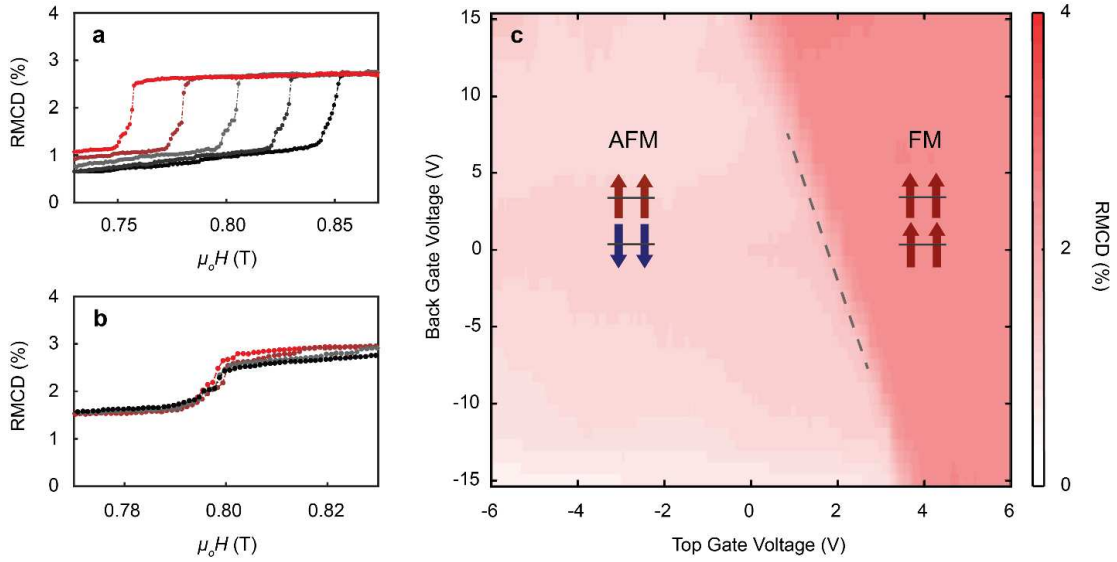

Figure 3.4. Origin of voltage-controlled switching of magnetic states in bilayer CrI_3 device 1. (a) RMCD signal of bilayer CrI_3 device 1 (D1) as a function of applied magnetic field at fixed doping levels from 0 cm^{-2} (black) to 4.4 x 10^{-12} cm^{-2} (red) for zero displacement field. (b) RMCD signal as a function of applied magnetic field at several displacement fields ranging from 0 V/nm (red) to 0.6 V/nm (black) for zero doping. The metamagnetic transition is clearly insensitive to changes in the displacement field but strongly dependent on the doping level. (c) Color map of RMCD signal when sweeping both the graphite top gate and silicon back gate. The pink region reflects negligible RMCD signal, corresponding to the layered antiferromagnetic states. The red region corresponds to the ferromagnetic ↑↑ state. The boundary between them is parallel to a constant doping contour (grey dashed line). Reproduced from ref. [98].

3.4 IDENTIFYING ANTIFERROMAGNETIC STATES THROUGH SYMMETRY BREAKING

In this section, we shift our attention to the electrical control of *antiferromagnetic* order at zero magnetic field. We first revisit the magnetic field sweep of the RMCD signal from an ungated bilayer CrI_3 device (Fig. 3.2c). Despite being in one of two antiferromagnetic states *i.e.* a magnetic

state with net zero out-of-plane magnetization, the bilayer exhibits non-zero RMCD signal at 0 T. Furthermore, the sign of this signal depends on whether the magnetic field was swept down from the ↑↑ or the ↓↓ state.

We can reason that the two states with equal and opposite RMCD signals must be the two different antiferromagnetic states through the following logic. Although there is no net out-of-plane magnetization in the antiferromagnetic state, the presence of spin order breaks time-reversal symmetry. It is also clear that a ferromagnet with an out-of-plane magnetization, M_z, in an applied magnetic field, H, possesses time-reversal pairs of magnetic states. That is, for any $M_z(H)$, the following relation is true: $M_z(H) = -M_z(-H)$. To extend this argument to the bilayer, we treat it as two weakly antiferromagnetically coupled ferromagnets. In the ferromagnetic-like states, M_z is equal and opposite in both layers for any given H. Upon sweeping H past the spin-flip transition into the antiferromagnetic states, the layer magnetizations must be equal, but opposite depending on which ferromagnetic-like state the bilayer was initialized in. As such, the antiferromagnetic state that is initialized from starting in the ↑↑ state must be different from the antiferromagnetic state that is prepared from the ↓↓ state. This provides a reliable protocol by which to controllably initialize and access the different antiferromagnetic states.

We now apply a gate voltage to investigate its effects on the two antiferromagnetic states. One antiferromagnetic state is prepared by starting in the ↑↑ state with an applied magnetic field of 1 T, and then sweeping the field back to zero (Initialization 1, inset Fig. 3.5a). Remaining at zero external magnetic field, we sweep the back gate voltage and observe a MOKE signal that is linearly dependent on the voltage with a slope of -0.04 mrad/V, shown in Fig. 3.5a. The other antiferromagnetic state is prepared by starting in the ↓↓ state with a magnetic field of -1 T and sweeping the field back to zero (Initialization 2, inset Fig. 3.5b). In Fig. 3.5b, the MOKE signal

also exhibits a linear dependence on the gate voltage, but with an opposite slope of +0.04 mrad/V. These results further show that the two initialization processes indeed lead to two distinct layered antiferromagnetic states, ↑↓ and ↓↑, which are time-reversed pairs. More importantly, however, we have electrical tunability over the antiferromagnetic states even at zero magnetic field.

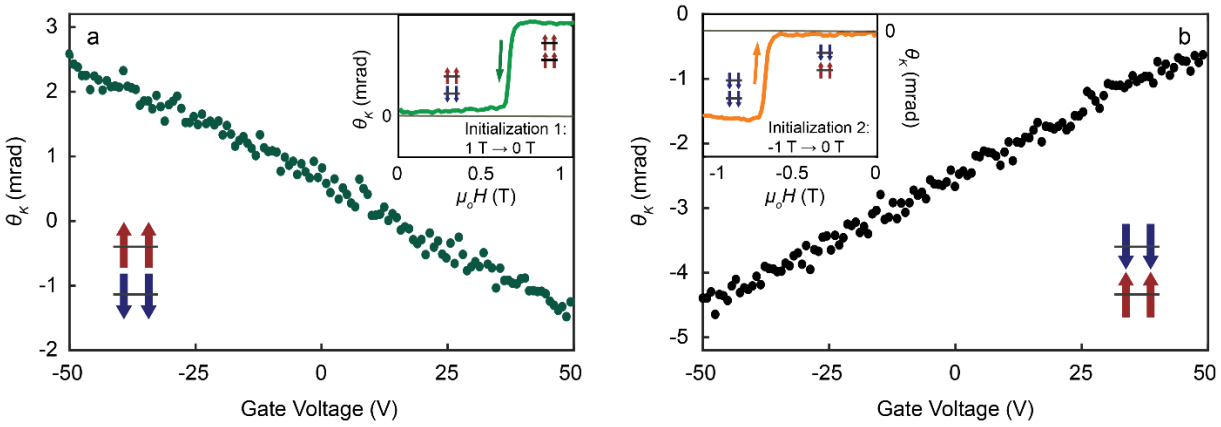

Figure 3.5. Gate voltage-induced MOKE of layered antiferromagnetic states at zero magnetic field. Gate-dependent MOKE signal of a non-encapsulated bilayer CrI_3 device (Device 2) prepared in the ↑↓ state following the initialization depicted in the inset (see text for details). **(b)** Equivalent measurement performed on the device prepared in the ↓↑ state by the initialization process in the inset. The opposite slopes of the MOKE signal between ↑↓ and ↓↑ highlight the symmetry breaking-induced MOKE in a collinear antiferromagnet through an applied interlayer bias. Insets show the initialization processes for preparing antiferromagnetic states at zero field (discussed in the text). Reproduced from ref. [98].

This observed magnetoelectric coupling in the layered antiferromagnetic states is a result of broken time-reversal and inversion symmetry due to the applied gate voltage[113]. The magneto-optical Kerr effect (and by extension, the Faraday effect) arises from antisymmetric components in the conductivity tensor, σ[53]. These components are precisely the parts of the conductivity tensor which give rise to the DC Hall effect in electrical transport, and so MOKE and RMCD can be viewed as a high-frequency (10^{14} Hz) AC Hall effect. Moreover, one can also define an associated

vector, $\boldsymbol{n}$, for the MOKE signal which depends on a transverse electric field, $\boldsymbol{E}$, traveling perpendicular to an applied electric field, $\boldsymbol{E}$, in the following way:

$$\boldsymbol{n} = \boldsymbol{j} \times \boldsymbol{E}.$$

If time-reversal symmetry is present, then $\boldsymbol{n} = \boldsymbol{j} \times \boldsymbol{E} = -\boldsymbol{j} \times \boldsymbol{E} = \boldsymbol{0}$. This is simply a re-statement that the MOKE signal for a paramagnet is zero. Time-reversal symmetry is, of course, not present in ferromagnets and antiferromagnets, so $\boldsymbol{n}$ is allowed to be non-zero since $\boldsymbol{j} \times \boldsymbol{E}$ no longer needs to be equivalent to $-\boldsymbol{j} \times \boldsymbol{E}$. In the antiferromagnetic state of a pristine CrI_3 bilayer, however, the combined time-reversal and inversion symmetry is present. Since $\boldsymbol{j}$ is unaffected by this operation and $\boldsymbol{E}$ flips sign, $\boldsymbol{n}$ is once again constrained to be zero: $\boldsymbol{n} = \boldsymbol{j} \times \boldsymbol{E} = \boldsymbol{j} \times -\boldsymbol{E} = \boldsymbol{0}$. Applying an out-of-plane electric field breaks the inversion symmetry of the bilayer, allowing $\boldsymbol{n}$ to be non-zero. This also implies that since the two antiferromagnetic states are linked via an inversion operation, $\boldsymbol{n}$ (the MOKE/RMCD signal) must be equal and opposite between the two states, fully describing the magnetoelectric effect observed for the antiferromagnetic states of bilayer CrI_3.

We can also intuitively explain this linear magnetoelectric effect through the spin-layer locking effect. For an antiferromagnetic state at zero field, the spin (magnetization) orientation is locked to the layer pseudospin that labels the geometric top and bottom layers. A direct consequence of this spin-layer locking effect is that the creation of a layer polarization is accompanied by a net magnetization[114,115]. In the antiferromagnetic configuration, the opposite spin orientations of the two layers quench the interlayer hopping and hence the layer hybridization[114,116]. The application of an electrostatic gate voltage then creates a layer polarization of the carriers, resulting in net magnetizations of opposite signs in the $\uparrow\downarrow$ and $\downarrow\uparrow$ states. The layer

polarization and hence net magnetization has a linear dependence on the gate voltage, consistent with the observed gate dependence of the MOKE signal in Fig. 3.5. Tunability of the net magnetization with gate voltage gradually weakens as the temperature increases (Fig. 3.6), until at T_N ~ 40 K, the gate voltage has no effect on the MOKE signal. These temperature-dependent measurements show that the bilayer Néel temperature is unaffected within the applied gate voltage range.

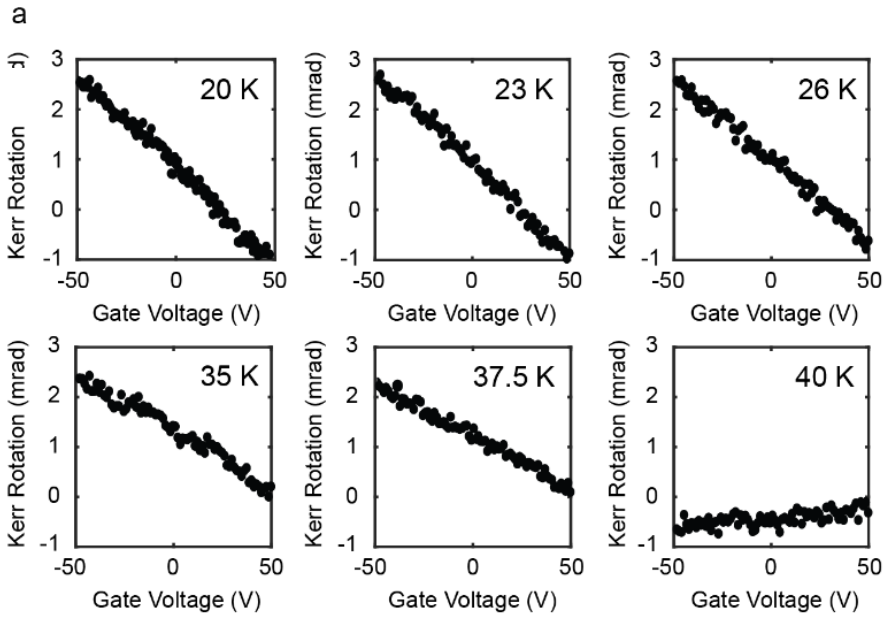

Figure 3.6. Gate-dependent MOKE at increased fixed temperatures with no applied magnetic field. MOKE signal of the bilayer (Device 2) prepared in the ↑↓ state with no applied magnetic field at several fixed temperatures ranging from 20 K to 40 K. As the device is warmed, the linear dependence of the MOKE signal on gate voltage decreases, showing that the tunability of the net magnetization weakens and is inversely related to the temperature. Above the Néel temperature at ~40 K, there is no dependence of the MOKE signal on the gate voltage, signaling that the layered antiferromagnetic order and hence the spin-layer locking effect is destroyed. In addition, the disappearance of the MOKE signal for all gate voltages at 40 K implies that the Néel temperature is the same regardless of the applied gate voltage. Therefore, the electric field effect does not affect the Néel temperature of bilayer CrI_3. Reproduced from ref. [98].

Furthermore, this allows us to identify and controllably access the two energetically degenerate antiferromagnetic states. The application of a positive gate voltage results in a larger electron density in the bottom layer than in the top layer (Fig. 3.7a). If the bilayer is in the ↑↓ state, the net magnetization then points down with a negative slope of the MOKE signal as a function of gate voltage (Fig. 3.5a and Fig. 3.7b). The ↓↑ state will then have a positive slope in the gate-dependent MOKE signal (Fig. 3.5b and Fig. 3.7c). Although the device assembly process may already break the degeneracy between the ↑↓ and ↓↑ states, the signs of the gate-dependent MOKE slopes are nevertheless fingerprints for distinguishing between the two antiferromagnetic states. Based on Figs. 3.5a&b, we can definitively determine that by using Initialization 1, the ↑↑ state transitions to the ↑↓ state, and by using Initialization 2, the ↓↓ state transitions to the ↓↑ state.

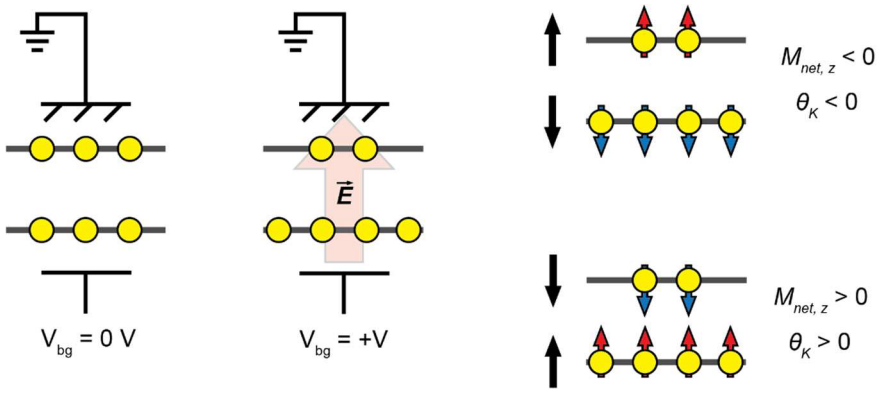

Figure 3.7. Intuition of the non-zero MOKE signal in the antiferromagnetic states of bilayer CrI_3. When the gate voltage is zero, the carrier density is the same for both layers (left). Upon an application of a gate voltage, hopping processes between the layers lead to a charge imbalance between the two layers and an electric dipole is formed (center). Because of the strong intralayer ferromagnetic interactions which are opposite between the two layers, the electric dipole also creates a magnetic dipole which is equal and opposite between the two antiferromagnetic states

(right). The linearity of the effect comes from the fact that the change in the electric dipole is linear with respect to the gate voltage.

3.5 SUMMARY, PARALLEL WORK AND FUTURE DIRECTIONS

In this chapter, we demonstrated the electrical control of magnetism of bilayer CrI_3. Overall, there are two main effects that electric fields have on the magnetic order of bilayer CrI_3:

- Electrostatic doping induces changes to the interlayer antiferromagnetic order. Electron-doping causes the antiferromagnetic exchange to weaken, while hole-doping leads to stronger interlayer exchange interactions. This effect is linear as a function of doping and could potentially lead to a transition from layered antiferromagnetism to ferromagnetism with strong enough electric fields.
- Interlayer bias from displacements fields leads to a linear magnetoelectric effect that gives rise to non-zero Kerr signal in the layered antiferromagnetic states, even when the net magnetization is zero. This effect hinges on breaking the combined time-reversal and inversion symmetry and can be intuitively be viewed as inducing a magnetic polarization through electric polarization. There were also signatures of decreased Kerr signal in the ferromagnetic-like phase (Fig. 3.6b) which correspond precisely to the changes in Kerr signal in monolayer CrI_3 due to electric fields[107].

Our findings were confirmed through parallel work at Cornell[104,107], who were able to tune the spin-flip transition to ~0.2 T through stronger applied electric fields. Additional work on the gate control of magnetism in four-layer CrI_3 has also been demonstrated[117]. When a magnetic field is applied that is just below magnetic saturation, the intermediate magnetic states of four-layer CrI_3 can be switched via a gate voltage from a low-energy configuration, $\uparrow\uparrow\downarrow\uparrow$, to a higher-energy configuration $\uparrow\uparrow\uparrow\downarrow$. While MOKE microscopy cannot discern between these two magnetic states,

electron tunneling measurements can due to the differences in the number of antiferromagnetic tunneling barriers.

There are still gaps in the theoretical understanding of this electrically tunable magnetism. The doping effect is still not well-explained and a microscopic model that involves the orbitals in super-exchange and super-superexchange has not been proposed. It is also unknown what role electrostatic doping has on the linear magnetoelectric effect in the antiferromagnetic states, *i.e.* whether interlayer bias alone explains the observed effects[118]. Although the spin-layer locking effect provides a convenient and intuitive grasp of the linear magnetoelectric effect in the antiferromagnetic states, this description is incomplete as CrI_3 is an electrical insulator. This implies that charge hopping between layers should be largely suppressed due to the negligibly small density of states within the band gap. While symmetry provides an overview of why a MOKE signal should be present when biasing the antiferromagnetic states of bilayer CrI_3, a microscopic model of what leads to this magnetoelectrical effect is not well-understood.

Beyond CrI_3, demonstrations of electric-field control of magnetism have also been shown in other vdW materials. In $CrGeTe_3$, for instance, electric fields can tune the magnetic anisotropy in five-layer flakes evidenced by the change in remanence of its magnetic hysteresis. With ionic liquid gating, $CrGeTe_3$ can demonstrate ambipolar field-effect transistor behavior and could be a launching point to explore spin-transistor devices in magnetic vdW materials. In trilayer flakes of Fe_3GeTe_2, ionic liquid gating is able to tune the T_C from cryogenic temperatures (~100 K) up to room temperature[119]. It is questionable, though, whether the electric field control is actually intrinsic or not; other studies showed that intercalation of Na^+ ions in bulk Fe_3GeTe_2 can lead to the formation of Fe_2Ge defects that exhibit room-temperature ferromagnetism[120].

Promising directions have been unlocked with the ability to electrically tune magnetism in vdW materials. In particular, magnetic heterostructures which rely on exchange bias[121] can be easily tuned by electric fields to realize electrical switching of magnetic states for low-power computing and memory storage applications. Local gating at the nanoscale[122] using a scanning probe tip could be used to induce magnetic textures, leading to the exploration of topological skyrmions in the 2D limit. In layered antiferromagnetic topological insulators, an applied electric field could bring about the quantum anomalous Hall insulating state via an electrically induced magnetic-phase transition to the ferromagnetic state.

Chapter 4. TUNING INELASTIC SCATTERING VIA SYMMETRY CONTROL IN 2D MAGNET CrI_3

In the first few chapters, we discussed the magnetic properties of atomically thin CrI_3. We found that unlike the ferromagnetism found in the bulk crystal form, few-layer CrI_3 exhibits layered antiferromagnetism. Electric fields and pressure can be used to control the antiferromagnetic order in bilayer CrI_3[64,65,98,104,107]. demonstrating a new platform by which to realize novel spintronics devices utilizing magnetic vdW materials and their heterostructures[38,70–72]. Beyond device applications, we also found in Section 3.4 that symmetry plays a heightened role in the 2D limit, enabling the generation of *non*-zero MOKE signal through electric fields in an atomically thin bilayer antiferromagnet. Subsequent work has led to the discovery of other exciting symmetry-related magneto-optical phenomena, including spontaneous helical photoluminescence from monolayer ferromagnetic insulators[123,124] and giant second harmonic generation in the antiferromagnetic state of bilayer CrI_3[63].

We pursue this direction further by exploring symmetry-related magneto-optical effects governed by quasiparticle excitations in CrI_3. In this chapter, we focus on phenomena pertaining to quantized atomic vibrations, or *phonons*. We start by briefly discussing what a phonon is and how we can deduce the phonon modes in monolayer CrI_3 through group theory. We then highlight the main evidence for spin-phonon coupling in atomically thin CrI_3: unprecedented giant polarization rotation of light scattered by an A_{1g} phonon[57]. Lastly, we will demonstrate the symmetry control of Raman selection rules through magnetoelectric switching in bilayer CrI_3. This chapter closely follows my work in *B. Huang et al.* "Tuning inelastic scattering via symmetry control in the two-dimensional magnet CrI_3" which was published into *Nature Nanotechnology* in 2020.

4.1 PHONON MODES OF CrI_3

In solids, atoms can be displaced from their equilibrium positions due to thermal excitations or through external fields. This results in the collective vibration of the constituent atoms in the solid. Furthermore, these vibrations can be quantized, with its quasiparticle representation being the phonon. In general, phonons interact weakly with other particles in solids and so its eigenstates *i.e.* the vibrational modes, can be solved for by treating their interactions as a perturbation to the equilibrium state[125]. Consequently, their eigenstates obey the same symmetries as the Hamiltonian which represents the interactions in the material. This is important in crystals since the point group of the crystal lattice dictates the possible symmetries of the phonon modes[126]. Therefore, the number of phonon modes of a crystal and their associated symmetries can be analyzed using the machinery of group theory[127].

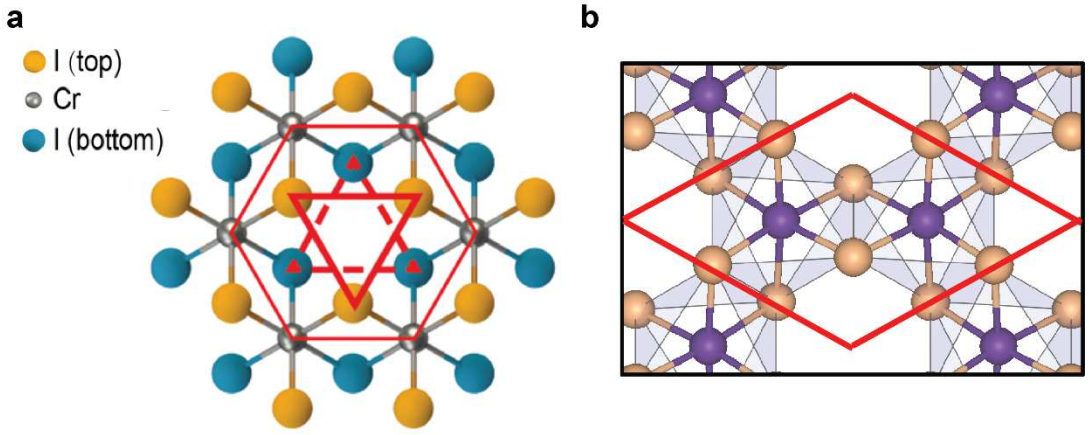

Figure 4.1. Monolayer CrI_3 lattice and unit cell. (a) Illustration of the crystal lattice of monolayer CrI_3, emphasizing the Cr^{3+} (gray) honeycomb lattice (hexagon outlined in red) and the relative positions of the top and bottom I^- ions (yellow and blue, respectively). (b) Unit cell of monolayer CrI_3. Clearly, there are two Cr^{3+} ions (purple) and six I^- ions (gold). Adapted from refs. [63] and [123].

We will perform exactly this analysis to find the phonon modes of CrI_3. First, we need to find the reducible representations of the translation vector, Γ_{vec}. The crystal lattice of monolayer

CrI_3 is shown in Figure 4.1a and its unit cell in Figure 4.1b. Monolayer CrI_3 belongs to the D_{3d} point group (character table in Table 4.1).

Table 4.1 – Character table for the D_{3d} point group.

D_{3d}	E	$2C_3$	$3C_2$'	i	$2S_6$	$3\sigma_d$	Linear functions	Quadratic functions
A_{1g}	+1	+1	+1	+1	+1	+1		x^2+y^2, z^2
A_{2g}	+1	+1	-1	+1	+1	-1	R_z	
E_g	+1	-1	0	+2	-1	0	(R_x, R_y)	(x^2-y^2, xy), (xz, yz)
A_{1u}	+1	+1	+1	-1	-1	-1		
A_{2u}	+1	+1	-1	-1	-1	+1	z	
E_u	+1	-1	0	-2	+1	0	(x, y)	

From the table, we find that the reducible representation for Γ_{vec} is:

$$\Gamma_{vec} = A_{2u} + E_u.$$

Next, we need to determine the reducible representation, Γ_{atom}, that contains the number of atoms per unit cell which are fixed under the set of group operations in D_{3d}. For example, since there are eight atoms in the unit cell, the identity operator of Γ_{atom} has the character, 8. We find that Γ_{atom} for monolayer CrI_3 has the following representation:

	E	$2C_3$	$3C_2$'	i	$2S_6$	$3\sigma_d$
Γ_{atom}	+8	+2	+2	0	0	+2

Finally, the reducible representation for all the phonon modes, Γ_{3N}, can be determined by taking the outer product of Γ_{vec} and Γ_{atom}:

	E	$2C_3$	$3C_2$'	i	$2S_6$	$3\sigma_d$
Γ_{vec}	+3	0	-1	-3	0	+1
Γ_{atom}	+8	+2	+2	0	0	+2
Γ_{3N}	+24	0	-2	0	0	+2

As we will be studying the optical phonons through Raman spectroscopy (explained in Section 4.2), we remove the acoustic phonon modes by subtracting Γ_{vec} from Γ_{3N}. Then, in terms of the irreducible representations of the D_{3d} group, we arrive at the following representation for the optical phonon modes of CrI_3:

$$\Gamma_{3N} - \Gamma_{vec} = 2A_{1g} + 2A_{2g} + 4E_g + A_{1u} + 2A_{2u} + 3E_u.$$

In other words, there are a total of 14 optical phonon modes in CrI_3: two A_{1g} modes, two A_{2g} modes, four E_g modes, one A_{1u} mode, two A_{2u} modes, and three E_u modes. Although group theory allows us to determine the number of phonon modes in a material, the energies and the actual atomic motions of each mode must be calculated through either lattice dynamical simulations or density functional theory[125]. These calculations have been done previously for CrI_3 and can be found in refs. [128] and [129].

4.2 Principles of Raman spectroscopy

The most prevalent method to detect phonons in materials is through Raman spectroscopy. Light which scatters off a material predominantly undergoes Rayleigh scattering, an elastic scattering process that conserves momentum and energy. As shown in Figure 4.2a, one can illustrate this process in the following way: an electron in the ground state absorbs an incident photon and is excited to a virtual state; then the electron relaxes back to the same ground state by emitting a photon of equal energy as the incident photon.

On rare occasions, a small fraction of these scattering events (roughly 1 in 10^7) end up *inelastically* scattering through a process known as Raman scattering[130], as illustrated in Figure 4.2b&c. In Stokes Raman scattering (Fig. 4.2b), an electron starts in the ground state and is excited to a virtual state via the absorption of a photon with energy E. Upon relaxing, however, the electron

emits a photon that is lower in energy by a phonon quanta, $E - E_{vib}$, and ends up in a vibrational excited state. In anti-Stokes Raman scattering (Fig. 4.2c), the electron starts in the vibrational excited state, is excited to the virtual state by a photon of energy, E, and relaxes back to the ground state by emitting a photon with energy, $E + E_{vib}$. An equivalent interpretation is that Stokes (anti-Stokes) Raman scattering generates (removes) a phonon of energy, E_{vib}, from the lattice.

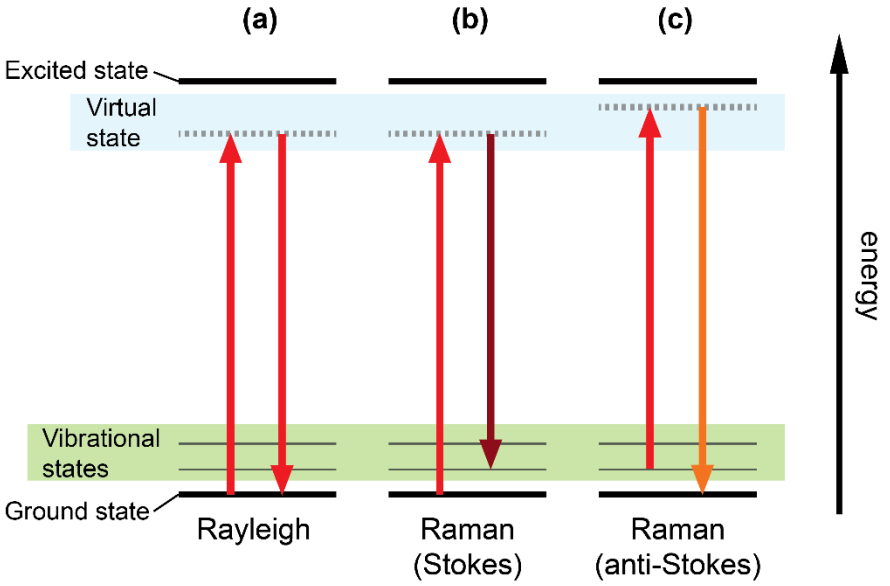

Figure 4.2. Energy diagrams of Rayleigh and Raman scattering. (a) Rayleigh scattering: absorption of a photon with energy E excites an electron from the ground state up to the virtual state (left, red arrow pointing up). The electron in the excited state relaxes to the ground state by emitting a photon of the same energy as the incident photon which excited it. (b) Stokes Raman scattering: excitation process identical to Rayleigh scattering in (a). However, the electron relaxes to a vibrational state that sits at a small energy, E_{vib}, above the ground state and emits a photon of energy, $E - E_{vib}$. A phonon is created in this process. (c) Anti-Stokes Raman scattering: an electron in a vibrational state is excited to a virtual state via absorption of a photon with energy E. The electron then relaxes back to the ground state by emitting a photon of energy $E + E_{vib}$. This scattering process annihilates a phonon.

The ratio of scattering events between the Stokes and anti-Stokes processes depends on the thermally excited phonon population which because it is bosonic, scales as $\exp\left(\frac{-E_{vib}}{k_B T}\right)$, where E_{vib}

is the phonon energy. Therefore, while it is possible to observe anti-Stokes scattering events from high-energy quasiparticles (~50 meV) at room temperature, it is virtually impossible to detect them at cryogenic temperatures (~15 K or $k_B T$ = 1.18 meV). Tracking the ratio of Stokes to anti-Stokes scattering is also a useful measure of the sample temperature to track unintentional Joule or laser heating of the sample.

From a classical perspective, Raman scattering can be viewed as coming from changes in the polarizability tensor of a material, $\boldsymbol{\alpha}$[126]. This is important because the selection rules for Raman scattering depends on whether their symmetry of the phonon mode conforms to how $\boldsymbol{\alpha}$ transforms. Since $\boldsymbol{\alpha}$ is a rank two tensor that transform according to a quadratic basis function, any phonon mode with symmetry that also transforms in any of the quadratic functions will be Raman active. For monolayer CrI_3, the only symmetries which transform quadratically are the A_{1g} and E_g symmetries. Therefore, we expect to see from a Raman scattering experiment on monolayer CrI_3, two A_{1g} and four E_g phonon modes.

The expected polarization dependence of the Raman scattering is also dependent on the symmetry of the phonon mode. That is because the polarizability tensor encodes the symmetry information of a given phonon mode, dictating how an electron oscillates and re-emits light in response to the incident optical field. In practice, for incident light with polarization, $|i\rangle$, and scattered light with polarization, $|f\rangle$, the Raman scattering intensity, I, is equal to $|\langle f|R|i\rangle|^2$, where R is a symmetry-specific Raman tensor. For instance, for the A_{1g} mode in monolayer CrI_3, the Raman tensor has the form:

$$R_{A_{1g}} = \begin{bmatrix} a & 0 & 0 \\ 0 & a & 0 \\ 0 & 0 & b \end{bmatrix}.$$

where a and b are real coefficients. If the incident light is horizontally polarized, $|i\rangle = \begin{bmatrix}1\\0\\0\end{bmatrix}$, and we vary the analyzing polarizing angle, $|f\rangle = \begin{bmatrix}\cos\theta\\\sin\theta\\0\end{bmatrix}$, then the expected polarization dependence of scattered light is:

$$\left|\left\langle f\left|R_{A_{1g}}\right|i\right\rangle\right|^2 = a^2 cos^2\theta$$

where θ is the relative angle between the transmission axis of the polarizer and horizontally polarized light. We see then that maximal Raman scattering coincides when $\theta = 0$ or π, signifying that the scattered light from an A_{1g} phonon mode is co-linear with the incident photon polarization.

The same analysis can be performed for an E_g phonon mode. Since the E_g phonon mode is twofold degenerate, it has two Raman tensors:

$$R_{E_{g,1}} = \begin{bmatrix}c & 0 & 0\\0 & -c & d\\0 & d & 0\end{bmatrix};\ R_{E_{g,2}} = \begin{bmatrix}c & 0 & 0\\0 & -c & d\\0 & d & 0\end{bmatrix}.$$

This results in an I that is independent of the analyzing polarizer angle.

To perform the polarization-dependent magneto-optical Raman measurements, we designed and constructed a home-built confocal Raman microscope that is illustrated in Figure 4.3. Because samples are excited in the backscattering geometry and the momentum of the photon, $p = \frac{h}{\lambda}$ (h is Planck's constant and λ is the wavelength of the photon), is much less than the crystal momentum (three orders of magnitude less), this implies that only zero-momentum phonons can be probed. There are several key elements that enabled the success in sensitively detecting Raman scatter from these 2D flakes: the laser used (HeNe, 1.96 eV) had an excitation energy that is close to an electronic transition in CrI_3; and the use of Bragg filters to clean the laser line and reject Rayleigh scattered light down to 3 cm^{-1} (0.6 meV) from the laser line. The benefit of exciting on

resonance with, in this case a ligand-to-metal charge transfer transition, is that Raman scattering intensities can be enhanced by a factor of up to 10^6, as can be seen in the difference in Raman signal from CrI_3 between 1.96 eV and 2.33 eV (Figure 4.4)[131]. Conventional laser notch filters from ThorLabs, while effective at eliminating Rayleigh scatter, have bandwidths of up to 300 cm^{-1}. Obviously, using a Bragg filter that can cut the Rayleigh scatter down to 3 cm^{-1} without also filtering out the Raman signal is imperative for any successful detection of the phonon (and magnon, Chapter 5!) modes in any system.

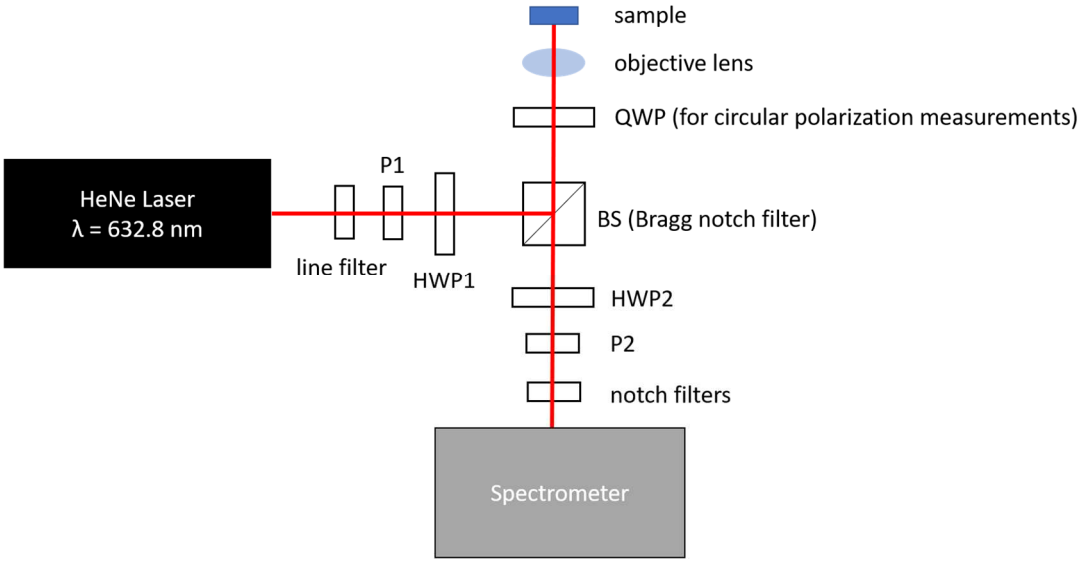

Figure 4.3. Diagram of confocal Raman microscope. Our home-built Raman microscope uses a HeNe laser (λ = 632.8 nm, black box) as the excitation source. The laser (path outlined by red line) is spectrally cleaned by a BragGrate™ bandpass 633 nm line filter down to 5 cm^{-1} from the laser line. A BragGrate™ notch filter acts as a beam splitter which further cleans the excitation source and sends the excitation path toward the sample. The laser is focused down to a 1-μm beam spot on the sample using an objective lens. Rayleigh scattering in the backscattered light is then cleaned by the beam splitter BragGrate™ notch filter as well as two others downstream toward the spectrometer (gray box). The polarization of light in our excitation and collection paths is set by polarizers, P1 and P2, half-wave plates, HWP1 and HWP2, as well as the quarter-wave plate, QWP.

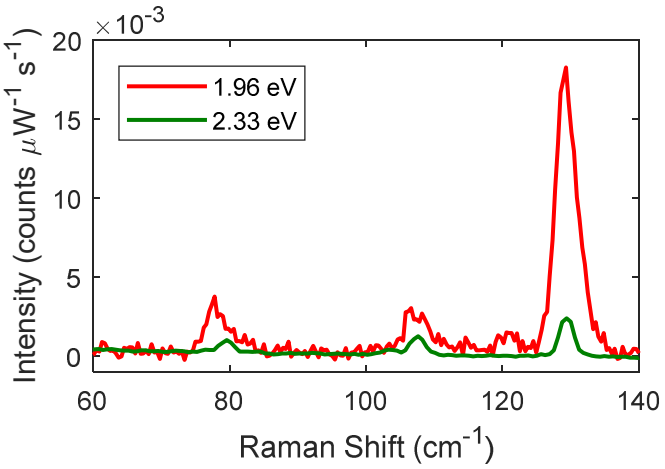

Figure 4.4. Resonant vs. non-resonant Raman scattering of exfoliated CrI_3 flakes. Raman spectra of a bulk CrI_3 flake taken with two excitation sources: one with a HeNe laser at 632.8 nm (red trace, 1.96 eV) and one with a solid-state laser at 532 nm (green trace, 2.33 eV). The spectra are normalized by the laser power used and the spectra integration time. Altogether, there is a roughly an order of magnitude improvement in the Raman signal of CrI_3 when using 633 nm excitation as compared to exciting with 532 nm.

4.3 Magneto-optical Raman effect in monolayer CrI_3

To begin, we first check the consistency of our group theory analysis in Section 4.2 by performing Raman scattering measurements on a monolayer flake of CrI_3 (optical image in top inset of Fig. 4.5a) above T_C in the paramagnetic phase. For these measurements, we use a laser power of 80 μW and integrate for 5 minutes. The sample temperature is ~60 K, above the monolayer T_C of 45 K. Paramagnetism is confirmed by magnetic field-dependent measurements of the RMCD signal which show a linear trace with no magnetic hysteresis (Fig. 4.5a inset). As shown in Figure 4.5a, the two Raman spectra, XX (black) and XY (red), show four distinct peaks. Here, XX and XY denote the excitation polarization and analyzing polarizer being co-polarized and cross-polarized, respectively. Given the weak signal in the XY channel, and energies relative to theory[128], we assign the peaks at 76.9 cm^{-1} and 127.4 cm^{-1} to be Raman scattering from the two predicted A_{1g} phonons.

The nearly equal intensities between XX and XY peaks at 107.7 cm^{-1} and 114.8 cm^{-1} meanwhile confirm that these two peaks are Raman scattering from two of the four predicted E_g phonon modes. Oddly, the predicted E_g phonon modes at 50 cm^{-1} and 230 cm^{-1} are not observed in the Raman spectra. One possibility is that scattering cross-section of these phonon modes is too small and therefore lead to very weak Raman scattering that is difficult to detect. We also find that the A_{1g} phonon mode at 127.4 cm^{-1} has significant Raman scattering in the XY channel, roughly 25% of the scattering intensity in the XX channel. Such Raman activity is typically forbidden from A_{1g} phonons, but resonant effects can lift this restriction and weakly allow Raman scattering in the XY channel through imaginary components in the Raman tensor[131].

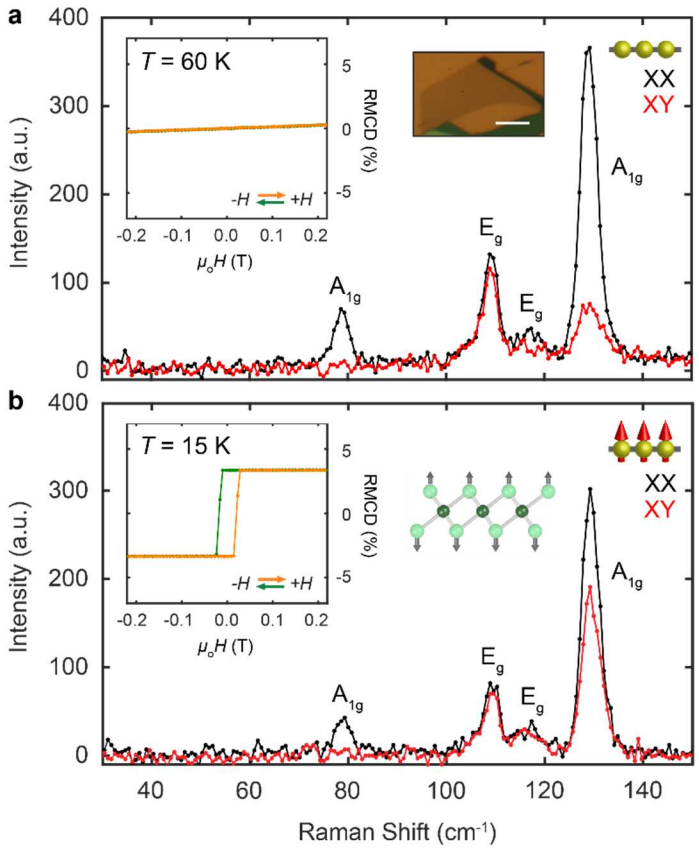

Figure 4.5. Raman scattering and its dependence on magnetic order in monolayer CrI_3. (a-b), Raman spectrum of monolayer CrI_3 with zero applied magnetic field in the (a) paramagnetic state at 60 K and (b) ferromagnetic state at 15 K. Black (red) curves correspond to co-linear (cross-

linear) excitation and detection. Insets on the left show the RMCD signal as a function of magnetic field. Right inset of (a) is an optical image of an exfoliated CrI_3 monolayer. Right inset of (b) shows the vibrational mode corresponding to the A_{1g} mode at 127.4 cm^{-1}. Scale bar is 5 µm. Reproduced from ref. [57].

Verifying that our group theory analysis of the monolayer phonon modes above T_C is indeed correct, we now cool the CrI_3 monolayer below T_C to 15 K. At this temperature, the monolayer is clearly ferromagnetic as evidenced by magnetic hysteresis in the magnetic field-dependent RMCD signal as seen in the inset of Fig. 4.5b. While the Raman spectra shows relatively little change in both scattering channels for the 76.9 cm^{-1} A_{1g} mode and the two E_g modes at low temperature, the A_{1g} mode at 127.4 cm^{-1} exhibits enhanced Raman scattering in the XY channel. This enhancement is also seen when the monolayer is in the opposite spin configuration, as seen in Fig. 4.6. Given that magnetic effects are present in only the 127.4 cm^{-1} A_{1g} phonon mode (vibrational mode depicted in the inset of Fig. 4.5b), we narrow our experimental efforts on the Raman scattering from this mode for the rest of this chapter.

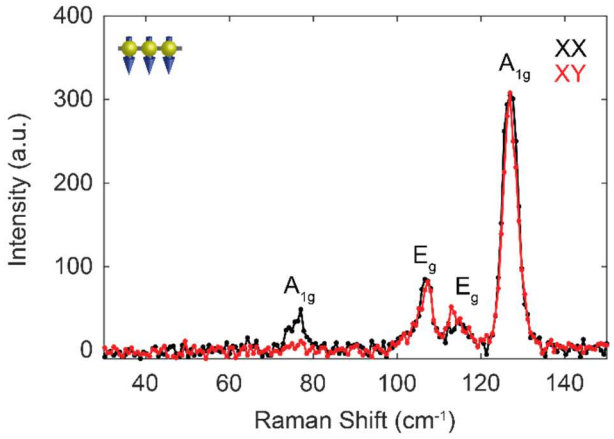

Figure 4.6. Polarization-resolved Raman scattering of monolayer CrI_3 in the spin-down ferromagnetic state. Co- (black) and cross-linearly (red) polarized Raman spectra of a CrI_3 monolayer in the spin-down ferromagnetic state taken at 15 K with no applied magnetic field. Reproduced from ref. [57].

Since there is a sudden enhancement in the XY channel of the 127.4 cm^{-1} peak, we need to discern whether this signal originates from Raman scattering of the A_{1g} phonon mode, or an entirely new feature such as a high-energy magnon[132]. To separate the two, we monitor the Raman scattering intensity as a function of the analyzing polarization while keeping the excitation polarization fixed to the horizontal axis (represented by a green double-sided arrow along 0° in Fig. 4.7a&b). Above T_C at 60 K, the polarization pattern has two lobes, with the polarization axis (dotted line) coinciding with the excitation polarization. This is expected for the Raman scattering from an A_{1g} mode since the intensity is proportional to $cos^2\theta$ as we deduced above.

Cooling below T_C to 15 K, the polarization pattern of the 127.4 cm^{-1} A_{1g} mode in the ferromagnetic phase still features two lobes. However, there is a noticeable rotation of the polarization axis, φ, away from the co-linear condition that is equal, roughly 40°, but opposite in sign between the two different magnetization directions. The polarization rotation is also independent of the excitation polarization direction (Figure 4.8). We also observe polarization rotation of the 76.9 cm^{-1} A_{1g} peak at 15 K in Fig. AIII.1, albeit with much smaller rotation as compared to the 127.4 cm^{-1} peak.

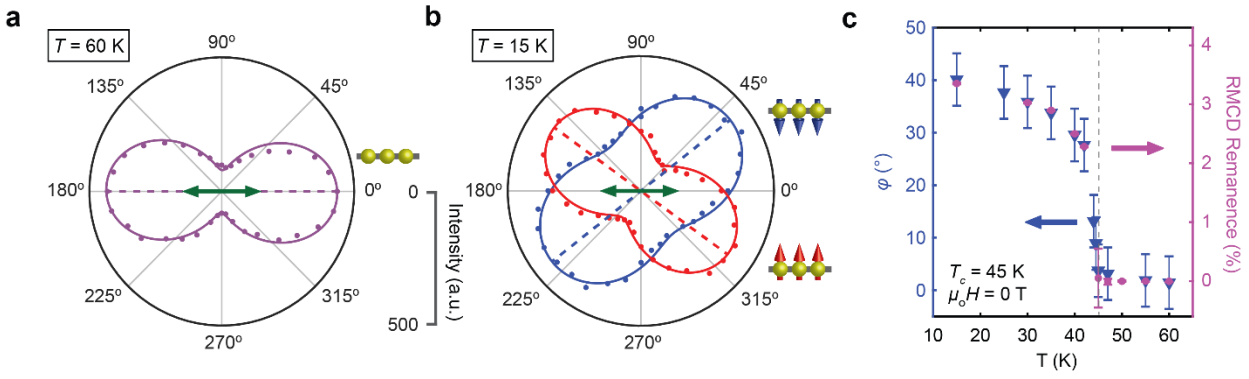

Figure 4.7. The effects of ferromagnetic order on the linear polarization of inelastically scattered light in monolayer CrI_3. (a-b) Polarization patterns of the 127.4 cm^{-1} A_{1g} mode in (a) the paramagnetic state (purple) at 60 K and (b) the two ferromagnetic states, spin-up (red) and spin-down (blue), at 15 K. The green arrow denotes the incident laser polarization. (c) Raman scattering

rotation, φ (blue), and the RMCD remanence signal at zero applied magnetic field (magenta) plotted as a function of temperature. All data in this figure was taken at zero applied magnetic field. Reproduced from ref. [57].

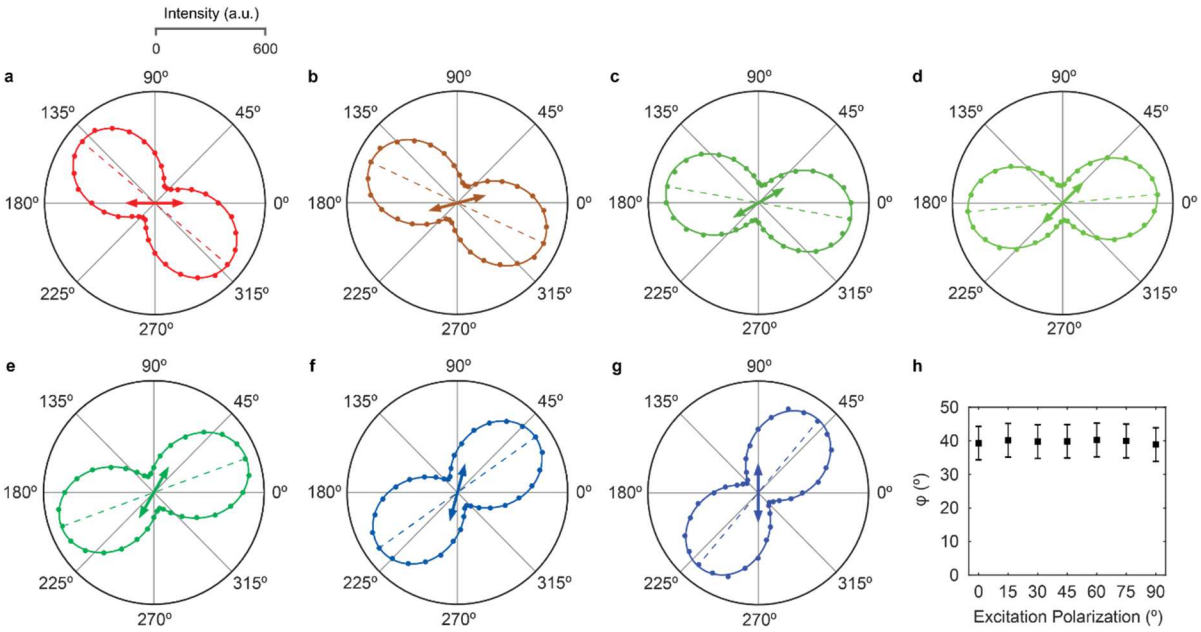

Figure 4.8. Independence of Raman scattering rotation on excitation linear polarization. (a-g) Polarization patterns of the 127.4 cm^{-1} A_{1g} mode in a CrI_3 monolayer for select incident laser polarizations denoted by the double-sided arrows. (h) Raman scattering rotation, ϕ, of the 127.4 cm^{-1} A_{1g} mode in a CrI_3 monolayer as a function of the incident laser polarizations taken in (a-g). Reproduced from ref. [57].

We also mapped these polarization patterns at higher temperatures and found that the polarization rotation decreases with the same power-law dependence as the RMCD remanence plotted in Fig. 4.7c. The continuous evolution of the polarization axis across T_C as well as the equal, but opposite rotation between the two ferromagnetic states (see Figure 4.9 for individual polarization patterns at each temperature) confirms that the scattering observed in the XY channel is from the 127.4 cm^{-1} A_{1g} phonon. This also implies that the polarization rotation is a signature of spin-phonon coupling.

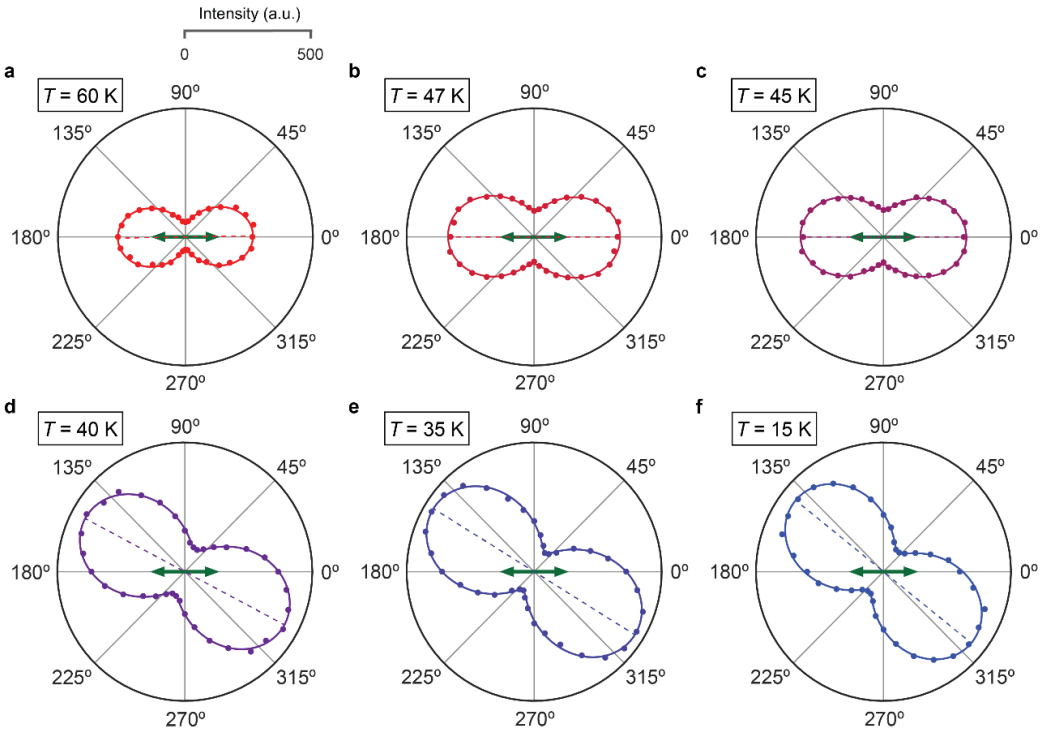

Figure 4.9. Temperature-dependent Raman scattering rotation and RMCD measurements. (a-f) Raman scattering polarization patterns of the 127.4 cm^{-1} A_{1g} phonon at select temperatures while cooling to 15 K from above T_c. Green double-sided arrows show the laser excitation polarization and dotted lines show the polarization axis of the resultant Raman scatter (g) Magnetic field-dependent RMCD measurements at the same temperatures shown in (a-f). Reproduced from ref. [57].

In principle, time-reversal symmetry breaking can lead to Hall-like, antisymmetric components in the Raman tensor and hence polarization rotation of scattered light. To derive this, we look at the magnetic point group of monolayer CrI_3 in the ferromagnetic state which is $D_{3d}(C_{3i})$ = C_{3i} + $\theta c_2' C_{3i}$, where θ is the time-reversal operator and c_2' is an in-plane rotation axis. The first term of the point group representation is independent of time-reversal symmetry and hence the original non-magnetic space group, while the second term involves time-reversal symmetry breaking due to ferromagnetic order. Given that the Raman tensor of a mode transforms according

to its representation, we find the Raman tensor for the A_{1g} mode in the ferromagnetic phase to have the general form:

$$R_{FM} = R_i + R_c = \begin{pmatrix} A & 0 & 0 \\ 0 & A & 0 \\ 0 & 0 & B \end{pmatrix} + \begin{pmatrix} 0 & C & 0 \\ -C & 0 & 0 \\ 0 & 0 & 0 \end{pmatrix} = \begin{pmatrix} A & C & 0 \\ -C & A & 0 \\ 0 & 0 & B \end{pmatrix}.$$

where R_i describes the non-magnetic scattering from the XX channel and R_c the magnetism-related scattering in the XY channel. The parameter C in R_i can be complex when the excitation is resonant with an electronic transition. Indeed, by calculating the scattering intensity as a function of the analyzing polarization, θ, using R, we find that $I \sim \cos^2(\theta - \varphi)$, the non-magnetic A_{1g} polarization pattern but rotated by $\varphi = \tan^{-1}(|C|/A)$. This is precisely what we observe in experiment, and further confirms that spin-phonon coupling leads to Raman scattering in the XY channel at 127.4 cm^{-1}.

While it is unclear what the microscopic origins are of the spin-phonon coupling in the A_{1g} Raman modes, the polarization rotation is certainly unprecedented, especially coming from a monolayer ferromagnet. As a comparison, the Kerr rotation from MOKE is around 5 mrad or ~0.2^o on a monolayer CrI_3 flake, two orders of magnitude smaller than the polarization rotation of the 127.4 cm^{-1} A_{1g} peak.

Lastly, we switch over to measuring the Raman spectra from monolayer CrI_3 in the circular polarization basis to further identify spin-phonon effects from the ferromagnetic order. Figures 4.10a-c show the Raman scattering of the 127.4 cm^{-1} A_{1g} peak in the σ^+/σ^+, σ^+/σ^-, σ^-/σ^+ and σ^-/σ^- channels where the first denotes the helicity of the incident light and the second denotes the helicity of the scattered light. We illustrate σ^+/σ^+ and σ^-/σ^- in the inset of Fig. 4.10a for clarity. Above T_C at 60 K, we observe Raman scattering from the 127.4 cm^{-1} mode (Fig. 4.10a) that is equal in both the helicity-preserving channels: σ^+/σ^+ and σ^-/σ^-. Likewise, there is negligible scattering in the cross-helicity channels, σ^+/σ^- and σ^-/σ^+. When the monolayer is in the ferromagnetic spin-up state at 15 K, Raman scattering is dominated by the σ^+/σ^+ channel as shown in Fig. 4.10b. In the

oppositely magnetized state, σ^-/σ^- is found to be the dominant scattering channel (Fig. 4.10c), the exact time-reversed process to what was observed in the spin-up state.

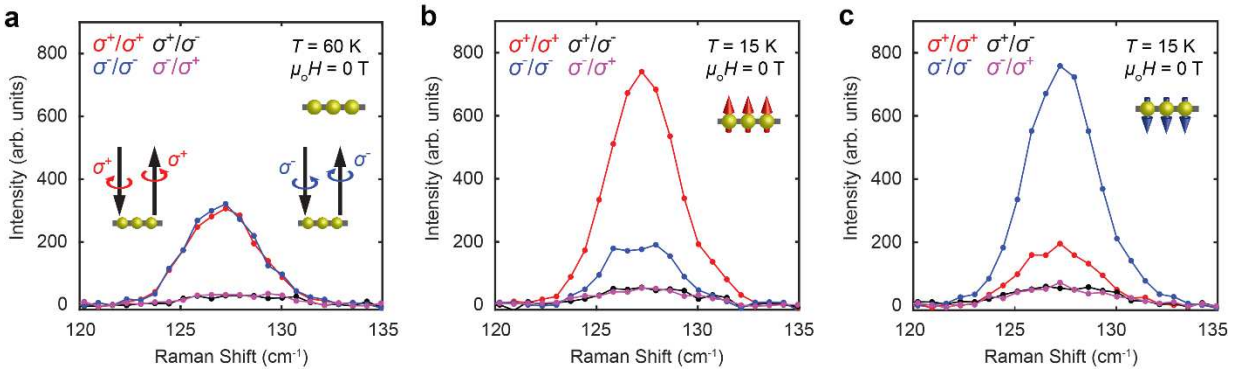

Figure 4.10. The effects of ferromagnetic order on the circular polarization of inelastically scattered light in monolayer CrI_3. Helicity-resolved Raman spectra of the A_{1g} peak in (d) the paramagnetic state at 60 K and the two ferromagnetic states, (e) spin-up and (f) spin-down at 15 K. Insets in (d) depict the Raman scattering channels with identical helicities between the incident and scattered light. Reproduced from ref. [57].

We can recover these experimental results in the circular polarization basis by calculating the expected Raman scattering intensities from the A_{1g} Raman tensor that we deduced through group theory analysis. We first calculate the Raman scattering intensities for the co-circular channels. The ket notation for the circular basis is: $|\pm\rangle = \frac{1}{\sqrt{2}}\begin{bmatrix}1\\ \mp i\\ 0\end{bmatrix}$, where $|+\rangle$ and $|-\rangle$ represent right- and left-circularly polarized light, respectively. The calculated Raman scattering intensity, I_{++}, from an A_{1g} phonon mode in the ferromagnetic phase of monolayer CrI_3 in the σ^+/σ^+ channel is:

$$I_{++} = |\langle +|R_{FM}|+\rangle|^2 = \left|\frac{1}{2}\begin{bmatrix}1 & i & 0\end{bmatrix}\begin{bmatrix}A & C & 0\\ -C & A & 0\\ 0 & 0 & B\end{bmatrix}\begin{bmatrix}1\\ -i\\ 0\end{bmatrix}\right|^2 = A^2 + |C|^2 + 2A \cdot Im(C)$$

In the σ^-/σ^- channel, the expected Raman scattering intensity, I_{--}, is:

$$I_{--} = |\langle -|R_{FM}|-\rangle|^2 = \left|\frac{1}{2}[1 \quad -i \quad 0]\begin{bmatrix} A & C & 0 \\ -C & A & 0 \\ 0 & 0 & B \end{bmatrix}\begin{bmatrix} 1 \\ i \\ 0 \end{bmatrix}\right|^2 = A^2 + |C|^2 - 2A \cdot Im(C)$$

There is a clear splitting between I_{++} and I_{--} which depends on the imaginary component of C. This implies that a splitting in the σ^+/σ^+ and σ^-/σ^- channels depends not only on the magnetization in monolayer CrI_3, but also on whether the excitation is close to an electronic resonance. Lastly, the expected Raman scattering intensity is zero for the cross-circular scattering, consistent with the absence of Raman scattering in the σ^+/σ^- and σ^-/σ^+ channels in Figs. 4.10a-c.

4.4 RAMAN ACTIVATION OF VIBRATIONAL MODES THROUGH SYMMETRY CONTROL IN BILAYER CrI_3

Next, we explore the effects of magnetic order on the magneto-optical Raman scattering from bilayers of CrI_3. Unless stated otherwise, all the following measurements were performed at 15 K. Unlike the monolayer, at zero magnetic field, two peaks distinct in energy appear at 126.7 cm^{-1} and 128.8 cm^{-1} in the XY and XX channels respectively (Fig. 4.11a). When the field is above the spin-flip transition (0.7 T) to fully align the spins, only a single peak is observed at 128.8 cm^{-1} in both the XX and XY channels (Fig. 4.11b). Figures 4.11c&e show the Raman intensity of these channels plotted as a function of magnetic field and Raman shift, while the magnetic field-dependent RMCD signal is shown in Fig. 4.11d, providing information of the corresponding magnetic states.

Starting with the XX channel, the mode at 128.8 cm^{-1} does not change in either energy or intensity as the magnetic field varies (Fig. 4.11e). In contrast, the XY channel in Fig. 4.11c shows that the 126.7 cm^{-1} peak present in the antiferromagnetic states is abruptly suppressed when the bilayer is switched to the ferromagnetic-like states. Simultaneously, a peak at 128.8 cm^{-1} emerges in the cross-polarized channel. The temperature dependence of the peaks in the XY channel further

confirms their magnetic origin. Above T_N ~ 45 K, we only observe a single co-linearly polarized peak at 128.1 cm^{-1} which slightly blueshifts to 128.8 cm^{-1} as the bilayer is cooled to 15 K (Fig. 4.12). Below T_N, both cross-polarized peaks at 126.7 cm^{-1} (antiferromagnetic state, Figs. 4.12a&b) and 128.8 cm^{-1} (ferromagnetic-like state, Figs. 4.12c-f) appear with the onset of magnetic order.

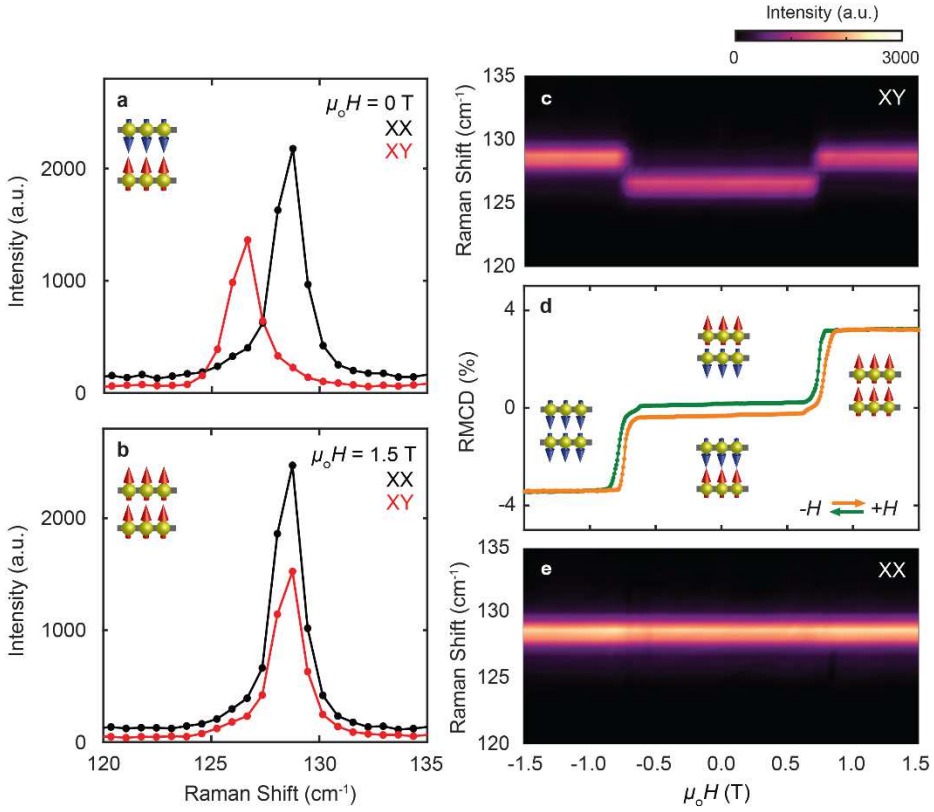

Figure 4.11. Coupling of magnetic order and Raman optical selection rules in bilayer CrI_3. (a-b) Co- (black) and cross-linearly (red) polarized Raman spectra taken in (a) an antiferromagnetic state at zero applied magnetic field and (b) the fully spin-up ferromagnetic-like state at 1.5 T, with zero applied gate voltage. (c) Color map of Raman spectra at a range of applied magnetic fields swept from 1.5 T to -1.5 T in the cross-linear scattering channel. (d) Magnetic field dependent RMCD signal of the same bilayer. (e) Color map of Raman spectra taken in the co-linear scattering channel**.** Reproduced from ref. [57].

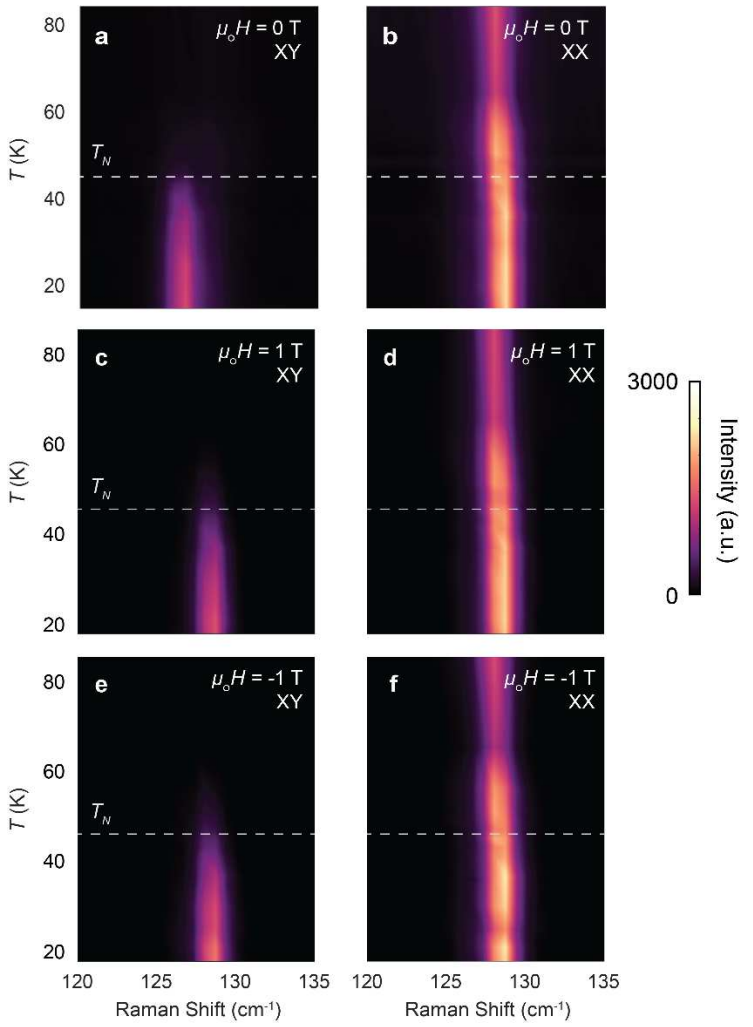

Figure 4.12. Temperature dependence of co- and cross-linearly polarized light Raman scattered from the 126.7 and 128.8 cm^{-1} modes in bilayer CrI_3. Color maps of the temperature dependence in both the XX and XY Raman scattering channels with (a-b) zero applied field, (c-d) an applied magnetic field of 1 T and (e-f) -1 T. T_N is demarcated by the gray dashed line. Adapted from ref. [57].

The appearance of the two Raman peaks in the antiferromagnetic state and the dependence of the cross-linearly polarized spectra on the magnetic order can be understood by treating the CrI_3 bilayer as a coupled spring system[133,134]. In a bilayer, weak vdW interactions between the two layers split each phonon mode in the monolayer into two modes (*i.e.* Davydov splitting). Given that the lattice of bilayer CrI_3 is centrosymmetric, we can classify one of the two modes as an odd-

parity mode (*u*) and the other as an even-parity mode (*g*). For the 127.4 cm^{-1} A_{1g} mode in the monolayer, Davydov splitting in the bilayer results in a lower-energy 126.7 cm^{-1} *u* mode, in which the layers vibrate out-of-phase as depicted in Fig. 4.13a, and a higher-energy 128.8 cm^{-1} *g* mode with in-phase vibrations between the layers (Fig. 4.13b). Since Raman scattering is an even-parity process, this implies that the even-parity 128.8 cm^{-1} *g* mode is Raman-active, while the odd-parity 126.7 cm^{-1} *u* mode is infrared-active but Raman-silent. This is consistent with the Raman spectra above T_N (Fig. 4.12).

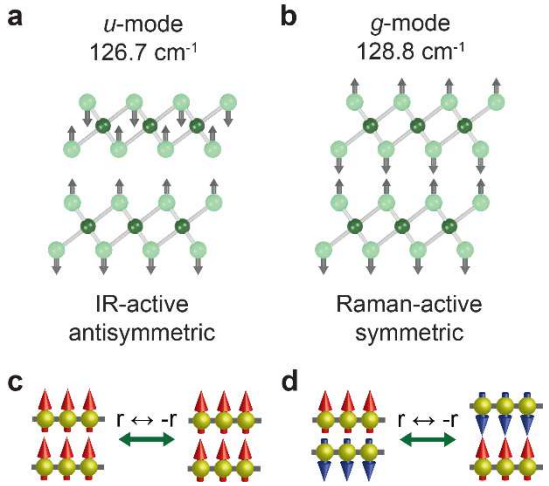

Figure 4.13. Davydov-splitting and the combined time-reversal and inversion symmetry in bilayer CrI_3. (a-b) Illustrations of the two Davydov-split A_{1g} modes in a CrI_3 bilayer: (a) an infrared (IR)-active *u* phonon mode at 126.7 cm^{-1} and (b) a Raman-active *g* phonon mode at 128.8 cm^{-1}. (c) In the ferromagnetic-like states, applying **-r** preserves the spin orientation, and therefore the centrosymmetry of the entire bilayer. (d) On the other hand, applying the inversion operation, **-r,** in the layered antiferromagnetic states switches the spin orientation of the two layers, thus breaking centrosymmetry. However, the combined time-reversal and inversion symmetry still holds. Adapted from ref. [57].

Factoring in magnetic order leads to remarkable changes to the Raman optical selection rules. For the fully spin-polarized state, centrosymmetry remains intact (Fig. 4.13c), so it should behave exactly like the FM monolayers: the 128.8 cm^{-1} *g* mode is active in both the XX and XY

channels, while the 126.7 cm^{-1} *u* mode remains silent. This is consistent with experimental findings. A comparison of the linear polarization patterns between the 127.4 cm^{-1} A_{1g} phonon mode in the ferromagnetic monolayer (Figs. 4.14a&b) and the 128.8 cm^{-1} *g* mode in the ferromagnetic-like bilayer shows virtually the same degree of polarization rotation (Figs. 4.14c&d).

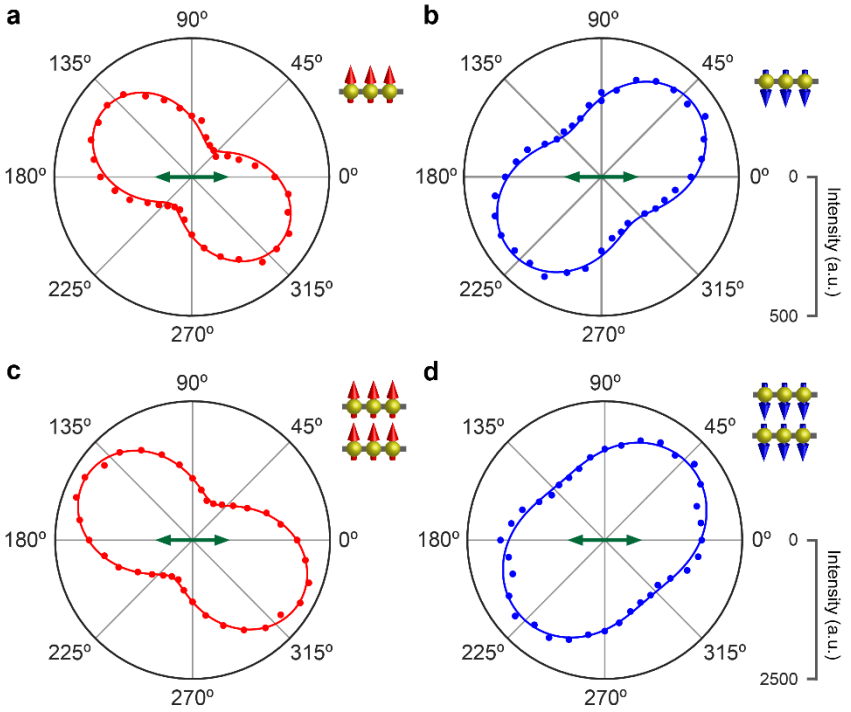

Figure 4.14. Raman scattering rotation from bilayer CrI_3 in the fully spin-polarized states. (a-b) Monolayer polarization patterns of the 127.4 cm^{-1} phonon in (a) the spin-up and (b) spin-down states. (c-d) Polarization patterns of the 128.8 cm^{-1} mode in bilayer CrI_3 in the (c) fully spin-up polarized and (d) fully spin-down polarized states. The sign of the Raman scattering rotation in each spin state is the same and the magnitude of the rotation roughly equal between the monolayer and the bilayer. Green double-sided arrows show the laser excitation polarization. Adapted from ref. [57].

In the antiferromagnetic states, parity no longer applies since the antiparallel spin configuration breaks inversion symmetry (Fig. 4.13d). Yet, the system remains invariant under the combined time-reversal and inversion symmetry, which forbids Raman activity in the Hall-like

component in the Raman tensor of the *g* mode. On the other hand, since the 126.7 cm^{-1} *u* mode breaks inversion symmetry explicitly, it can be active in the XY channel shown in Fig. 4.11a. This is further confirmed by the polarization patterns of the 126.7 cm^{-1} *u* mode and 128.8 cm^{-1} *g* mode in the antiferromagnetic state which shows that their polarization axes are perpendicular and parallel to the excitation polarization, respectively (Fig. 4.15). Davydov splitting of the 76.9 cm^{-1} A_{1g} peak into two phonon modes at 76.4 cm^{-1} and 77.4 cm^{-1} is also observed (Fig. AIII.2). These modes have the same selection rules as the pair of phonons at 126.7 cm^{-1} and 128.8 cm^{-1} respectively.

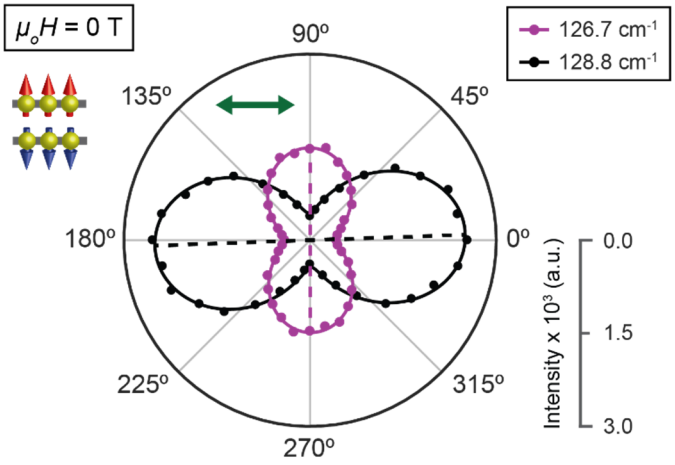

Figure 4.15. Polarization dependence of Dayvdov-split modes in antiferromagnetic bilayer CrI_3. Polarization patterns of the 126.7 cm^{-1} *u* mode (purple) and the 128.8 cm^{-1} *g* mode (black) of bilayer CrI_3 taken at T = 15 K without an applied magnetic field. Dashed lines correspond to the polarization axis of inelastically scattered light. Green double-sided arrow represents the excitation polarization. Clearly, the 126.7 cm^{-1} *u* mode is cross-linearly polarized with respect to laser while 128.8 cm^{-1} *g* mode is co-linearly polarized. Reproduced from ref. [57].

To understand in detail the selection rules of these modes, we treat the bilayer CrI_3 as two weakly coupled FM monolayers. The Raman tensor of a monolayer can be decomposed into a spin-independent, diagonal part (R_i), and a spin-dependent, anti-symmetric part (R_c) as derived in Section 4.3, with R_i describing scattering in the XX channel and R_c in the XY channel. If the

magnetization is flipped, R_i remains the same while R_c changes sign. Under the weak coupling assumption, the Stokes and anti-Stokes component of the total induced electric dipole moment can be written as $p(t) = \sum_{l=1}^{2}(R_i^l + R_c^l)Q^l\,Ee^{i(\omega\pm\Omega)t}$, where l is the layer index, Q is the normal coordinate of the phonon, E is the electric field, and ω and Ω are the photon and phonon frequencies, respectively.

In the AFM state, we have $R_i^1 = R_i^2 = R_i$ and $R_c^1 = -R_c^2 = R_c$. The normal coordinates are $Q^1 = -Q^2 = Q$ for the *u* mode and $Q^1 = Q^2 = Q$ for the *g* mode. The total induced dipole moment for the two modes are $p_{u,\mathrm{AFM}} = 2R_cQ\,Ee^{i(\omega\pm\Omega)t}$ and $p_{g,\mathrm{AFM}} = 2R_iQ\,Ee^{i(\omega\pm\Omega)t}$. Therefore, the *u* mode is active only in the XY channel, and the *g* mode in the XX channel. For the fully spin-polarized state, the key difference from the AFM state is that $R_c^1 = R_c^2 = R_c$. This leads to $p_{g,\mathrm{FM}} = 2(R_i + R_c)Q\,Ee^{i(\omega\pm\Omega)t}$, and $p_{u,\mathrm{FM}} = 0$. Consequently, the *g* mode is active in both the XX and XY channels while the *u* mode is silent. This analysis precisely matches our experimental observations.

We can also arrive at these selection rules for the *g* and *u* modes via group theory analysis. CrI_3 bilayers are in the monoclinic phase. This is represented by the symmetry group, $C_{2h} = \{e, c_2', i, \sigma_\perp\}$, where e is the identity operator, c_2' is the two-fold rotation with an in-plane axis, i is the inversion operator, and $\sigma_\perp$ is a reflection whose mirror plane is normal to c_2'.[135] The two Davydov-split phonon modes *g* and *u* transform under C_{2h} as:

$$e|g\rangle = |g\rangle,\ c_2'|g\rangle = |g\rangle, \qquad i|g\rangle = |g\rangle,\ \sigma_\perp|g\rangle = |g\rangle$$

$$e|u\rangle = |u\rangle,\ c_2'|u\rangle = -|u\rangle, \qquad i|u\rangle = -|u\rangle,\ \sigma_\perp|u\rangle = |u\rangle$$

Applying the time-reversal operator has no effect on the phonon modes and leaves them unchanged. Considering magnetic structure, however, leads to distinct magnetic point groups between the ferromagnetic-like and the antiferromagnetic states. In the ferromagnetic-like state,

the magnetic point group is $C_{2h}(C_i) = \{e, i, \theta c_2', \theta\sigma_\perp\}$. The presence of inversion symmetry (i) renders the *u* mode silent in both XX and XY channels and the lack of time-reversal (θ) allows the Raman tensor for the *g* mode to develop an antisymmetric component. For the antiferromagnetic state, its magnetic point group is $C_{2h}(C_2) = \{e, c_2', \theta i, \theta\sigma_\perp\}$. Again by requiring that the Raman tensor transform according to the same representation of the corresponding phonon mode, we find that the *g* mode is silent in the XY channel and the *u* mode is silent in the XX channel.

Unlike the A_{1g} modes, Davydov splitting is not observed in the E_g modes. This is not surprising since the E_g modes in the monolayer are not visibly affected by magnetic order, implying that the terms related to the magnetic order are negligibly small or do not couple to the excitation based on the scattering geometry. These additional terms, however, are what enable the Raman activity of the odd Davydov-split A_{1g} modes at 126.7 cm^{-1} and 76.4 cm^{-1}. Thus, because the terms related to the magnetic order in the E_g Raman tensors are negligibly small, Raman activity of the odd Davydov-split E_g mode will not be detectable through Raman scattering measurements.

Lastly, we demonstrate magnetoelectrical control over the Davydov-split phonons by electrically switching the magnetic states of a bilayer device shown in Figures 4.16a&b. The magnetic field-dependent Raman intensity plot taken near the spin-flip transition at an applied gate voltage V_g of 0 V (5 V) is shown in Fig. 4.16c (d). The magnetic field at which the 126.7 cm^{-1} peak is activated/suppressed is modulated from -0.7 T to -0.6 T, consistent with previous electrical control of the spin-flip transition[98,104]. Parking the magnetic field at -0.62 T, Figs. 4.16e&f compare the co- and cross-linearly polarized Raman spectra at two different V_g, 0 V and 5 V. At 5 V, the 126.7 cm^{-1} peak is suppressed while the 128.8 cm^{-1} peak is activated in the XY channel as the positive V_g switches the magnetic states. In Fig. 4.16g, we continuously sweep the applied gate voltage from -1 V up to 6 V and monitor the Raman activity of the 126.7 cm^{-1} and 128.8 cm^{-1}

phonons in the XY channel. The gradual suppression of the 126.7 cm^{-1} phonon and the emergence of the 128.8 cm^{-1} phonon track exactly the gate-dependent RMCD signal (Fig. 4.16h) with progressively larger negative RMCD signal as the bilayer is switched from an AFM state to the fully spin-down polarized state. From these measurements, we confirm the magnetoelectrical switching of the 126.7 cm^{-1} phonon mode through electrostatic control of the magnetic states, and hence the Raman selection rules, in a gated CrI_3 bilayer device.

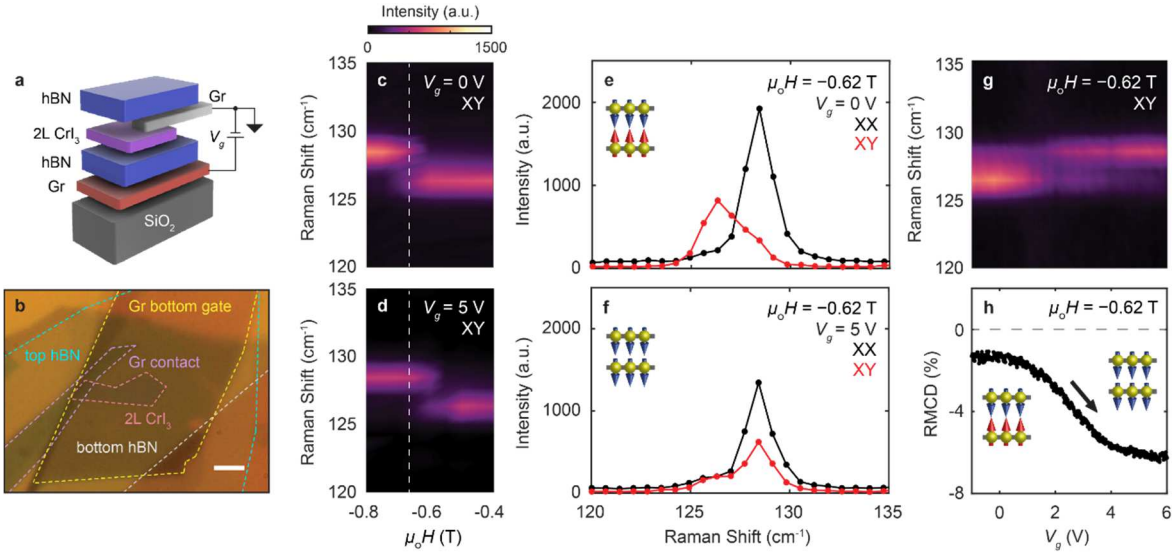

Figure 4.16. Electrical switching of a Raman-silent phonon in bilayer CrI_3. (a) Schematic of a gated CrI_3 bilayer device. (b) Optical micrograph of the assembled gated CrI_3 bilayer device drawn in (a). Scale bar is 5 μm. (c-d) Color map of Raman spectra at a range of applied magnetic fields swept from -0.4 T to -0.8 T in the cross-linear scattering channel of a CrI_3 bilayer device taken at an applied gate voltage of (c) 0 V and (d) 5 V. The white dashed line denotes the magnetic field at which the spin-flip transition occurs in the ungated CrI_3 bilayer. (e-f) Co- (black) and cross-linearly (red) polarized Raman spectra taken at an applied gate voltage of (e) 0 V and (f) 5 V. (g) Color map of cross-linearly polarized Raman spectra taken at range of applied gate voltages from -1 V to 6 V at a fixed magnetic field of -0.62 T. (h) RMCD signal of the same device taken in the same experimental conditions as in (g). The gray dashed line demarcates zero RMCD signal. Reproduced from ref. [57].

4.5 SUMMARY AND FUTURE DIRECTIONS

In this chapter, we have demonstrated emergent spin-phonon effects in atomically thin CrI_3. In the spin-polarized phases of monolayer and bilayer CrI_3, clear magneto-optical rotation of inelastically scattered light is observed by the A_{1g} phonon at ~128 cm^{-1}. This rotation is a consequence of a Hall-like component in the Raman tensor A_{1g} tensor that arises due to net out-of-plane magnetic order. In bilayer CrI_3, the A_{1g} phonon exhibiting spin-phonon coupling Davydov splits, due to interlayer vdW forces between the layers, into a parity-even *g* mode and a parity-odd *u* mode. The combination of inversion symmetry and layered antiferromagnetism leads to a loss of centrosymmetry in the bilayer, allowing the parity-odd *u* mode to become Raman active in the cross-linearly polarized scattering channel. Switching to the spin-polarized state via magnetic and electric fields suppresses the Raman activity of this state and demonstrates the tuning of these selection rules via symmetry control. This work has been confirmed through other independent research groups, who have also investigated this spin-phonon coupling in thicker flakes of CrI_3[132,136].

The current microscopic understanding for why the spin-phonon coupling in CrI_3 leads to polarization rotation is currently not known. One peculiar aspect of the Raman tensor derived from group theory principles suggests a Hall-like component in the polarizability of the electron cloud. Whether this Hall-like term originates from electronic resonance effects or from something more exotic such as Berry curvature of the phonon wavefunction warrants further investigation. For instance, one could perform an excitation energy-dependent study of the Raman features in CrI_3 to see how the magneto-optical effects change. If the effects change in accordance with how the MOKE or RMCD signal changes (amplitude and sign), then the magneto-optical Raman effect is likely from magnetism-related changes to the electronic band structure.

Further magnetic field-dependent Raman studies are also needed in thicker flakes of CrI_3 to confirm that the switching of phonon selection rules is indeed related to Davydov splitting and combined time-reversal and inversion symmetry breaking. This could be paired with infrared spectroscopy measurements of these thicker flakes to determine the number of Raman-active and infrared-active modes, since Davydov splitting results in ceil(N/2) Raman-active modes and floor(N/2) infrared-active modes for an N-layer CrI_3 flake, where ceil (floor) rounds N/2 up (down) to the nearest integer.

Chapter 5. DIRECT OBSERVATION OF 2D MAGNONS IN ATOMICALLY THIN CRI_3

In this chapter, we investigate symmetry-related magneto-optical effects pertaining to quantized spin waves, *i.e.* magnons, in atomically thin CrI_3. First, we first intuit why spin waves are magnetic excitations of a magnetic material and briefly look at the characteristics of magnons such as their energy gap and dispersion. Then we probe using Raman spectroscopy, the magnon modes of monolayer and bilayer CrI_3, positing their selection rules through both angular momentum conservation and group theory considerations. This chapter closely follows my work in *J. Cenker et al.* "Direct observation of 2D magnons in atomically thin CrI_3" which has been published into *Nature Physics* in 2020[137].

5.1 MAGNONS: QUASIPARTICLE EXCITATIONS OF MAGNETIC ORDER

We begin our discussion with the origin of spin waves. The ground state of the ferromagnetic state is one in which all spins point in the same direction along an easy axis (Figure 5.1a): the total magnetic moment of the system maximally points along the easy axis. An excited state then could be achieved, for instance, by misaligning one of the spins, either thermally or via an external field, as illustrated in Figure 5.1b. This has the effect of lowering the total projected magnetic moment along the easy axis. The relaxation dynamics of the disoriented spin is governed by the Landau-Lifshitz-Gilbert equation[138,139], which essentially finds that the spin returns to the ground state through decaying orbital motion around the easy axis, illustrated in Figure 5.1c. While the misaligned spin is precessing, exchange and magnetostatic interactions with nearest-neighbor sites result in the transmission of this precessing motion to other spins in the ferromagnet (Fig. 5.1d). This propagation of spin precession is the basis for spin waves in magnetic materials.

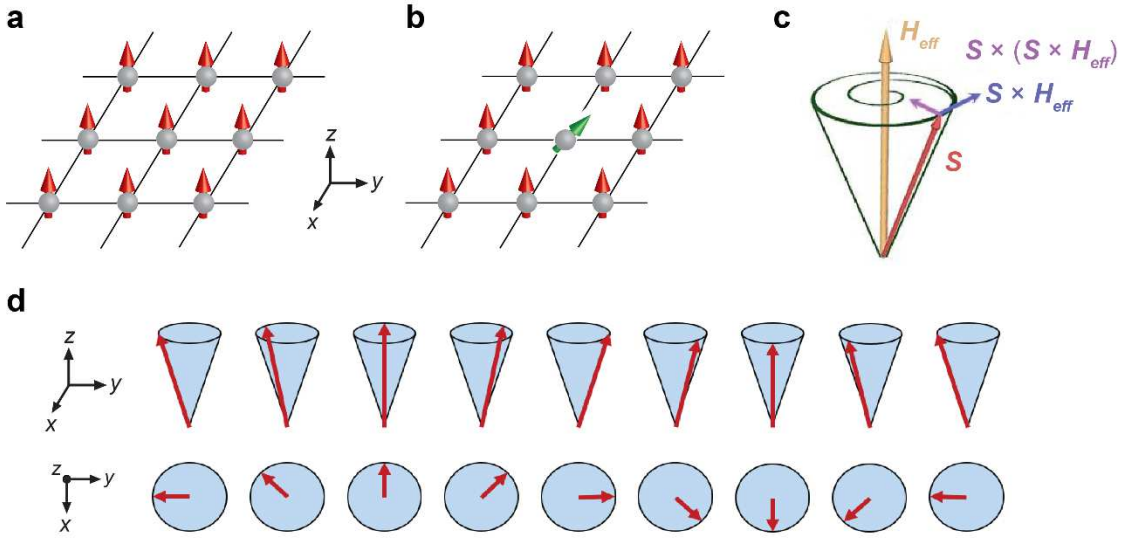

Figure 5.1. Magnetic excitations and spin waves. (a) Illustrations of ferromagnetically interacting spins in a square lattice with out-of-plane magnetic anisotropy. (b) Thermal or external perturbations kick a spin (green arrow) in the middle of the square lattice out-of-alignment with the rest of the spins. (c) Magnetization dynamics of a perturbed spin that is precessing back to its original out-of-plane alignment in (a). These dynamics are governed by the Landau-Lifshitz-Gilbert equation, which consists of a tangential force, $\boldsymbol{S} \times \boldsymbol{H_{eff}}$, and a centripetal force, $\boldsymbol{S} \times (\boldsymbol{S} \times \boldsymbol{H_{eff}})$, where $\boldsymbol{S}$ is the spin vector and $\boldsymbol{H_{eff}}$ represents an effective magnetic field that encompasses the external applied magnetic field, $\boldsymbol{H}$, anisotropy, and exchange interactions.

Furthermore, these spin waves can be quantized as quasiparticles known as magnons and are diagonalizable by the system Hamiltonian[42,140]. The number of magnon modes in a material is determined by the number of spin sites per unit cell. For a material with one spin site per unit cell, the energy dispersion, E_k, of the magnon mode has the following expression:

$$E_k = \Delta_o + 2\mu_B\mu_o H + 2JS(1 - \cos ka)$$

where Δ_o is the magnetic anisotropy, and k is the wavevector in the Brillouin zone. From this expression, we find that the magnon energy is a linear function of $\mu_o H$, shifting with a g factor of 2 and $S = 1$. In the absence of an external magnetic field, the energy minimum centered at $k = 0$ *i.e.* the Γ-point is known as the spin wave gap and is simply equal to the strength of the magnetic

anisotropy. In principle, magnons can also be produced/annihilated through Raman scattering, though magnetic anisotropies above ~0.3 meV are required since confocal Raman microscopy only detects inelastic scattering from Γ-point quasiparticles.

5.2 2D MAGNONS IN MONOLAYER CrI_3

To start, we will first intuit the magnon modes in monolayer CrI_3. There are two Cr^{3+} ions per unit cell, so two magnon modes are expected. One magnon mode is found to be a low-energy acoustic mode with in-phase precession (Fig. 5.2a) and the other a higher-energy optical mode with out-of-phase precession (Fig. 5.2b)[132,141]. The spin wave gap, determined by the strong magnetic anisotropy in monolayer CrI_3, is theoretically predicted to be around 0.3 to 0.4 meV (2.4 – 3.2 cm^{-1})[42,142]. This energy scale is just accessible experimentally with our Raman microscope which has a resolution of ~3 cm^{-1}.

To ensure that our monolayer CrI_3 samples (optical image of representative flake in Figure 5.2c, left inset) are ferromagnetic, we look at their RMCD signal as a function of magnetic field at 15 K. As shown in the right inset of Figure 5.2c, the RMCD trace shows magnetic hysteresis, indicating that ferromagnetic order is present in the monolayer. This is further confirmed by RMCD spatial mapping of the monolayer at zero applied magnetic field, which shows large, uniform RMCD signal across the entire flake. This is indicative that the monolayer flake is uniformly magnetized as a single-domain ferromagnet.

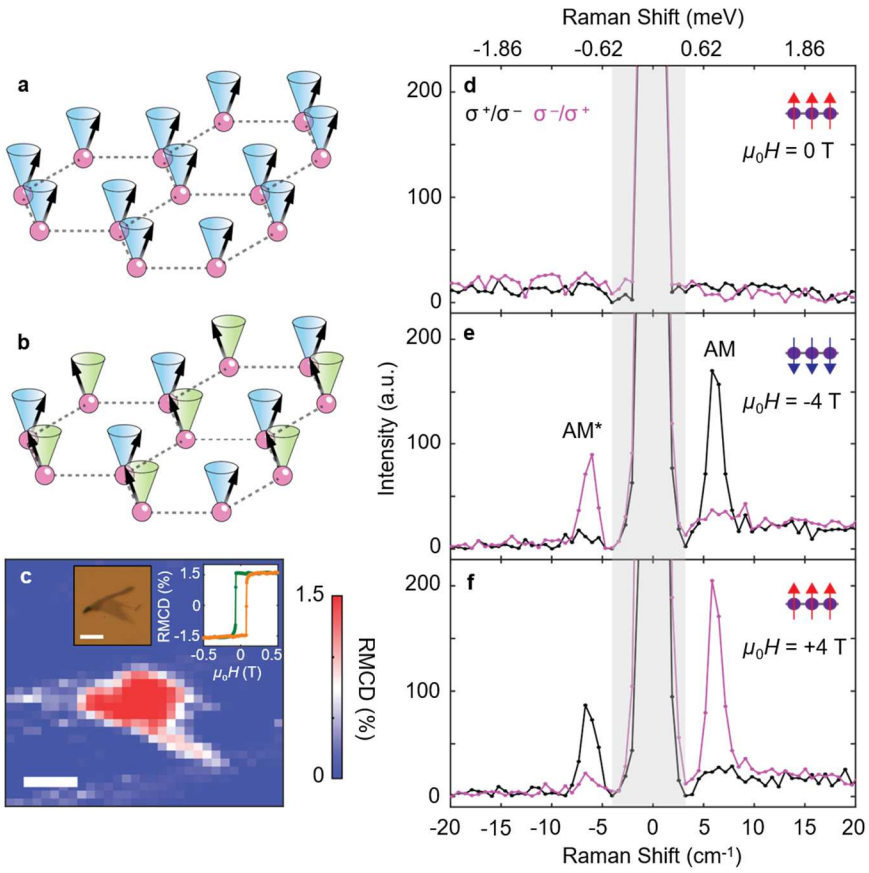

Figure 5.2. Spin waves illustrations of monolayer CrI_3, magnetic characterization and low-frequency Raman spectra. (a-b) Depiction of the two types of spin waves in ferromagnetic monolayer CrI_3: (a) corresponds to the in-phase acoustic mode while (b) corresponds to the out-of-phase optical one. (c) Zero-field reflective magnetic circular dichroism (RMCD) map of an encapsulated monolayer CrI_3 flake. Scale bar: 4 μm. The right inset shows an RMCD sweep taken at the center of the flake while the left inset shows an optical micrograph of the sample with a scale bar of 10 μm. (d-f) Low-frequency cross-polarized Raman spectra taken at (d) zero-field (e) -4 T, and (f) 4 T. The grey box indicates the spectral range of our optical filter below which the magnon is unresolvable. Reproduced from ref. [137].

Polarization-dependent Raman measurements were performed on atomically thin CrI_3 samples using the same experimental setup described at the end of Section 4.2. Since the Raman scattering from 2D magnons is weak, we used a laser power of ~0.4 mW and an integration time

of 2 minutes. Despite the incredibly large fluences used in these experiments, there is no laser heating as we will show later.

The cross-circularly polarized low-frequency Raman spectra of monolayer CrI_3 are plotted in Figs. 5.2d-f at select magnetic fields. The gray shaded box centered around the laser line indicate the portion of the spectrum that is rejected by the Bragg filters. Fig. 5.2d shows the Raman spectra taken with zero applied magnetic field. Clearly, there are no Raman scattering features detected around the laser line. Ramping the magnetic field magnitude to 4 T, a low-frequency feature emerges in the cross-circularly polarized channels as seen in Fig. 5.2e&f. The low-frequency mode is present on both the Stokes and anti-Stokes sides, which we label as AM and AM*, respectively. As we can see from Figs. 5.2e&f, AM and AM* obey distinctly opposite optical selection rules, *i.e.* the helicity of light which scatters off of AM is opposite to the helicity required to detect AM*. For example, with the magnetization point down (Fig. 5.2e), AM appears when excited with σ^+ light while AM* is detected through σ^- excitation. The selection rules reverse when the magnetization is flipped as seen in Fig. 5.2f. When the magnetization points up, AM couples to σ^- excitation while AM* is observed through σ^+ excitation. AM and AM* are not detected in the co-polarized channels which are instead dominated by quasi-elastic scattering from the Si substrate (Figure 5.3).

We now look at the magnetic evolution of these peaks by performing polarization-dependent Raman measurements at fixed magnetic fields from 7 T down to -7 T in 0.5 T steps. Fig. 5.4a shows a color map of the intensity of AM and AM* as a function of Raman shift and magnetic field. We extract the peak positions of AM and AM* in Fig. 5.4a and plot them as a function of magnetic field in Fig. 5.4b. Both AM and AM* exhibit highly linear shifts with applied field. The corresponding slope of this magnetic field-dependent shift is 0.94 cm^{-1}/T (.12 meV/T),

consistent with the Zeeman energy shift of a spin-1 quasiparticle that possesses a magnetic moment of 2 μ_B. Thus, we conclude that AM and AM* are the Stokes and anti-Stokes Raman scattering from 2D magnons in monolayer CrI_3.

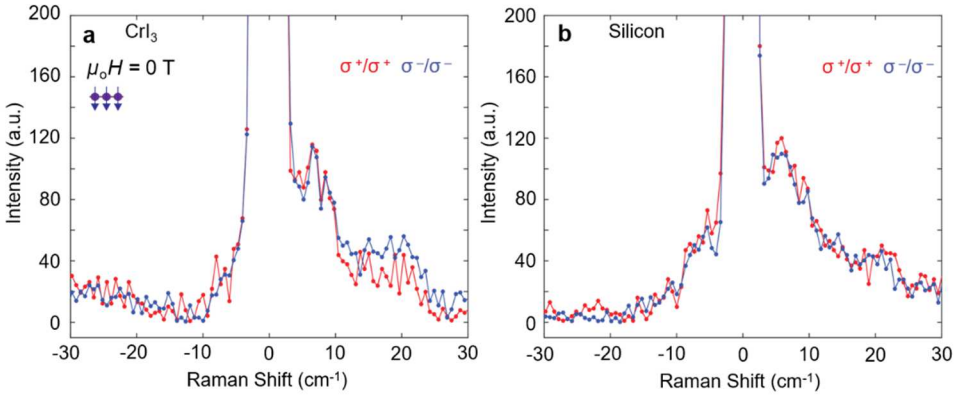

Figure 5.3. Low energy co-circularly polarized Raman scattering from monolayer CrI_3 and SiO_2. (a-b) Raman scattering in the σ^+/σ^+ (red) and σ^-/σ^- (blue) channels from (a) monolayer CrI_3 in the spin-down state and (b) SiO_2 substrate with zero applied magnetic field. Scattering features observed from the monolayer are identical to those seen from the substrate, implying that AM and AM* are not observed in the co-circular scattering channels. Adapted from ref. [137].

More specifically, AM and AM* are Raman scattering off the acoustic magnons in monolayer CrI_3. In Fig. 5.4b, we extrapolate the magnon energy to zero magnetic field. Doing so allows us to extract the spin wave gap, which we determine to be ~2.4 cm^{-1} (or ~0.3 meV), quite large for a ferromagnet due to the large magnetic anisotropy of CrI_3. The extracted spin wave gap is also in excellent agreement with the theoretical predictions in refs. [42] and [142], confirming the detection of acoustic magnons in monolayer CrI_3. We also perform magnetic-field dependent polarization-dependent Raman measurements on unexfoliated bulk CrI_3, shown in Fig. 5.5a&b. Extracting the spin-wave gap of bulk CrI_3 in Fig. 5.5c, we find that the spin wave gap is ~2.8 cm^{-1} (~0.4 meV), consistent with the monolayer spin wave gap. This implies that the only significant parameter affecting the properties of acoustic magnons is out-of-plane magnetic anisotropy.

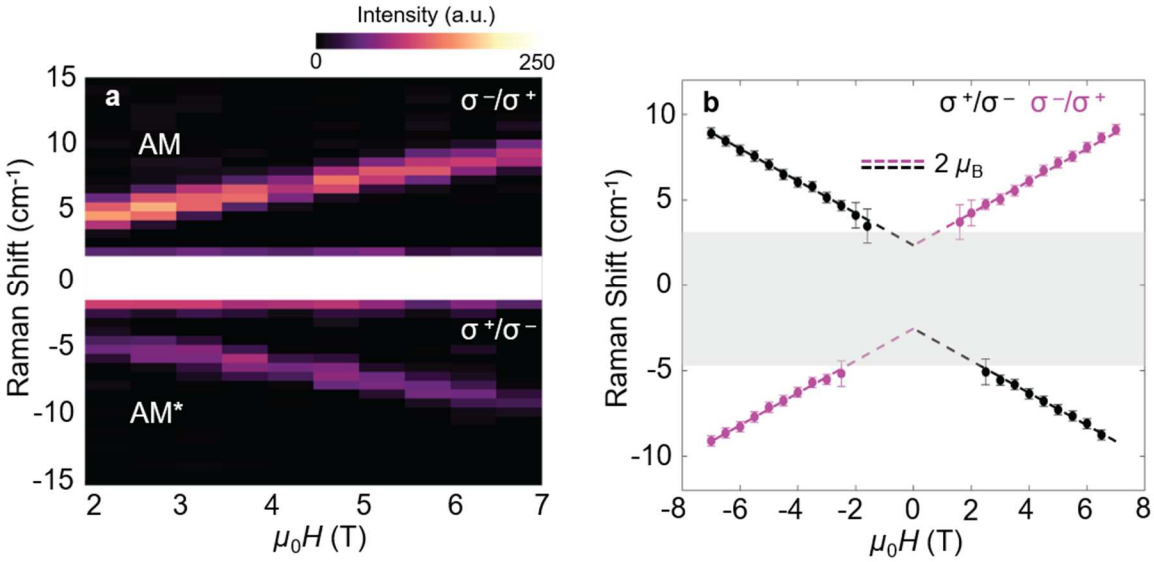

Figure 5.4. 2D acoustic magnons in a magnetic field. (a) Intensity color map of low energy Raman scattering as a function of applied magnetic field. (b) Energies of AM and AM* are extracted from (a) and plotted as a function of magnetic field. The black (purple) dots represent Raman shifts extracted from scattering features observed in the σ^+/σ^- (σ^-/σ^+) channel. The shift in peak energy as a function of magnetic field is highly linear and fits precisely to the description of a magnon with a *g*-factor of 2 (dotted lines). The gray region represents the Raman signal which is cutoff by our Bragg filters. Adapted from ref. [137].

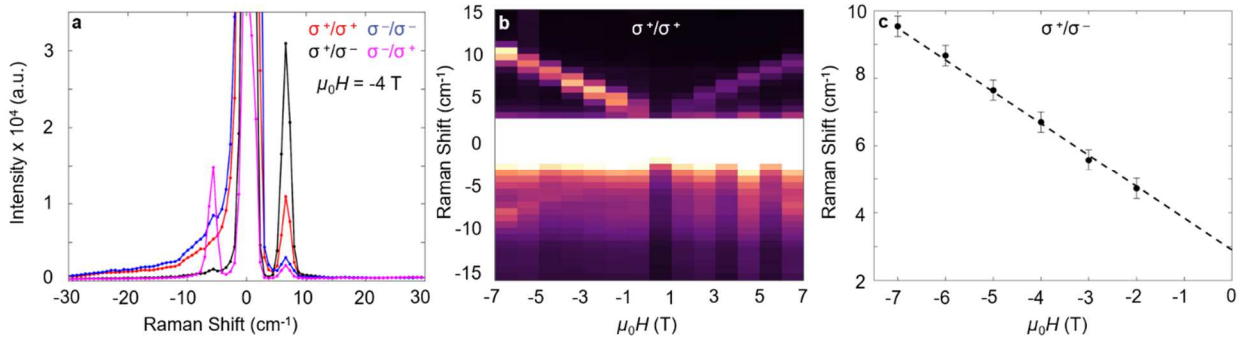

Figure 5.5. Acoustic magnon scattering in unexfoliated single crystal CrI_3. (a) Low-frequency circularly polarized Raman spectra of bulk single crystal CrI_3. Although the magnon scattering is still predominantly in the cross-circularly polarized channel, a large component appears in the co-circular σ^+/σ^+ channel. (b) Color map of the magnetic field dependence of σ^+/σ^+ scattering. The linear shift of ~2 μ_B indicates that it arises from magnon scattering and rules out acoustic phonons.

(c) The energy of the acoustic magnon from the σ^+/σ^- channel plotted as a function of magnetic field from -7 to -2 T. The dashed line indicates a shift of 2 μ_B with a zero-field energy of ~2.8 cm^{-1} and fits the energy shift of the low-energy peak well. The nearly identical zero-field energy of the acoustic magnons for all sample thicknesses highlights the intralayer nature of these spin waves and the layer-independent anisotropy from bulk single crystal down to the monolayer limit. Reproduced from ref. [137].

Lastly, we perform temperature-dependent Raman measurements to verify the magnetic origin of AM and AM* in monolayer CrI_3. Fig. 5.6 shows a color map of the Raman scattering intensity from AM and AM* plotted as a function of temperature and Raman shift. We apply a -7 T magnetic field to shift the magnon mode away from the laser line while also stabilizing the spin-polarized state at temperatures above T_C. This allows for a larger temperature range by which to study the acoustic magnon. As we warm to higher temperatures, AM and AM* gradually redshift while also slightly weakening in intensity. At ~75 K, the Raman scattering from AM and AM* is abruptly suppressed before reaching the cutoff of our Bragg filters, indicating a magnetic phase transition to a paramagnetic state.

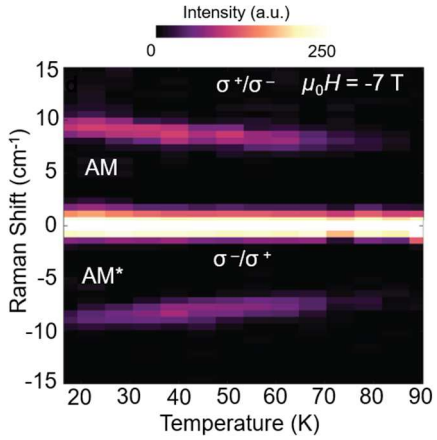

Figure 5.6. Temperature dependence of acoustic magnons in monolayer CrI_3. Color map of temperature-dependent Raman measurements indicate a gradual redshifting with temperature until the scattering vanishes at temperatures above ~80 K. Reproduced from ref. [137].

We also separately plot the individual Raman spectra at select temperatures in Fig. AIV.1. Throughout the entire temperature range, the linewidth of AM and AM* remains essentially constant through the whole temperature range that they are detectable. In other magnetic systems[143], the Raman features from magnon scattering typically broaden as the material reaches T_C or T_N. This implies that the true linewidth of AM and AM*, Γ, is limited by the resolution of our spectrometer. Given this, we quantify a lower bound on the lifetime of the acoustic magnon, τ, as $\Gamma^{-1} = 5$ ps. An actual determination of τ would require ultrafast measurements of the acoustic magnon mode such as a pump-probe technique[144].

5.3 Selection rules based on angular momentum conservation in a lattice with threefold rotation symmetry

The distinct cross-circular optical selection rules can be derived by considering the angular momentum of the photon, J_p, magnon, J_m in a honeycomb lattice (Fig. 5.7). For instance, when the magnetization points up, the total change of photon angular momentum is $\Delta J_p = \pm 2\hbar$ since the helicities between incident and scattered light are opposite, where + (−) corresponds to anti-Stokes (Stokes) scattering from the magnon mode. The change of magnon angular momentum contributes $\Delta J_m = \pm\hbar$. This leads to a total change of angular momentum that is $\Delta J_p + \Delta J_m = \pm 3\hbar$. In a system with continuous rotational symmetry, the conservation of angular momentum would forbid such a process. However, in an analogue to the Umklapp process[145,146], the threefold symmetry of the honeycomb lattice in monolayer CrI_3 allows for discrete angular momentum conservation up to modulo $3\hbar$: $|\Delta J_p + \Delta J_m|/\hbar = 0 \pmod 3$. Given that the total change of the angular momentum is a multiple of $3\hbar$, cross-circular selection rules are expected in monolayer CrI_3.

A group theory analysis also yields the cross-circular selection rules observed in monolayer CrI_3. Recall from Section 4.3 that the magnetic point group of monolayer CrI_3 is $D_{3d}(C_{3i}) = C_{3i} +$

$\theta c_2' C_{3i}$, where θ is the time-reversal operator and c_2' is an in-plane rotation axis. In Hermann-Mauguin notation, this magnetic point group is denoted by $\bar{3}m'$. Inversion symmetry is present in the system, implying that the magnon modes at Γ point are eigenstates of the parity operator. The acoustic mode can be represented by the following operator: $S_a = S_A + S_B$ where S_A and S_B are the spin operators at the A and B sublattice sites of the unit cell. We also note that S_x and S_y encode rotations in x and y, respectively, and so have E_g symmetry in the $\bar{3}m'$ magnetic point group. Thus, the Raman tensor of S_a is:

$$R_a = \begin{pmatrix} iA & -A & B \\ -A & -iA & -iB \\ B & -iB & 0 \end{pmatrix} S_a^+ + \begin{pmatrix} iC & C & D \\ C & -iC & iD \\ D & iD & 0 \end{pmatrix} S_a^-,$$

where $S_a^{\pm} = S_a^x \pm iS_a^y$. Note, the S_a^+ and S_a^- components represent the Raman tensors for Stokes and anti-Stokes scattering, respectively. If we let $|i\rangle = \begin{bmatrix} 1 \\ -i \\ 0 \end{bmatrix} \equiv |\sigma^+\rangle$, then I is only non-zero for the S_a^+ component if $|f\rangle = \begin{bmatrix} 1 \\ i \\ 0 \end{bmatrix} \equiv |\sigma^-\rangle$; the S_a^- component has an I of zero for both final helicities if $|i\rangle = |\sigma^+\rangle$. Likewise, if $|i\rangle = |\sigma^-\rangle$, I is zero for all final helicities in the S_a^+ component, and non-zero for the S_a^- component only if $|i\rangle = |\sigma^+\rangle$. These calculations of I for the different helicities and components of the acoustic mode Raman tensor confirm that this group theory analysis reproduces the acoustic magnon cross-helicity selection rules of monolayer CrI_3 observed in experiment.

These selection rules are relaxed for acoustic magnon scattering in bulk CrI_3 (Fig. 5.5a). While the magnon scattering is still predominately in the cross-circular channels, we observe significant scattering in the co-circular channels. This deviation from the expected selection rules

could potentially originate from stacking faults in the bulk and highlights the intriguing physics afforded by studying atomically thin samples with pristine crystal structures.

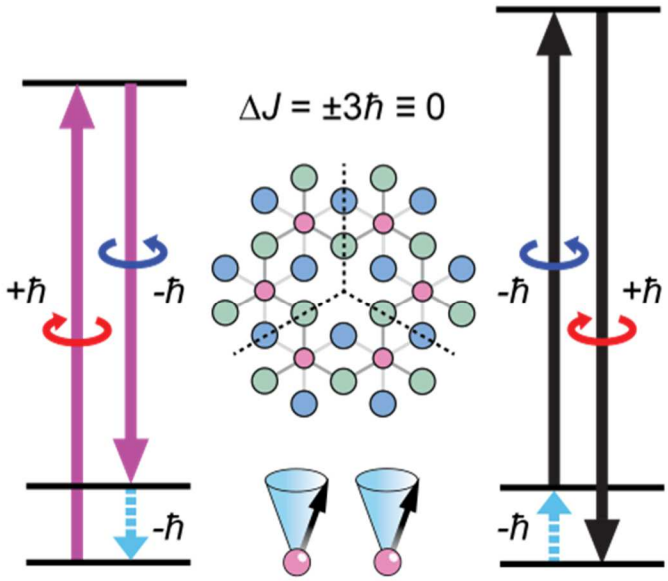

Figure 5.7. Optical selection rules of one-magnon scattering in monolayer CrI_3. The left (right) energy diagram illustrates Stokes (anti-Stokes) scattering in the spin-up state. While the total change in angular momentum, ΔJ is $\pm 3\hbar$, this is equivalent to $\Delta J = 0$ in a honeycomb lattice shown in the middle of the figure. Pink, green, and blue circles in the honeycomb lattice represent Cr^{3+}, top I^-, and bottom I^- ions respectively. The pink spheres in the bottom of the figure are the Cr^{3+} sites in a unit cell. Their spins are denoted as black arrows and the trace of their in-phase oscillatory motion as blue cones. Reproduced from ref. [137].

5.4 Antiferromagnetic magnon modes and optical magnons in bilayer CrI_3

Unlike the monolayer, bilayer CrI_3 hosts layered antiferromagnetic states below a critical temperature of 45 K which can be switched to a ferromagnetic-like state upon the application of a magnetic field. The crystal lattice of bilayer CrI_3 also does not possess threefold rotational symmetry. This provides opportunities to study the effects of antiferromagnetic interlayer coupling

on the magnon spectrum, as well as probe for changes in the selection rules in the ferromagnetic-like state.

Figure 5.8a shows the low-frequency Raman spectrum of a CrI_3 bilayer in an applied field of 6 T. Since the magnetization of both layers are aligned in the same direction by the magnetic field, the bilayer essentially behaves like a ferromagnetic monolayer. That is, the acoustic magnon mode is cross-circularly polarized with the Stokes and anti-Stokes peaks showing opposite selection rules and shifts linearly in energy with a *g* factor of ~2.1 under applied field (Fig. 5.8b). However, in contrast to the monolayer, we observe switching of acoustic magnon modes as the bilayer undergoes a spin-flip transition between -0.7 T and -0.75 T, consistent with the spin-flip field observed in RMCD. Figure 5.8c shows a series of Raman spectra as the magnetic states switch from the AFM to the FM-like state. Since the shift of the magnon peak over small field ranges near the spin-flip transition is smaller than the resolution of our spectrometer, we utilize Lorentzian fits to track subtle changes in the magnon energy as illustrated in Fig. AIV.2. In the AFM state, at fields close to the spin-flip transition, the acoustic magnon mode has a frequency of ~3.6 cm^{-1}. As the field passes the spin-flip transition, the magnon mode at 3.6 cm^{-1} vanishes. Instead, another acoustic mode, starting at a lower frequency of ~3.0 cm^{-1}, appears and linearly shifts to higher energy as the magnitude of the field increases.

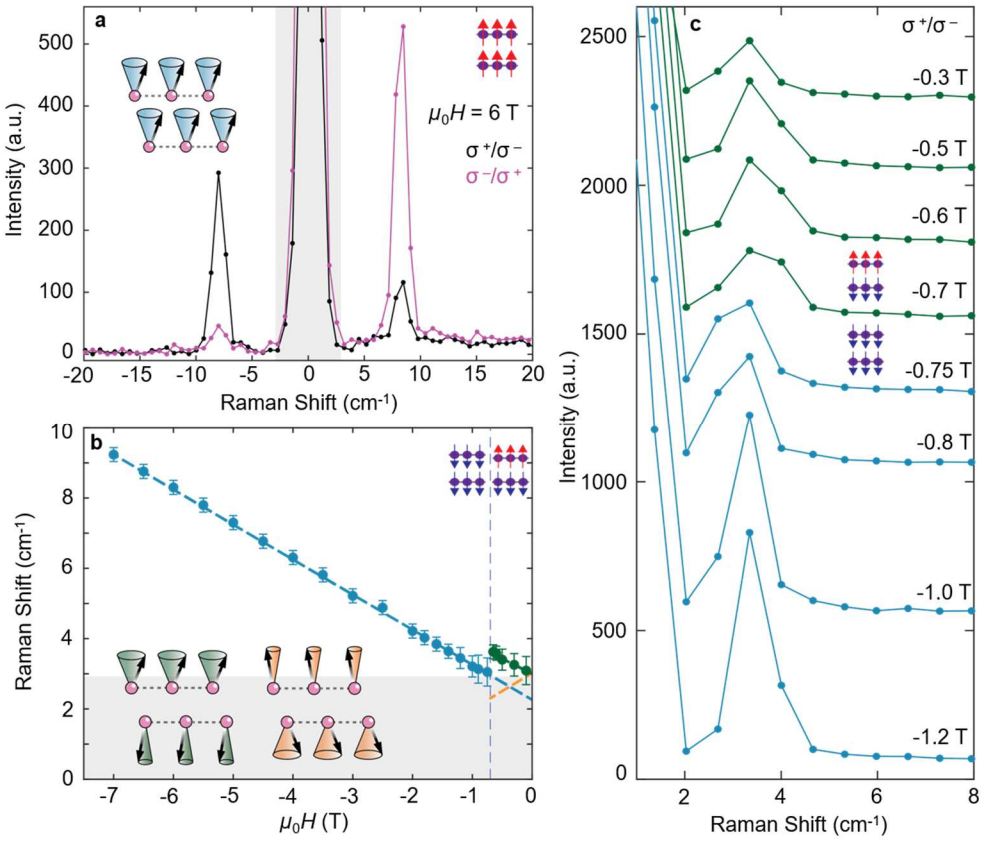

Figure 5.8. Magnon scattering in magnetic CrI_3 bilayers. (a) Low-frequency Raman spectrum of a CrI_3 bilayer in the spin-up FM-like state at an applied field of 6 T. (b) The magnon frequency in the field range from -7 T to 0 T. The dashed blue line is a linear fit of the acoustic magnon energy indicating a Zeeman shift of g factor ~ 2.1 and intercept of 2.2 cm^{-1} (0.27 meV). Between -0.7 T and -0.75 T, a metamagnetic transition indicated by the grey dashed line occurs as the bilayer switches to the layered AFM state which should host two magnon modes that shift oppositely with applied field. These two magnon modes are illustrated in the bottom-left inset. The green dashed line plots the mode which blueshifts (left cartoon of inset) and is resolvable in our experiments while the orange dashed line indicates the mode which redshifts (right cartoon of inset) into the spectral filter which is indicated by the grey box. The intercept of the green line indicates that the zero-field AFM magnon energy is ~ 3 cm^{-1} (0.37 meV). The error bars represent the uncertainty of the Lorentzian fit used to determine the magnon energy. (c) Low-frequency Raman spectra taken as the bilayer goes through the transition with increasing magnetic field strength. The switching of the acoustic magnon modes is evident as the peak centered at ~3.6 cm^{-1} (0.44 meV) at -0.7 T disappears, and a lower energy mode emerges. Reproduced from ref. [137].

The zero-field magnon energy of the antiferromagnetic acoustic magnon mode, which we find to be ~0.37 meV from a linear fit (green line in Fig. 5.8b), is given by $\sqrt{(2J_{\text{inter}} + K)K}$, where J_{inter} is the antiferromagnetic interlayer exchange interaction, and K is the magnetic anisotropy[147]. We can extract the magnetic anisotropy by extrapolating the linear fit (blue line, Fig. 5.8b) of the acoustic magnon energy shift in the FM-like state to zero field. Doing so results in K ~ 0.27 meV which allows us to find J_{inter} ~ 0.11 meV. Therefore, bilayer CrI_3 is in the weak exchange limit ($K > J_{\text{inter}}$) as opposed to the weak anisotropy limit ($J_{\text{inter}} \gg K$). As the magnetic field increases, instead of a spin-flop transition, bilayer CrI_3 undergoes an abrupt spin-flip transition[34,62], explaining the observed discontinuity of the magnon frequency at the spin-flip field. The weak interlayer exchange J_{inter} also explains why the cross-circular optical selection rules continue to hold for bilayer CrI_3 even though the crystal structure lacks three-fold rotational symmetry due to its monoclinic stacking[58–61,63–65].

In addition to the low-frequency acoustic magnons, we also resolve a high-frequency cross-polarized mode in bilayers which has not been observed in previous Raman studies on CrI_3[57,64–66,132,136]. Figure 5.9a shows a very weak and broad peak centered at ~148 cm^{-1} (4.4 THz or 18.4 meV) at 8 T which exhibits the same helicity-dependent selection rules as the acoustic magnon mode. Magnetic field-dependent measurements show that the peak position shifts linearly with a g factor of ~2 (Fig. 5.9b). Consequently, we assign this peak as the high-frequency optical magnon (OM). This is in sharp contrast to monolayers where the optical mode is Raman silent. As illustrated in Fig. 5.10a, the optical magnon mode does not show up in monolayers because it has the form $S_A^- - S_B^-$. This excitation is thus parity-odd and Raman-silent. In bilayers, the optical modes from both layers will hybridize, leading to a Davydov-like splitting into two modes. These two optical modes are given by $S_o^- = (S_{A1}^- - S_{B1}^-) \pm (S_{A2}^- - S_{B2}^-)$, where $A1$ denotes the A site in

layer 1. It is clear that one mode is parity-odd while the other is parity-even and consequently Raman-active (Figs. 5.10b&c). This optical magnon mode is related to the intralayer exchange by $E = K + 6J_{\text{intra}}$. Therefore, we determine the intralayer exchange to be ~2.83 meV. We also observed the terahertz optical magnon in both exfoliated thin bulk (Fig. 5.11a) and unexfoliated single crystal samples (Fig. 5.11b) with frequencies of 160 cm^{-1} (4.8 THz or 19.8 meV) and 148 cm^{-1} (4.4 THz or 18.4 meV) respectively. We note that the optical magnon energy is consistent with that seen in recent neutron scattering experiments[141].

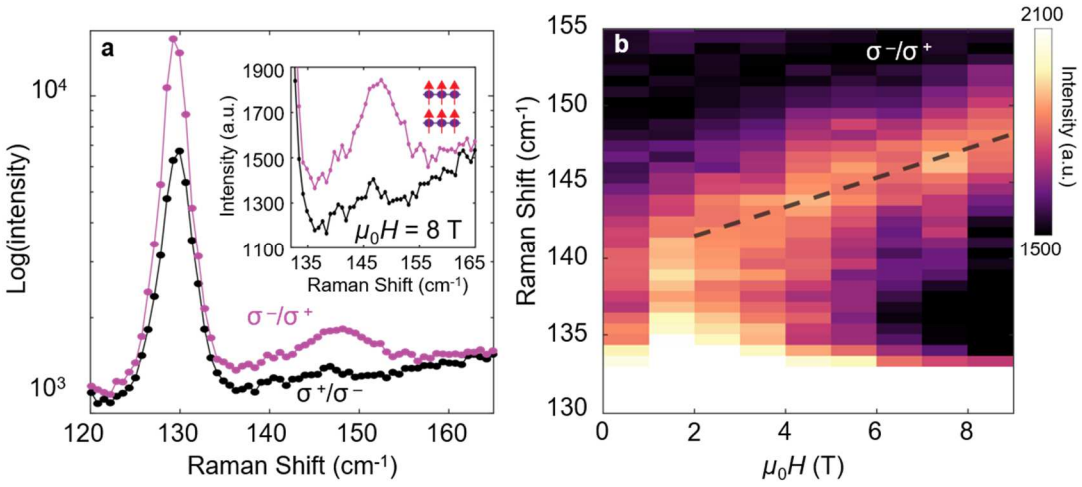

Figure 5.9. Optical magnons in bilayer CrI_3. (a) Raman scattering from bilayer CrI_3 in an applied field of 8 T with intensity plotted in a log scale. The right inset displays a zoomed in plot of a cross-polarized feature centered at ~148 cm^{-1} (4.4 THz or 18.4 meV). (b) Field dependence of the optical magnon from 0 T to 9 T. The feature shifts with a g factor ~ 2 (dashed black line), confirming its magnon nature. Reproduced from ref. [137].

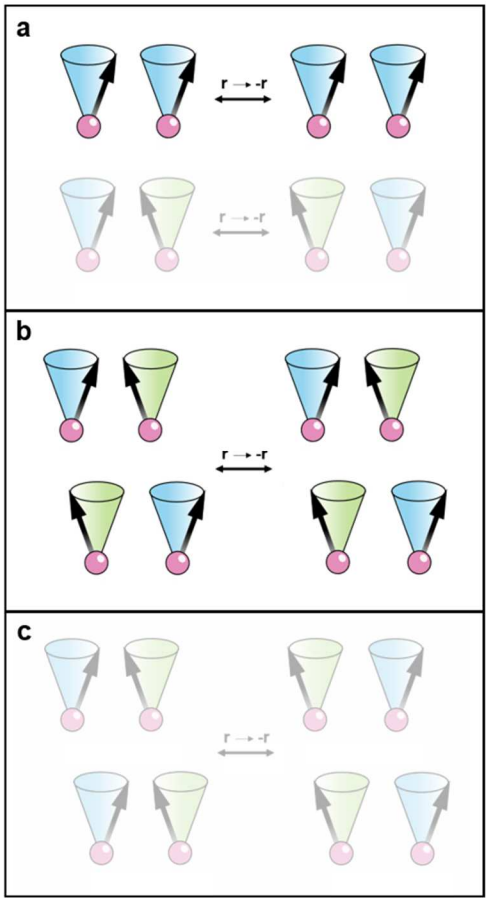

Figure 5.10. Raman selection rules for optical magnons in monolayer and bilayer CrI_3. (c) Illustration of acoustic and optical magnons in a CrI_3 monolayer unit cell. After applying the inversion operator, **-r**, the acoustic magnon remains invariant while the optical magnon accumulates a π-phase shift in its spin precession. Given that the monolayer is centrosymmetric, the parity-even acoustic magnon is Raman-active while the parity-odd optical magnon is Raman-silent. (d-e) Cartoons of optical magnons in an FM-like CrI_3 bilayer. Davydov-like splitting of the optical magnon in a monolayer results in (d) a parity-even, Raman-active mode and (e) a parity-odd, Raman-silent mode. Reproduced from ref. [137].

Unlike the low-frequency acoustic magnon which merges with Rayleigh scatter, we are able to resolve the OM mode down to zero applied field and observe its behavior in the AFM state. In stark contrast to the FM-like state, the OM mode in the AFM state can be excited by both helicities of incident light, giving equal scattering intensity in both σ^+/σ^- and σ^-/σ^+ detection

channels in the absence of applied field (Fig. 5.12a). Applying a small field of 0.5 T, however, results in an energy splitting between the OM features seen in the two cross-circular channels shown in Fig. 5.12b: the OM mode in the σ^-/σ^+ channel blueshifts while the peak in the σ^+/σ^- channel redshifts. Flipping the direction of the applied field to -0.5 T in Fig. 5.12c reverses the splitting such that the OM mode in the σ^+/σ^- (σ^-/σ^+) channel is at a higher (lower) frequency.

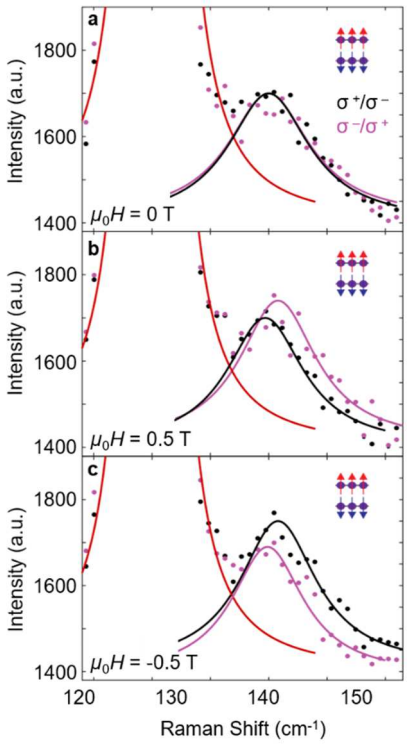

Figure 5.11. Magnetic field-dependence of antiferromagnetic optical magnons in bilayer CrI_3. (a) Zero-field Raman spectra of bilayer CrI_3. The solid lines are Lorentzian functions plotted as guides-to-the-eye. Contrary to the FM-like state which shows a strong favoring of one cross-circular scattering channel, the optical magnon in the zero-field AFM state appears equally in both σ^+/σ^- and σ^-/σ^+. (b) Upon application of magnetic field, there is a splitting between the two optical magnon modes as the σ^-/σ^+ mode blue-shifts and σ^+/σ^- mode red-shifts. (c) When the direction of applied field is flipped, the energy shift of the modes is also reversed. Reproduced from ref. [137].

In general, antiferromagnets with easy axis anisotropy, such as bilayer CrI_3, host two magnon modes per branch which are degenerate at zero-field but carry opposite angular

momentum[147,148]. The layered antiferromagnetic order breaks inversion symmetry, eliminating the parity criterion and hence allowing Raman activity of both optical magnon modes. Upon the application of a magnetic field, the two modes shift oppositely, *i.e.* one mode will blueshift and the other will redshift. This explains the Raman activity of the optical branch magnons in both cross-circular channels and the opposite energy splitting of the two OM modes in Figs. 5.12b&c. The acoustic branch magnons also split in an applied magnetic field, but the redshifted magnon mode (denoted by the orange line in Fig. 5.8b) is overshadowed by Rayleigh scatter, making it unresolvable in our measurements.

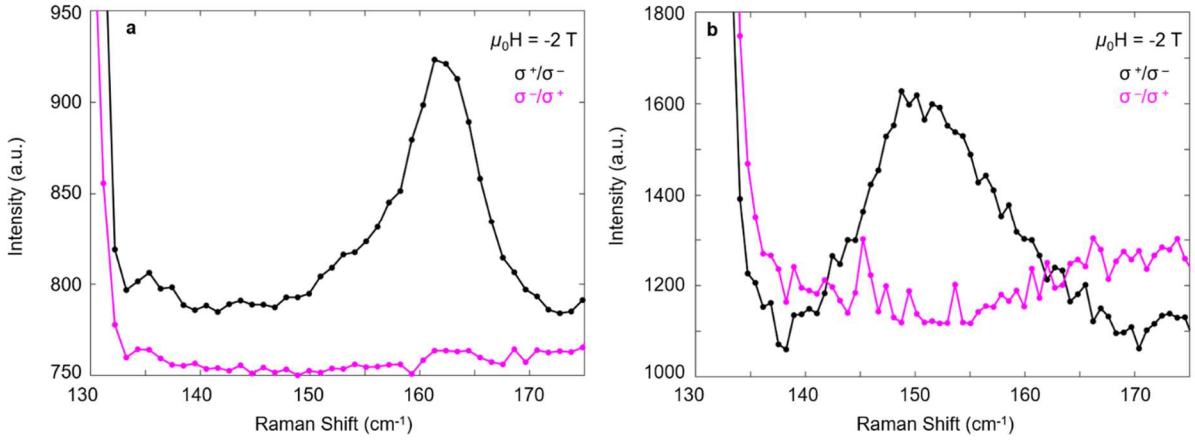

Figure 5.12. Optical magnons in bulk CrI_3. (a) Cross-circularly polarized scattering channels in exfoliated thin bulk (~100 nm thickness) showing the optical magnon at an applied field of -2 T. In this sample, the magnon appears at a higher frequency than in bilayer with a zero-field energy of ~160 cm^{-1} (4.8 THz). (b) Optical magnon in unexfoliated single-crystal CrI_3 in an applied field of -2 T. In this thickness, the optical magnon appears at a zero-field frequency of ~148 cm^{-1}, higher than that of bilayer but lower than exfoliated thin bulk. Reproduced from ref. [137].

5.5 Remarks and Future Directions

In this chapter, we have identified acoustic and optical magnons in atomically thin CrI_3 which obey selection rules dictated by discrete angular momentum conservation in a honeycomb lattice. Using the energies of the acoustic magnons, we calculate the strength of anisotropy and interlayer

exchange. The optical magnon, on the other hand, allows for the determination of intralayer exchange. A group at Cornell experimentally confirmed the acoustic magnon mode through ultrafast pump-probe measurements[149] but were unable to identify the optical magnon mode.

In contrast to the low-frequency acoustic magnons and those observed in standard FM spintronic systems, the frequency of the optical magnon is well into the terahertz regime and is comparable to those found in AFM systems[150]. As CrI_3 is an insulator, the lifetime of terahertz magnons may be much longer than those in metallic systems[151,152]. Indeed, we determine that the lifetime is on the order of picoseconds, an order of magnitude longer than those seen in recent high-quality metallic FM thin films[152,153], and could be useful for vdW magnonic devices in the terahertz regime.

While the optical magnon mode was found through Raman scattering in bilayer CrI_3, it was not detected in monolayer CrI_3 due to symmetry constraints. Therefore, an alternative experimental approach is needed to detect these THz spin waves in the monolayer limit. One possibility could be through infrared spectroscopy. Due to its parity, a direct optical transition via one-photon absorption could couple to the optical magnon transition which would be detected as a change in the intensity of infrared light at the optical magnon energy. Another method would be to interface monolayer CrI_3 with the monolayer semiconducting MX_2 (M = W, Mo; X = S, Se) to couple the optical magnon to the K valley excitons. This has been demonstrated in $MnPSe_3$-$MoSe_2$ heterostructures where the magnons in the $MnPSe_3$ lead to an energy shift of the K valley excitons through exchange interactions between the two[154].

BIBLIOGRAPHY

1. Reyren, N. *et al.* Superconducting Interfaces Between Insulating Oxides. *Science* **317**, 1196–1199 (2007).
2. König, M., Molenkamp, L. W., Qi, X. & Zhang, S. Quantum Spin Hall Insulator State in HgTe Quantum Wells. *Science* **318**, 766–771 (2007).
3. Bert, J. A. *et al.* Direct imaging of the coexistence of ferromagnetism and superconductivity at the $LaAlO_3/SrTiO_3$ interface. *Nat. Phys.* **7**, 767–771 (2011).
4. Caviglia, A. D. *et al.* Electric field control of the $LaAlO_3/SrTiO_3$ interface ground state. *Nature* **456**, 624–627 (2008).
5. Bernevig, B. A., Hughes, T. L. & Zhang, S.-C. Quantum Spin Hall Effect and Topological Phase Transition in HgTe Quantum Wells. *Science* 1757–1762 (2006).
6. Novoselov, K. S. *et al.* Electric Field Effect in Atomically Thin Carbon Films. *Science* **306**, 666–669 (2004).
7. Du, X., Skachko, I., Barker, A. & Andrei, E. Y. Approaching ballistic transport in suspended graphene. *Nat. Nanotechnol.* **3**, 491–495 (2008).
8. Bolotin, K. I. *et al.* Ultrahigh electron mobility in suspended graphene. *Solid State Commun.* **146**, 351–355 (2008).
9. Bolotin, K. I., Ghahari, F., Shulman, M. D., Stormer, H. L. & Kim, P. Observation of the fractional quantum Hall effect in graphene. *Nature* **462**, 196–199 (2009).
10. Xu, X., Yao, W., Xiao, D. & Heinz, T. F. Spin and pseudospin in layered transition metal dichalcogenides. *Nat. Phys.* **10**, 343–350 (2014).
11. Wu, S. *et al.* Observation of the quantum spin Hall effect up to 100 kelvin in a monolayer crystal. *Science* **359**, 76–79 (2018).
12. Fei, Z. *et al.* Edge conduction in monolayer WTe_2. *Nat. Phys.* **13**, 677–682 (2017).
13. Geim, A. K. & Grigorieva, I. V. Van der Waals heterostructures. *Nature* **499**, 419–425 (2013).
14. Novoselov, K. S., Mishchenko, A., Carvalho, A. & Castro Neto, A. H. 2D materials and van der Waals heterostructures. *Science* **353**, aac9439 (2016).
15. Baugher, B. W. H., Churchill, H. O. H., Yang, Y. & Jarillo-Herrero, P. Optoelectronic devices based on electrically tunable p-n diodes in a monolayer dichalcogenide. *Nat.*

Nanotechnol. **9**, 262–267 (2014).

16. Ross, J. S. *et al.* Electrically tunable excitonic light-emitting diodes based on monolayer WSe_2 p-n junctions. *Nat. Nanotechnol.* **9**, 268–272 (2014).
17. Cheng, R. *et al.* Electroluminescence and photocurrent generation from atomically sharp WSe_2/MoS_2 heterojunction p-n diodes. *Nano Lett.* **14**, 5590–5597 (2014).
18. Cao, Y. *et al.* Unconventional superconductivity in magic-angle graphene superlattices. *Nature* **556**, 43–50 (2018).
19. Seyler, K. L. *et al.* Signatures of moiré-trapped valley excitons in $MoSe_2/WSe_2$ heterobilayers. *Nature* **567**, 66–70 (2019).
20. Jin, C. *et al.* Observation of moiré excitons in WSe_2/WS_2 heterostructure superlattices. *Nature* **567**, 76–80 (2019).
21. Tran, K. *et al.* Evidence for moiré excitons in van der Waals heterostructures. *Nature* **567**, 71–75 (2019).
22. Alexeev, E. M. *et al.* Resonantly hybridized excitons in moiré superlattices in van der Waals heterostructures. *Nature* **567**, 81–86 (2019).
23. Mermin, N. D. & Wagner, H. Absence of ferromagnetism or antiferromagnetism in one- or two-dimensional isotropic Heisenberg models. *Phys. Rev. Lett.* **17**, 1133–1136 (1966).
24. Onsager, L. Crystal Statistics. I. A Two-Dimensional Model with an Order-Disorder Transition. *Phys. Rev.* **65**, 117–149 (1949).
25. Zhang, W. B., Qu, Q., Zhu, P. & Lam, C. H. Robust intrinsic ferromagnetism and half semiconductivity in stable two-dimensional single-layer chromium trihalides. *J. Mater. Chem. C* **3**, 12457–12468 (2015).
26. Lin, M. W. *et al.* Ultrathin nanosheets of $CrSiTe_3$: A semiconducting two-dimensional ferromagnetic material. *J. Mater. Chem. C* **4**, 315–322 (2016).
27. Li, X. & Yang, J. $CrXTe_3$ (X = Si, Ge) nanosheets: Two dimensional intrinsic ferromagnetic semiconductors. *J. Mater. Chem. C* **2**, 7071–7076 (2014).
28. Tongay, S., Varnoosfaderani, S. S., Appleton, B. R., Wu, J. & Hebard, A. F. Magnetic properties of MoS_2: Existence of ferromagnetism. *Appl. Phys. Lett.* 123105 (2012).
29. Sachs, B., Wehling, T. O., Novoselov, K. S., Lichtenstein, A. I. & Katsnelson, M. I. Ferromagnetic two-dimensional crystals: Single layers of K_2CuF_4. *Phys. Rev. B - Condens. Matter Mater. Phys.* **88**, 201402 (2013).

30. Wang, X. *et al.* Raman spectroscopy of atomically thin two-dimensional magnetic iron phosphorus trisulfide (FePS3) crystals. *2D Mater.* **3**, 031009 (2016).
31. Tian, Y., Gray, M. J., Ji, H., Cava, R. J. & Burch, K. S. Magneto-elastic coupling in a potential ferromagnetic 2D atomic crystal. *2D Mater.* **3**, 025035 (2016).
32. Dillon, J. F., Kamimura, H. & Remeika, J. P. Magneto-optical properties of ferromagnetic chromium trihalides. *J. Phys. Chem. Solids* **27**, 1531–1549 (1966).
33. Dillon, J. F. & Olson, C. E. Magnetization, resonance, and optical properties of the ferromagnet CrI_3. *J. Appl. Phys.* **36**, 1259–1260 (1965).
34. Huang, B. *et al.* Layer-dependent Ferromagnetism in a van der Waals Crystal down to the Monolayer Limit. *Nature* **546**, 270–273 (2017).
35. McGuire, M. A., Dixit, H., Cooper, V. R. & Sales, B. C. Coupling of crystal structure and magnetism in the layered, ferromagnetic insulator CrI_3. *Chem. Mater.* **27**, 612–620 (2015).
36. Wang, H., Eyert, V. & Schwingenschlögl, U. Electronic structure and magnetic ordering of the semiconducting chromium trihalides $CrCl_3$, $CrBr_3$, and CrI_3. *J. Phys. Condens. Matter* **23**, 116003 (2011).
37. Wang, H., Fan, F., Zhu, S. & Wu, H. Doping enhanced ferromagnetism and induced half-metallicity in CrI_3 monolayer. *Europhys. Lett.* **114**, 47001 (2016).
38. Huang, B. *et al.* Emergent Phenomena and Proximity Effects in 2D Magnets and Heterostructures. *Nat. Mater.* accepted (2020).
39. Kanamori, J. Superexchange interaction and symmetry properties of electron orbitals. *J. Phys. Chem. Solids* **10**, 87–98 (1959).
40. Goodenough, J. B. Theory of the Role of Covalence in the Perovskite-Type Manganites [La,M(II)]MnO_3. *Phys. Rev.* **100**, 564–573 (1955).
41. Geertsma, W. & Khomskii, D. Influence of side groups on 90° superexchange: A modification of the Goodenough-Kanamori-Anderson rules. *Phys. Rev. B - Condens. Matter Mater. Phys.* **54**, 3011–3014 (1996).
42. Lado, J. L. & Fernández-Rossier, J. On the origin of magnetic anisotropy in two dimensional CrI_3. *2D Mater.* **4**, 035002 (2017).
43. Bené, R. W. Electron-paramagnetic-resonance study of Cr ions and exchange-coupled Cr ion pairs in the BiI_3 structure. *Phys. Rev.* **178**, 497–513 (1969).
44. Abramchuk, M. *et al.* Controlling Magnetic and Optical Properties of the van der Waals

Crystal $CrCl_{3-x}Br_x$ via Mixed Halide Chemistry. *Adv. Mater.* **30**, 1801325 (2018).

45. Blake, P. *et al.* Making graphene visible. *Appl. Phys. Lett.* **91**, 063124 (2007).
46. Grant, P. M. & Bryan Street, G. Optical properties of chromium trihalides in the region 1-11 eV. in *Bulletin of the American Physical Society* 415 (1968).
47. Mak, K. F., Lee, C., Hone, J., Shan, J. & Heinz, T. F. Atomically thin MoS_2: A new direct-gap semiconductor. *Phys. Rev. Lett.* **105**, 136805 (2010).
48. Shcherbakov, D. *et al.* Raman Spectroscopy, Photocatalytic Degradation, and Stabilization of Atomically Thin Chromium Tri-iodide. *Nano Lett.* **18**, 4214–4219 (2018).
49. Vaz, C. A. F., Bland, J. A. C. & Lauhoff, G. Magnetism in ultrathin film structures. *Reports Prog. Phys.* **71**, 056501 (2008).
50. Huang, F., Kief, M. T., Mankey, G. J. & Willis, R. F. Magnetism in the few-monolayers limit: A surface magneto-optic Kerr-effect study of the magnetic behavior of ultrathin films of Co, Ni, and Co-Ni alloys on Cu(100) and Cu(111). *Phys. Rev. B* **49**, 3962–3971 (1994).
51. Nagaosa, N., Sinova, J., Onoda, S., MacDonald, A. H. & Ong, N. P. Anomalous Hall effect. *Rev. Mod. Phys.* **82**, 1539–1592 (2010).
52. Wang, Z. *et al.* Very large tunneling magnetoresistance in layered magnetic semiconductor CrI_3. *Nat. Commun.* **9**, 2516 (2018).
53. Ebert, H. Magneto-optical effects in transition metal systems. *Reports Prog. Phys.* **59**, 1665–1735 (1996).
54. Buchmeier, M., Schreiber, R., Bürgler, D. E. & Schneider, C. M. Thickness dependence of linear and quadratic magneto-optical Kerr effects in ultrathin Fe(001) films. *Phys. Rev. B - Condens. Matter Mater. Phys.* **79**, 064402 (2009).
55. Sato, K. Measurement of magneto-optical Kerr effect using piezo-birefringent modulator. *Jpn. J. Appl. Phys.* **20**, 2403–2409 (1981).
56. Višňovský, Š. *et al.* Magneto-optical Kerr spectra of nickel. *Journal of Magnetism and Magnetic Materials* **127**, 135–139 (1993).
57. Huang, B. *et al.* Tuning inelastic light scattering via symmetry control in the two-dimensional magnet CrI_3. *Nat. Nanotechnol.* **15**, 212–216 (2020).
58. Sivadas, N., Okamoto, S., Xu, X., Fennie, C. J. & Xiao, D. Stacking-Dependent Magnetism in Bilayer CrI_3. *Nano Lett.* **18**, 7658–7664 (2018).

59. Jiang, P. *et al.* Stacking tunable interlayer magnetism in bilayer CrI_3. *Phys. Rev. B* **99**, 144401 (2019).

60. Jang, S. W., Jeong, M. Y., Yoon, H., Ryee, S. & Han, M. J. Microscopic understanding of magnetic interactions in bilayer CrI_3. *Phys. Rev. Mater.* **3**, 031001 (2019).

61. Soriano, D., Cardoso, C. & Fernández-Rossier, J. Interplay between interlayer exchange and stacking in CrI_3 bilayers. *Solid State Commun.* **299**, 113662 (2019).

62. Song, T. *et al.* Giant tunneling magnetoresistance in spin-filter van der Waals heterostructures. *Science* **360**, 1214–1218 (2018).

63. Sun, Z. *et al.* Giant nonreciprocal second-harmonic generation from antiferromagnetic bilayer CrI_3. *Nature* **572**, 497–501 (2019).

64. Song, T. *et al.* Switching 2D magnetic states via pressure tuning of layer stacking. *Nat. Mater.* **18**, 1298–1302 (2019).

65. Li, T. *et al.* Pressure-controlled interlayer magnetism in atomically thin CrI_3. *Nat. Mater.* **18**, 1303–1308 (2019).

66. Ubrig, N. *et al.* Low-temperature monoclinic layer stacking in atomically thin CrI_3 crystals. *2D Mater.* **7**, 015007 (2020).

67. Klein, D. R. *et al.* Enhancement of interlayer exchange in an ultrathin two-dimensional magnet. *Nat. Phys.* **15**, 1255–1260 (2019).

68. Wang, Z. *et al.* Determining the phase diagram of atomically thin layered antiferromagnet $CrCl_3$. *Nat. Nanotechnol.* **14**, 1116–1122 (2019).

69. Chen, W. *et al.* Direct observation of van der Waals stacking-dependent interlayer magnetism. *Science* **366**, 983–987 (2019).

70. Burch, K. S., Mandrus, D. & Park, J. G. Magnetism in two-dimensional van der Waals materials. *Nature* **563**, 47–52 (2018).

71. Gibertini, M., Koperski, M., Morpurgo, A. F. & Novoselov, K. S. Magnetic 2D materials and heterostructures. *Nat. Nanotechnol.* **14**, 408–419 (2019).

72. Gong, C. & Zhang, X. Two-dimensional magnetic crystals and emergent heterostructure devices. *Science* **363**, eaav4450 (2019).

73. Sivadas, N., Daniels, M. W., Swendsen, R. H., Okamoto, S. & Xiao, D. Magnetic ground state of semiconducting transition-metal trichalcogenide monolayers. *Phys. Rev. B* **91**, 235425 (2015).

74. Norden, T. *et al.* Giant Valley Splitting in Monolayer WS_2 by Magnetic Proximity Effect. *Nat. Commun.* **10**, 4163 (2019).

75. Kim, M. *et al.* Hall micromagnetometry of individual two-dimensional ferromagnets. *Nat. Electron.* **2**, 457–463 (2019).

76. Alghamdi, M. *et al.* Highly Efficient Spin-Orbit Torque and Switching of Layered Ferromagnet Fe_3GeTe_2. *Nano Lett.* **19**, 4400–4405 (2019).

77. Ostwal, V., Shen, T. & Appenzeller, J. Efficient Spin-Orbit Torque Switching of the Semiconducting Van Der Waals Ferromagnet $Cr_2Ge_2Te_6$. *Adv. Mater.* **32**, 1906021 (2020).

78. Zhong, D. *et al.* Van der Waals Engineering of Ferromagnetic Semiconductor Heterostructures for Spin and Valleytronics. *Sci. Adv.* **3**, e1603113 (2017).

79. Seyler, K. L. *et al.* Valley Manipulation by Optically Tuning the Magnetic Proximity Effect in WSe_2/CrI_3 Heterostructures. *Nano Lett.* **18**, 3823–3828 (2018).

80. Otrokov, M. M. *et al.* Prediction and observation of an antiferromagnetic topological insulator. *Nature* **576**, 416–422 (2019).

81. Liu, C. *et al.* Quantum phase transition from axion insulator to Chern insulator in $MnBi_2Te_4$. *Nat. Mater.* **19**, 522–527 (2020).

82. Gong, C. *et al.* Discovery of intrinsic ferromagnetism in two-dimensional van der Waals crystals. *Nature* **546**, 265–269 (2017).

83. Lee, J. U. *et al.* Ising-Type Magnetic Ordering in Atomically Thin $FePS_3$. *Nano Lett.* **16**, 7433–7438 (2016).

84. McCreary, A. *et al.* Quasi-two-dimensional magnon identification in antiferromagnetic $FePS_3$ via magneto-Raman Spectroscopy. *Phys. Rev. B* **101**, 064416 (2020).

85. Deng, Y. *et al.* Quantum anomalous Hall effect in intrinsic magnetic topological insulator $MnBi_2Te_4$. *Science* **367**, 895–900 (2020).

86. Otrokov, M. M. *et al.* Prediction and observation of the first antiferromagnetic topological insulator. *Nature* **576**, (2018).

87. Cai, X. *et al.* Atomically Thin $CrCl_3$: An In-Plane Layered Antiferromagnetic Insulator. *Nano Lett.* **19**, 3993–3998 (2019).

88. O'Hara, D. J. *et al.* Room Temperature Intrinsic Ferromagnetism in Epitaxial Manganese Selenide Films in the Monolayer Limit. *Nano Lett.* **18**, 3125–3131 (2018).

89. Wu, Z., Yu, J. & Yuan, S. Strain-tunable magnetic and electronic properties of monolayer CrI_3. *Phys. Chem. Chem. Phys.* **21**, 7750–7755 (2019).

90. Mukherjee, T., Chowdhury, S., Jana, D. & Voon, L. C. L. Y. Strain induced electronic and magnetic properties of 2D magnet CrI_3: A DFT approach. *J. Phys. Condens. Matter* **31**, 335802 (2019).

91. Ni, Z. H. *et al.* Uniaxial strain on graphene: Raman spectroscopy study and band-gap opening. *ACS Nano* **2**, 2301–2305 (2008).

92. Wu, W. *et al.* Giant Mechano-Optoelectronic Effect in an Atomically Thin Semiconductor. *Nano Lett.* **18**, 2351–2357 (2018).

93. Chu, J. H., Kuo, H.-H., Analytis, J. G. & Fisher, I. R. Divergent nematic susceptibility in an iron arsenide superconductor. *Science* **338**, 469 (2012).

94. Bunch, J. S. *et al.* Electromechanical Resonators from Graphene Sheets. *Science* **315**, 490–494 (2007).

95. Jiang, S., Xie, H., Shan, J. & Mak, K. F. Two-dimensional magnetic nanoelectromechanical resonators. Preprint at: https://arXiv.org/abs/2001.03153

96. Nayak, A. P. *et al.* Pressure-induced semiconducting to metallic transition in multilayered molybdenum disulphide. *Nat. Commun.* **5**, 3731 (2014).

97. Wolf, S. A. *et al.* Spintronics: A spin-based electronics vision for the future. *Science* **294**, 1488–1495 (2001).

98. Huang, B. *et al.* Electrical control of 2D magnetism in bilayer CrI_3. *Nat. Nanotechnol.* **13**, 544–548 (2018).

99. Manchon, A., Koo, H. C., Nitta, J., Frolov, S. M. & Duine, R. A. New perspectives for Rashba spin-orbit coupling. *Nat. Mater.* **14**, 871–882 (2015).

100. Ohno, H., Chiba D., Matsukura, F., Omiya, T., Abe, E., Dietl, T., Ohno, Y., Ohtani, K. Electric-field control of ferromagnetism. *Nature* **408**, 944–946 (2000).

101. MacDonald, A. H., Schiffer, P. & Samarth, N. Ferromagnetic semiconductors: moving beyond (Ga,Mn)As. *Nat. Mater.* **4**, 195–202 (2005).

102. Weisheit, M. *et al.* Electric field-induced modification of magnetism in thin-film ferromagnets. *Science* **315**, 349–351 (2007).

103. Dean, C. R. *et al.* Boron nitride substrates for high-quality graphene electronics. *Nat. Nanotechnol.* **5**, 722–726 (2010).

104. Jiang, S., Shan, J. & Mak, K. F. Electric-field switching of two-dimensional van der Waals magnets. *Nat. Mater.* **17**, 406–410 (2018).

105. Ye, J. T. *et al.* Superconducting dome in a gate-tuned band insulator. *Science* **338**, 1193–1196 (2012).

106. Castellanos-Gomez, A. *et al.* Deterministic transfer of two-dimensional materials by all-dry viscoelastic stamping. *2D Mater.* **1**, 011002 (2014).

107. Jiang, S., Li, L., Wang, Z., Mak, K. F. & Shan, J. Controlling magnetism in 2D CrI_3 by electrostatic doping. *Nat. Nanotechnol.* **13**, 549–553 (2018).

108. Laturia, A., Van de Put, M. L. & Vandenberghe, W. G. Dielectric properties of hexagonal boron nitride and transition metal dichalcogenides: from monolayer to bulk. *npj 2D Mater. Appl.* **2**, 6 (2018).

109. Duan, C. G. *et al.* Surface magnetoelectric effect in ferromagnetic metal films. *Phys. Rev. Lett.* **101**, 137201 (2008).

110. Nakamura, K. *et al.* Giant modification of the magnetocrystalline anisotropy in transition-metal monolayers by an external electric field. *Phys. Rev. Lett.* **102**, 187201 (2009).

111. Schmehl, A. *et al.* Epitaxial integration of the highly spin-polarized ferromagnetic semiconductor EuO with silicon and GaN. *Nat. Mater.* **6**, 882–887 (2007).

112. Mairoser, T. *et al.* Is there an intrinsic limit to the charge-carrier-induced increase of the curie temperature of EuO? *Phys. Rev. Lett.* **105**, 257206 (2010).

113. Sivadas, N., Okamoto, S. & Xiao, D. Gate-controllable magneto-optic Kerr effect in layered collinear antiferromagnets. *Phys. Rev. Lett.* **117**, 267203 (2016).

114. Gong, Z. *et al.* Magnetoelectric effects and valley-controlled spin quantum gates in transition metal dichalcogenide bilayers. *Nat. Commun.* **4**, 2053 (2013).

115. Jones, A. M. *et al.* Spin-layer locking effects in optical orientation of exciton spin in bilayer WSe_2. *Nat. Phys.* **10**, 130–134 (2014).

116. Taychatanapat, T., Watanabe, K., Taniguchi, T. & Jarillo-Herrero, P. Quantum Hall effect and Landau-level crossing of Dirac fermions in trilayer graphene. *Nat. Phys.* **7**, 621–625 (2011).

117. Song, T. *et al.* Voltage Control of a van der Waals Spin-Filter Magnetic Tunnel Junction. *Nano Lett.* **19**, 915–920 (2019).

118. Suárez Morell, E., León, A., Miwa, R. H. & Vargas, P. Control of magnetism in bilayer

CrI_3 by an external electric field. *2D Mater.* **6**, 025020 (2019).

119. Deng, Y. *et al.* Gate-tunable room-temperature ferromagnetism in two-dimensional Fe_3GeTe_2. *Nature* **563**, 94–99 (2018).
120. Weber, D., Trout, A. H., McComb, D. W. & Goldberger, J. E. Decomposition-Induced Room-Temperature Magnetism of the Na-Intercalated Layered Ferromagnet $Fe_{3-x}GeTe_2$. *Nano Lett.* **19**, 5031–5035 (2019).
121. Nogués, J. *et al.* Exchange bias in nanostructures. *Physics Reports* **422**, 65–117 (2005).
122. Tombler, T. W., Zhou, C., Kong, J. & Dai, H. Gating individual nanotubes and crosses with scanning probes. *Appl. Phys. Lett.* **76**, 2412–2414 (2000).
123. Seyler, K. L. *et al.* Ligand-field helical luminescence in a 2D ferromagnetic insulator. *Nat. Phys.* **14**, 277–281 (2018).
124. Zhang, Z. *et al.* Direct Photoluminescence Probing of Ferromagnetism in Monolayer Two-Dimensional $CrBr_3$. *Nano Lett.* **19**, 3138–3142 (2019).
125. Baroni, S., de Gironcoli, S. & Dal Corso, A. Phonons and related crystal properties from density-functional perturbation theory. *Rev. Mod. Phys.* **73**, 516–562 (2001).
126. Dresselhaus, M. S. *Applications of Group Theory to the Physics of Solids*. (2002).
127. Tinkham, M. *Group Theory and Quantum Mechanics*. *Physics Bulletin* **26**, (1964).
128. Webster, L., Liang, L. & Yan, J. A. Distinct spin-lattice and spin-phonon interactions in monolayer magnetic CrI_3. *Phys. Chem. Chem. Phys.* **20**, 23546–23555 (2018).
129. Larson, D. T. & Kaxiras, E. Raman spectrum of CrI_3: An ab initio study. *Phys. Rev. B* **98**, 085406 (2018).
130. Raman, C. V. A New Radiation. *Indian J. Phys.* **2**, 387 (1927).
131. Long, D. A. *Raman spectroscopy*. (1977).
132. Jin, W. *et al.* Raman fingerprint of two terahertz spin wave branches in a two-dimensional honeycomb Ising ferromagnet. *Nat. Commun.* **9**, (2018).
133. Verble, J. L. & Wieting, T. J. Lattice mode degeneracy in MoS_2 and other layer compounds. *Phys. Rev. Lett.* **25**, 362–365 (1970).
134. Song, Q. J. *et al.* Physical origin of Davydov splitting and resonant Raman spectroscopy of Davydov components in multilayer $MoTe_2$. *Phys. Rev. B* **93**, 115409 (2016).
135. Sun, Z. *et al.* Giant and nonreciprocal second harmonic generation from layered antiferromagnetism in bilayer CrI_3. *Nature* **572**, 497–501 (2019).

136. Zhang, Y. *et al.* Magnetic Order-Induced Polarization Anomaly of Raman Scattering in 2D Magnet CrI_3. *Nano Lett.* **20**, 729–734 (2020).

137. Cenker, J. *et al.* Observation of 2D magnons in atomically thin CrI_3. *Nat. Phys.* accepted (2020).

138. Gilbert, T. L. A phenomenological theory of damping in ferromagnetic materials. *IEEE Trans. Magn.* **40**, 3443–3449 (2004).

139. Landau, L. & Lifshitz, E. On the theory of the dispersion of magnetic permeability in ferromagnetic bodies. in *Perspectives in Theoretical Physics* 51–65 (1992).

140. Rhyno, B. Magnons: Spin-Waves in Magnetic Materials. 1–10

141. Chen, L. *et al.* Topological Spin Excitations in Honeycomb Ferromagnet CrI_3. *Phys. Rev. X* **8**, 041028 (2018).

142. Lee, I., Utermohlen, F. G., Weber, D. & Hammel, C. P. Fundamental Spin Interactions Underlying the Magnetic Anisotropy in the Kitaev Ferromagnet CrI_3. *Phys. Rev. Lett.* **124**, 017201 (2020).

143. Meloche, E., Cottam, M. G., Gnezdilov, V. P. & Lockwood, D. J. One-magnon inelastic light scattering in the canted antiferromagnet NiF2. *Phys. Rev. B - Condens. Matter Mater. Phys.* **81**, (2010).

144. Němec, P., Fiebig, M., Kampfrath, T. & Kimel, A. V. Antiferromagnetic opto-spintronics. *Nat. Phys.* **14**, 229–241 (2018).

145. Higuchi, T., Kanda, N., Tamaru, H. & Kuwata-Gonokami, M. Selection rules for light-induced magnetization of a crystal with threefold symmetry: The case of antiferromagnetic NiO. *Phys. Rev. Lett.* **106**, 047401 (2011).

146. Hisatomi, R. *et al.* Helicity-Changing Brillouin Light Scattering by Magnons in a Ferromagnetic Crystal. *Phys. Rev. Lett.* (2019).

147. Keffer, F. & Kittel, C. Theory of antiferromagnetic resonance. *Phys. Rev.* **85**, 329–337 (1952).

148. Cheng, R., Daniels, M. W., Zhu, J. G. & Xiao, D. Antiferromagnetic spin wave field-effect transistor. *Sci. Rep.* (2016).

149. Zhang, X. X. *et al.* Gate-tunable spin waves in antiferromagnetic atomic bilayers. *Nat. Mater.* **19**, 838–842 (2020).

150. Jungwirth, T., Marti, X., Wadley, P. & Wunderlich, J. Antiferromagnetic spintronics. *Nat.*

Nanotechnol. **11**, 231–241 (2016).

151. Zhang, Y., Chuang, T. H., Zakeri, K. & Kirschner, J. Relaxation time of terahertz magnons excited at ferromagnetic surfaces. *Phys. Rev. Lett.* **109**, 087203 (2012).
152. Qin, H. J., Zakeri, K., Ernst, A. & Kirschner, J. Temperature Dependence of Magnetic Excitations: Terahertz Magnons above the Curie Temperature. *Phys. Rev. Lett.* **118**, 127203 (2017).
153. Qin, H. J. *et al.* Long-living terahertz magnons in ultrathin metallic ferromagnets. *Nat. Commun.* **6**, 6126 (2015).
154. Onga, M. *et al.* Antiferromagnet-Semiconductor Van der Waals Heterostructures: Interlayer Interplay of Exciton with Magnetic Ordering. *Nano Lett.* **20**, 4625–4630 (2020).

APPENDIX I

Thin film interference and its effect on the Kerr signal

Linearly polarized light is an equal superposition of right-circularly and left-circularly polarized light (RCP, LCP respectively). When a phase difference accrues between the RCP and LCP components, the polarization axis of the linearly polarized light rotates. This rotation can be observed in any material that exhibits circular birefringence. In magnetic samples, such as CrI_3, this birefringence arises from a non-zero magnetization, $\boldsymbol{M}$, and is known as the magneto-optical Kerr effect (MOKE) when detected in reflection geometry. A MOKE measurement then detects changes in $\boldsymbol{M}$ by exploiting the functional dependence of the Kerr rotation on the magnetization, $\theta_K(\boldsymbol{M})$. Additional interference terms must be accounted for however, when we discuss the Kerr rotation of a thin-film material, as reflections from the material-substrate (CrI_3-SiO_2) interface will superimpose with the reflection off the magnetic sample. As such, this motivates a model that uses the Fresnel equations to calculate the reflection coefficients for RCP ($\tilde{r_+}$) and for LCP ($\tilde{r_-}$) light. The phase difference between $\tilde{r_+}$ and $\tilde{r_-}$ then, is the Kerr rotation:

$$\theta_K = \arg(\tilde{r_+}) - \arg(\tilde{r_-}).$$

To obtain the index of refraction for CrI_3 when fully spin polarized, we work in Cartesian coordinates and use a dielectric tensor of the form[53]:

$$\boldsymbol{\varepsilon} = \begin{bmatrix} \tilde{\varepsilon}_{xx} & iQM & 0 \\ -iQM & \tilde{\varepsilon}_{xx} & 0 \\ 0 & 0 & \tilde{\varepsilon}_{zz} \end{bmatrix},$$

where Q is the complex Voigt constant and M is the out-of-plane (parallel to the z-axis) component of the magnetization, which we assume is constant for all CrI_3 thicknesses when fully spin polarized. This form of the dielectric tensor for a magnetic sample is valid assuming: *i.* the crystal

exhibits at least three-fold symmetry; *ii. M* is parallel to the axis of rotation that gives rise to the three-fold symmetry; and *iii.* the axis of rotation is chosen to be in the *z*-axis. Solving for the normal modes, we get the eigenvalues:

$$\tilde{n}_{\pm} = \sqrt{\tilde{\varepsilon}_{xx} \pm QM}$$

and the eigenvectors to be:

$$\boldsymbol{D}_{\pm} = (E_x \pm iE_y)\hat{\boldsymbol{z}}$$

where, $\tilde{n}_{+}$, $\boldsymbol{D}_{+}$ denote the eigenvalue and eigenvector respectively of RCP light and $\tilde{n}_{-}$, $\boldsymbol{D}_{-}$ denote the eigenvalue and eigenvector respectively of LCP light in CrI_3. The complex dielectric component, $\tilde{\varepsilon}_{xx}$, in terms of $\tilde{n}$ is:

$$\tilde{\varepsilon}_{xx} = n^2 - \kappa^2 - 2in\kappa$$

where the value of $\tilde{\varepsilon}_{xx}$ was derived from the n and κ at ~1.96 eV modeled in Figure 2.4b. It is apparent that we should not expect θ_K to depend linearly on M and layer number. In addition, interference from reflections off the CrI_3-SiO_2 interface will give rise to a non-trivial functional form of θ_K with respect to layer thickness.

There is no determination of Q in the literature for CrI_3, so we varied Q as a complex parameter and constrained it to a small range that fit experimental θ_K values from our MOKE measurements on trilayer and bulk CrI_3, as shown in Fig. AI.1. These calculations qualitatively describe the large increase in θ_K from monolayer to trilayer, as well as the negative θ_K seen at positive $\mu_o H$ for bulk flakes[34]. However, this simple model does not incorporate layer-dependent electronic structure changes, seen in other atomically-thin van der Waals materials such as MoS_2[47], and evident in this system as a change in magnetic ground states from monolayer to bilayer.

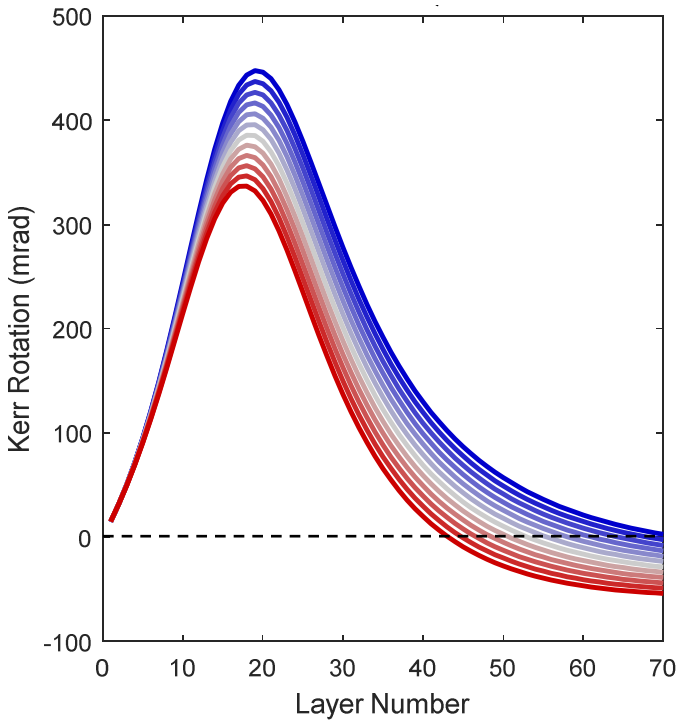

Figure AI.1. Simulated thickness-dependent Kerr signal of CrI_3 flakes on 285 nm SiO_2. The calculated evolution of the Kerr rotation is plotted as a function of layer number for a narrow range of Q (blue: 0.1+0.72i, red: 0.23+0.56i) determined by constraining the curve to fit the experimental Kerr rotation for trilayer and bulk CrI_3 (~40 nm). The black dotted line demarcates zero Kerr rotation. There is clearly a sign reversal in the Kerr signal occurring around a thickness of 40-70 layers which is qualitatively consistent with experiment. Quantitatively, however, the Kerr signal is overestimated by almost an order of magnitude in the few-layer limit.

APPENDIX II

Calculation of the magnetostatic energy of bilayer CrI_3

In this section, we calculate the magnetostatic energy of bilayer CrI_3. To begin, we recall that a particle with magnetic moment, $\boldsymbol{\mu}$, possesses a magnetic field, $\boldsymbol{B}(\boldsymbol{r})$, that has the form:

$$\boldsymbol{B}(\boldsymbol{r}) = \frac{\mu_o}{4\pi}\frac{3\hat{\boldsymbol{r}}(\boldsymbol{\mu}\cdot\hat{\boldsymbol{r}}) - \boldsymbol{\mu}}{r^3}$$

where $\boldsymbol{r}$ is the separation vector from the particle (positioned at the origin) to a point in free-space, r is the norm of this separation vector, $\hat{\boldsymbol{r}}$ is the corresponding unit vector and μ_o is the magnetic constant. The magnetostatic energy, E, for an interacting pair of spins is simply:

$$E = -\boldsymbol{\mu}\cdot\boldsymbol{B},$$

where $\boldsymbol{\mu}$ in this equation is the magnetic dipole moment of a particle that is being acted upon by a magnetic field of a second particle. Since all spin sites have the same magnetic moment, $\boldsymbol{\mu} = 3\mu_B\hat{\boldsymbol{z}}$, where μ_B is the Bohr magneton. This implies that in the calculation of the magnetostatic energy does not depend on the radial components of the magnetic field as the radial component is orthogonal to the z-axis. This is a valid assumption since as we will see, the resulting dipolar energy is much less than the out-of-plane magnetic anisotropy which fixes the spins to point along the z-axis. The total *interlayer* magnetostatic energy of bilayer CrI_3 is simply just the total sum of all of these interlayer pairwise interactions between all spin sites in the bilayer honeycomb lattice.

We can further simplify the expression for $\boldsymbol{B}$ by working in cylindrical coordinates. The separation vector, $\boldsymbol{r}$, between two spin sites of different layers can be analytically broken down into a component in the z-axis and one in the radial ρ-axis. The interlayer separation between layers is fixed at a distance $z_o = 7$ Å, so $\boldsymbol{r}$ has the form: $\boldsymbol{r} = z_o\hat{\boldsymbol{z}} + \rho\hat{\boldsymbol{\rho}}$ where ρ is the radial separation of the two spin sites. The expression for the z-component of the magnetic field, B_z, is:

$$B_z = \frac{3\mu_o\mu_B}{4\pi} \cdot \frac{2z_o^2 - \rho^2}{(z_o^2 + \rho^2)^{\frac{5}{2}}}$$

We can then use this B_z to find the total interlayer magnetostatic energy:

$$E_{tot} = \sum_{interlayer} -\boldsymbol{\mu} \cdot \boldsymbol{B} = \sum_{interlayer} -\frac{9\mu_o\mu_B^2}{4\pi} \cdot \frac{2z_o^2 - \rho^2}{(z_o^2 + \rho^2)^{\frac{5}{2}}}$$

One important feature of the expression for B_z is that there is a cutoff in ρ in which B_z switches sign. This means that spins that are within a radial distance $\rho = \sqrt{2}z_o$ contribute a magnetostatic energy that is opposite in sign to spins that are separated by large distances. Since B_z drops as ρ^{-3}, and the number of spin sites for some distance ρ grows as $\rho d\rho$, the largest contributions to the magnetostatic energy come from interlayer pairs with small ρ. As such, we expect the magnetostatic energy to be largely negative for small bilayer CrI_3 lattices, but eventually converge to a value close to zero as the size of the bilayer CrI_3 lattice grows.

In order to obtain ρ for each pair, we need to define the positions of each spin site. We start by defining the Bravais lattice vectors for monolayer CrI_3. The Bravais lattice of monolayer CrI_3 is hexagonal with each unit cell containing two Cr^{3+} sites as illustrated in Fig. AII.1.

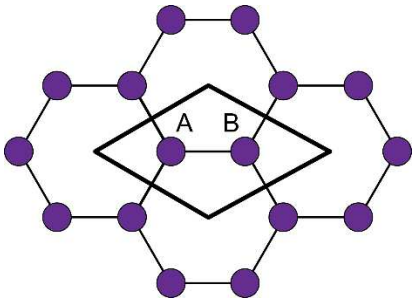

Figure AII.1. Unit cell and Cr^{3+} sublattices of monolayer CrI_3. A diamond-shaped CrI_3 cluster with a unit cell outlined by the diamond. Within the unit cell are two Cr^{3+} ions. The left Cr^{3+} ion we define as being part of the "A" sublattice while the right Cr^{3+} ion is in the "B" sublattice. The cluster has a total of ~3 × 3 unit cells.

We label the left Cr^{3+} ion as being part of the "A" sublattice while the right Cr^{3+} is part of the "B" sublattice. The choice of Bravais lattice vectors, $\boldsymbol{a}$ and $\boldsymbol{b}$, are picked to be two vectors with norm, 7 Å, and an angular separation of 60°. One can then define the positions of each unit cell, $\boldsymbol{d}$, as a coordinate, (m, n), using these two Bravais lattice vectors as a basis:

$$\boldsymbol{d} = m\boldsymbol{a} + n\boldsymbol{b}.$$

We can then determine the positions of the Cr^{3+} sites within a unit cell with respect to this basis. The coordinates of the Cr^{3+} sites in the A and B sublattices are found to be $(m - \frac{1}{6}, n - \frac{1}{6})$ and $(m + \frac{1}{6}, n + \frac{1}{6})$, respectively. We now introduce the second layer that is separated in the out-of-plane direction (z-axis) at a distance z_o away from the first layer. The stacking order of a CrI_3 bilayer is monoclinic, so we also introduce a shift vector, $\boldsymbol{s} = \frac{1}{3}\boldsymbol{a}$, to shift the top Cr^{3+} sites. Obtaining the radial separation distance, $\rho_{\Lambda\Lambda'}$, between two spin sites requires finding the norm of their radial displacement position vector, $\boldsymbol{\rho}_{\Lambda\Lambda'}$, which depends on their sublattice index, Λ and Λ' = {A, B}, where the former and latter correspond to the spins in layers 1 and 2, respectively. Therefore, the radial displacement position vector of two spins in layer 1 and 2 is:

$$\boldsymbol{\rho}_{\Lambda\Lambda'} = \boldsymbol{d}_{2,\Lambda} - \boldsymbol{d}_{1,\Lambda'} = \begin{cases} \left(m_2 - m_1 + \frac{1}{3}\right)\boldsymbol{a} + (n_2 - n_1)\boldsymbol{b}, & \Lambda = \Lambda' \\ \left(m_2 - m_1 + \frac{1}{3} \pm \frac{1}{3}\right)\boldsymbol{a} + \left(n_2 - n_1 \pm \frac{1}{3}\right)\boldsymbol{b}, & \Lambda \neq \Lambda' \end{cases}$$

The $\pm\frac{1}{3}$ term when $\Lambda \neq \Lambda'$ reflects the two cases where $\Lambda\Lambda'$ = AB or BA. The distance can be derived by taking the square root of the self-dot product of $\boldsymbol{r}_{\Lambda\Lambda'}$. Note that the dot product of $\boldsymbol{a}$ and $\boldsymbol{b}$ is $\boldsymbol{a} \cdot \boldsymbol{b} = ab\cos 60^o = \frac{1}{2}ab$.

We finally perform the calculation of the magnetostatic energy by plugging all these ρ into the E_{tot} sum. A typical bilayer flake is around (5 μm)^2 large in lateral size. This would require a diamond-shaped cluster size of ~7000 × 7000 unit cells, which is beyond the computational limits

of my computer. Instead, we perform this calculation by varying the number of unit cells in the diamond-shaped bilayer CrI_3 cluster up to a maximum of 100 × 100 unit cells and inferring the estimated order-of-magnitude total energy. As seen in Figure AII.2a, the calculated magnetostatic energy for small CrI_3 clusters with several tens of unit cells is on the order of a few μeV per Cr^{3+}, but quickly decays to zero as the cluster size increases.

To further understand the evolution of the magnetostatic behavior at large cluster sizes, we re-plot Figure AII.2a in the log-log scale (Fig. AII.2b). A notable feature when we plot the cluster size-dependent magnetostatic energy in this way is that one can notice the curve approaching a slope of ~1 for large cluster sizes. This implies that for large N where N is the number of Cr^{3+} sites, the energy decreases as a power law, E_{tot} per unit $Cr^{3+} \sim N^{-1}$. A rough estimate of the magnetostatic energy for a typical exfoliated bilayer CrI_3 flake then is around 10^{-2} μeV. This is several orders of magnitude lower than the interlayer exchange energy.

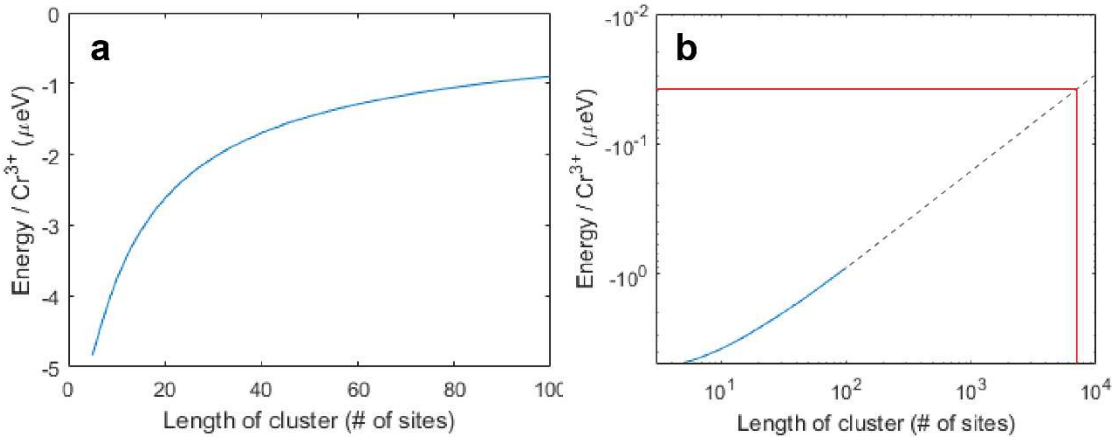

Figure AII.2. Magnetostatic energy per Cr^{3+} as a function of bilayer CrI_3 cluster size. (a-b) Calculated magnetostatic energy for diamond-shaped monoclinically stacked bilayer CrI_3 of varying sizes plotted in (a) the linear scale and (b) the log-log scale. In (b), the curve appears to approach a slope of ~1 indicated by the gray dashed line. Extrapolating to ~7,000 sites (indicated by the red lines), the size of a typical exfoliated bilayer flake, the energy is ~4 × 10^{-2} μeV/Cr^{3+}.

APPENDIX III

Supplementary Figures for Section IV

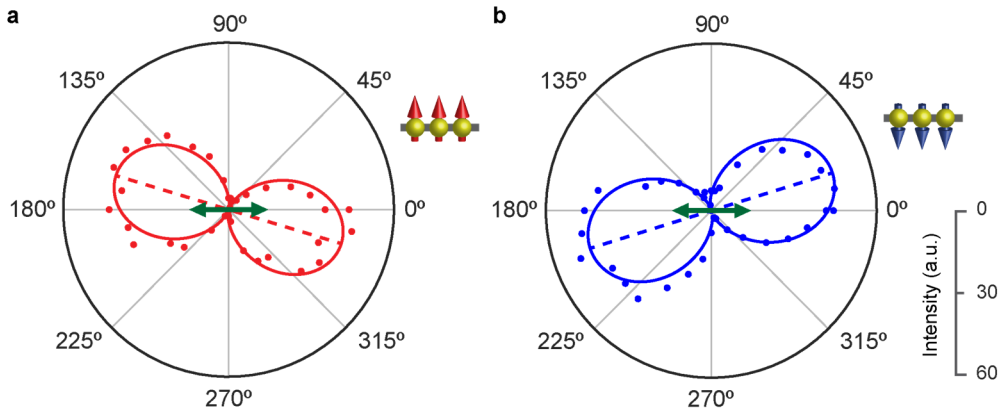

Fig. AIII.1. Raman scattering rotation of 76.9 cm^{-1} phonon in monolayer CrI_3. (a-b) Polarization rotation of the 76.9 cm^{-1} peak of monolayer CrI_3 in the (a) spin-up state and (b) spin-down state taken at T = 15 K without an applied magnetic field. Dashed lines show the polarization axis of the 76.9 cm^{-1} phonon. Green double-sided arrow shows the excitation polarization of the laser. Equal, but opposite rotation of about 15° is observed between the two ferromagnetic states, qualitatively consistent with the behavior seen from the 127.4 cm^{-1} phonon. Reproduced from ref. [57].

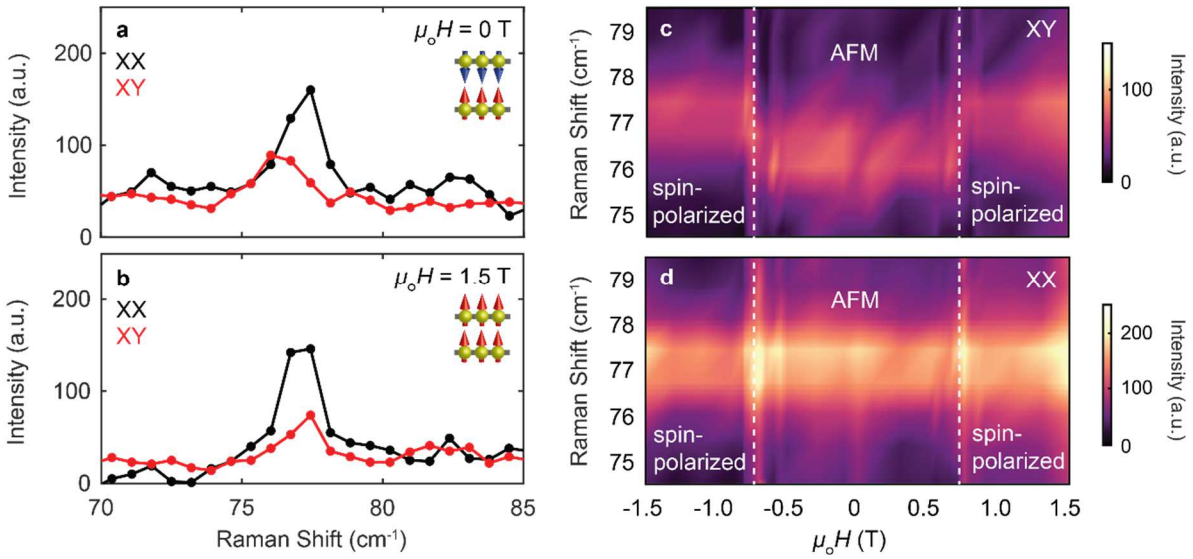

Figure AIII.2. Magnetic field-dependence of Dayvdov-split 76.9 cm^{-1} A_{1g} mode in antiferromagnetic bilayer CrI_3. (a-b) Co- (black) and cross-linearly (XY) scattered light near 76.9 cm^{-1} peak taken at (a) 0 T in the layered antiferromagnetic states and (b) 1.5 T in the spin-up ferromagnetic-like state. A small splitting can be seen between the peaks in the XX and XY channels in (a). (c-d) Magnetic field-dependent Raman spectra color maps of the two Davydov-split modes near 76.9 cm^{-1} in the (c) XY and (d) XX channels. The spin-flip transitions between the ferromagnetic-like states and the antiferromagnetic states are demarcated by white dotted lines. Although the splitting is smaller for the two modes near 76.9 cm^{-1}, the abrupt suppression of one mode and the activation of the second follow at the spin-flip transition match the magnetic field behavior of the modes at 126.7 cm^{-1} and 128.8 cm^{-1}, suggesting qualitatively similar selection rules for the lower energy pair of phonons. Reproduced from ref. [57].

APPENDIX IV

Supplementary Figures for Section V

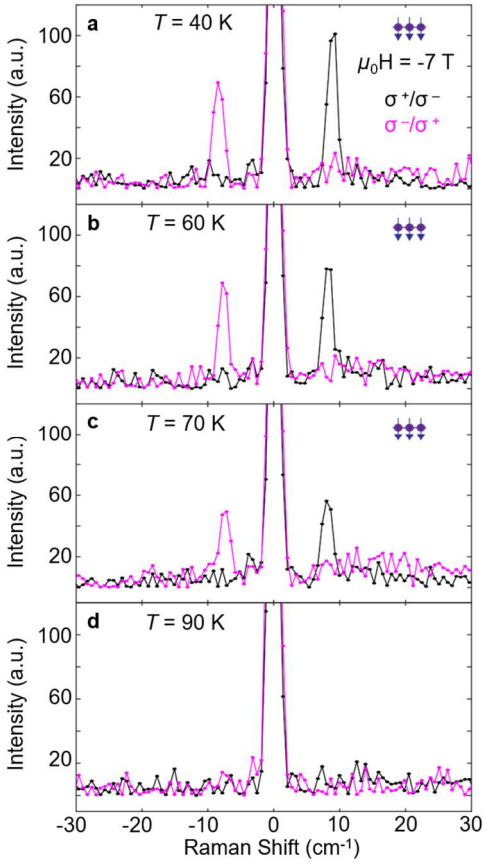

Fig. AIV.1. Low-frequency Raman spectra of monolayer CrI_3 at select temperatures. (a-d) Cross-circularly polarized Raman spectra taken at various temperatures in an applied field of -7 T. Due to the applied field, the magnon is shifted away from the Rayleigh line and is present until ~80 K, well above the Curie temperature of T_C ~ 45 K. Notably, the linewidth does not appear to significantly broaden throughout this temperature range. Reproduced from ref. [137].

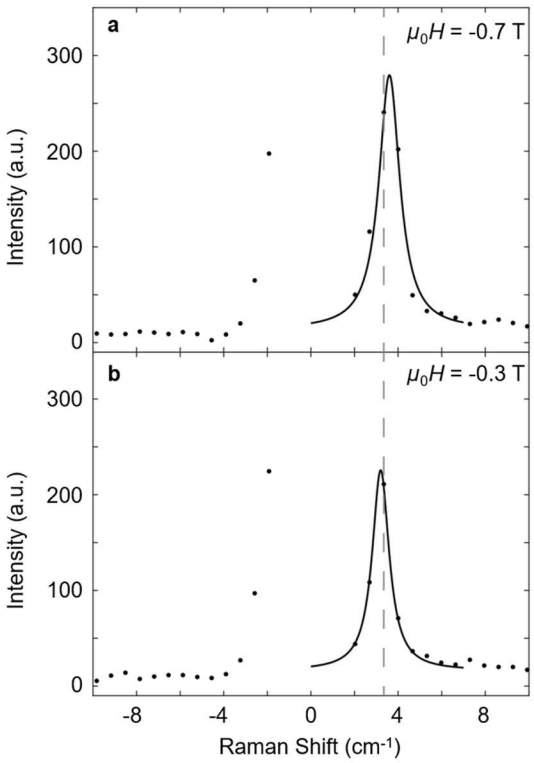

Fig. AIV.2. Lorentzian fits of the acoustic magnon in AFM bilayer CrI_3. (a-b) Lorentzian fit of the acoustic magnon in bilayer CrI_3 in an applied field of (a) -0.7 T and (b) -0.3 T. The center of the Lorentzian fits are at 3.6 cm^{-1} and 3.2 cm^{-1} respectively. The grey dashed line indicates the CCD pixel of the spectrometer with the highest counts of the magnon feature. Reproduced from ref. [137].

VITA

Bevin Huang was born in Portland, Oregon and was raised for most of his life in Clackamas, a suburb of Portland. From a young age, he was always curious about how things work – why the sky was blue, how pianos produce sound – though some questions landed him in trouble as a kid. He also loved working with numbers and always sought for opportunities to use them in math, in science, and in music. With the inspiration of his science teachers in high school and encouragement from his parents, he pursued a degree in physics at Virginia Polytechnic Institute and State University in Blacksburg, Virginia. Guidance by Profs. Mark Pitt, and Chenggang Tao, set him straight on a course for experimental condensed matter physics in Prof. Xiaodong Xu's lab at the University of Washington in Seattle, Washington. This was a choice that he will never regret and was certainly one of the most meaningful and impactful decisions of his life.